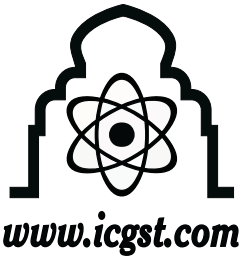

The International Congress for global Science and Technology (ICGST)

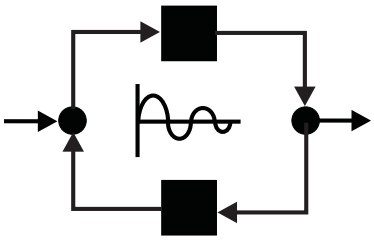

ICGST International Journal on Automatic Control & System Engineering (ACSE)

Volume (12), Issue (II)
October 2012

wwww.icgst.com
www.icgst-amc.com
www.icgst-ees.com

© ICGST LLC, Delaware, USA, 2012

ACSE Journal
ISSN: Print 1687-4811
ISSN Online 1687-482X
ISSN CD-ROM 1687-4838
© ICGST LLC, Delaware, USA 2012

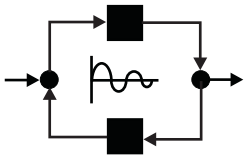

Table of Contents

Papers	Pages
P1111209135, Tarun Varshney and Satya Sheel, "PID Control of MIMO Turbo – Generator Plant Based on Genetic Algorithm"	1--6
P1111217176, Mohamed F. Hassan and Hala A. Mourad, "Closed Loop Controller for Stochastic Systems with Uncertain Parameters"	7--14
P1111210136, O. Chandra Sekhar, Dr.K.Chandra sekhar Member, IEEE, "A Novel Nine-Level MPC Inverter for Direct Torque Control Induction Motor Drive "	15--22
P1111219191, Akram Abu-aisheh and Sameer Khader, "Hybrid MPPT-Controlled LED Illumination Systems"	23--30
P1111212142, G. Sambasiva Rao and K. Chandra Sekhar, "A sophisticated Space Vector Pulse Width Modulation Signal Generation for Nine-Level Inverter system for Dual-Fed Induction Motor Drive"	31--34
P1111223205, H. Bellahsene and I. F. E. Fatani, "Amélioration du temps de convergence de l’algorithme de calcul du filtre optimal par HOS en DMT"	47--51
P1111217174, C. Harikrihsna and T. Bramhananda Reddy and J. Amarnath and S. Kamakshaiah, "Simple and Novel Generalized Scalar PWM Algorithm for Multilevel Inverter Fed Direct Torque Controlled Induction Motor"	39--46

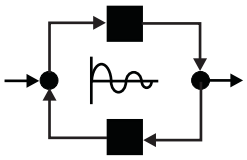

ICGST International Journal on Automatic Control & System Engineering - (ACSE)

A Publication of the International Congress for global Science and Technology - (ICGST)

ICGST Editor in Chief: Dr. rer. nat. Ashraf Aboshosha

www.icgst.com, www.icgst-amc.com,

www.icgst-ees.com

editor@icgst.com

www.icgst.com

Improved PID MIMO Control of Turbo Generator relying on Genetic Algorithm

Tarun Varshney, Satya Sheel
Electrical Engineering Department, Motilal National Institute of Technology, Allahabad, India,
t_varshney@yahoo.com, satyasheel@mnnit.ac.in

Abstract
PID controllers are widely used in industries due to simple functioning and robustness, yet the determination of controller gains is a big challenge more so when the plant to be control is multi input multi output (MIMO) and nonlinear in nature. The aim of this paper is to string together the qualities of conventional PID controller and a recent technique Genetic Algorithm (GA). In this work controller parameters are adjusted by means of fitness function that can evaluate the optimum PID parameters based on system error. Simulation study has been carried out for a turbo- generator and the results have been compared with decoupled control and diagonal recurrent neural network (DRNN) based PID tuning methods. A simulation result shows that the proposed control scheme results in smaller controller effort.

Keywords: *Genetic algorithm, PID Tuning, MIMO system*

1. Introduction
PID controllers are widely used in industries due to their simple functioning and robustness but determination of controller gains has always been a big challenge. Most industrial processes are multivariable and their nonlinear and interactive behavior imposes difficulties in determination of the parameters of controller. In such a situation progressive technique like GA has been shown to be capable of high performance without experiencing the difficulties [1], [10]. GA offers an adaptive heuristic search algorithm based on the evolutionary ideas of selection and genetics [2]. It is inspired by Darwin's theory about evolution- "Survival of fittest". GA represents an intelligent exploitation of random search used to solve optimization problems. Takhiro and Sigeru [3] applied GA to tune the PID gains for a single input single output (SISO) water bath system and proved that real number encoding is simple to operate and better than bit string encoding method. Mitsukura, Yamamoto and Kaneda [4, 5] proposed a new tuning method of PID parameters based on the relationship between the PID control law and the generalized minimum variance control show the effectiveness of proposed method for the nonlinear SISO Hammerstein model. Maja and Kabra [8] presented a tuning method for multivariable controller that was based on decoupling control and GA. As this method tends to achieve the shortest direct paths through the system (without inverting the model), it usually results in low energy consumption which can further be directly controlled with pole placement. Jih-Gau Juang et al. [12] used GA to tune the PID parameters to control a laboratory helicopter called twin rotor system. All parameters of the controller are obtained by a real-value-type genetic algorithm (RGA) with an integral of time multiplied by the square error criterion. Jin-Sung Kim et. al [13] proposed tuning method which was based on improved GA. For better performance they defined new objective function in the sense of root mean square error. In addition they made improvement by replacing the uniform distribution random number generation in conventional GA to newly designed hybrid random generator composed of Cauchy distribution and linear congruential generator which provides independent and different random numbers at each individual steps in Genetic operations. In many research works GA has been widely applied to tune the PID parameters such as a nonlinear model of thermal process [9], gasifier problem [11], missile control system, DC motor position control, LTI system, liquid level system [14-17]. Monica Patrascu et al. [18] applied GA to tune the parameters of PID controller for nonlinear model MIMO system. They have focused on the initialization procedure of the algorithm that can influence the outcome of the optimization procedure and showed that roulette wheel selection is better choice for selection. Daniel Carmona Morales et.al [20] developed a Graphical user interface system for optimum tuning of multivariable PID controller. From the educational point of view, this tool provides students with the necessary means to consolidate their knowledge on these control structures. In this work GA is chosen to tune the parameters of PID controller for a MIMO Turbo- Generator plant which is highly nonlinear and has strong coupling among variables. The simulation results have obtained by the proposed approach been compared with those obtained by fixed decoupled PID configuration and also with DRNN based tuning of controller parameters [19].

The rest of paper is organized as follows. In the next section basic steps of GA are described. In Section 3 Genetic operator such as Selection, Crossover and mutation are illustrated. Section 4 describes the evaluation procedure based on fitness function and fitness value. In section 5 the basic ideas of the tuning method are presented. Section 6 describes the Turbo-Generator plant considered and simulation studies are presented in Section 7. Concluding remarks are in last Section.

2. Genetic Algorithm

GA is a stochastic search method that emulates the process of natural evolution. It starts with the minimal knowledge of the correct solution and depends entirely on responses from its environment and genetic operators e.g. selection or reproduction, crossover and mutation to get the optimal solution [1]. By starting at several independent points and searching in parallel, the GA avoids local minima and converges to sub optimal solutions. The GA is typically initialized with a random population consisting of between 20-100 individuals. This population is usually represented by a real valued number or a binary string called a chromosome. Individual performance is measured by the fitness function. The fitness function assigns each individual a corresponding number called its fitness value. The fitness value of each chromosome is assessed and a survival of the fittest strategy is applied. There are three main genetic operators of the GA, these are known as Selection or reproduction, crossover and mutation.

The steps involved in implementing the GA are as follows:

1. Generate an initial, random population of individuals for a fixed size.
2. Applying it to the process
3. Evaluate the process using fitness function chosen i.e. IAE plus weighted control efforts (squared)
4. Select the fittest members of the population.
5. Reproduce using a probabilistic method.
6. Implement crossover operation on the reproduced chromosomes
7. Execute mutation operation with low probability.
8. Repeat step 2 until a predefined convergence criterion is met. The convergence criterion of a genetic algorithm is a user-specified condition e.g. the maximum number of generations or when the string fitness value exceeds a certain threshold.

An illustrative flowchart of the GA implementation is shown in Figure 1

3. Genetic Operator

To maintain the genetic diversity GA uses the operators. Genetic diversity is a necessarily procedure for process of evolution. Commonly three main Genetic operators of selection or reproduction, crossover and mutation are used in implementation of GA.

A. Selection or Reproduction

Selection is usually the first operator applied on population. The Selection operator is also known as reproduction operator. Selection means extract a subset of genes from an existing population. Every gene has a meaning so one may extract a kind of quality measurement called as fitness value and by following this quality selection can be done. Fitness function quantifies the optimality of a solution so that a particular solution may be ranked against all the other solutions. The function shows the degree of the closeness of the given solution to the desired solution. Roulette wheel selection, Rank selection, Boltzmann selection, Steady state selection and tournament selection are examples of selection operators [18].

B. Crossover

After the selection, crossover operator takes place and it combines two chromosomes (parents) to produce anew chromosome (offspring).The centre idea of crossover is that the new generated chromosome may be better than

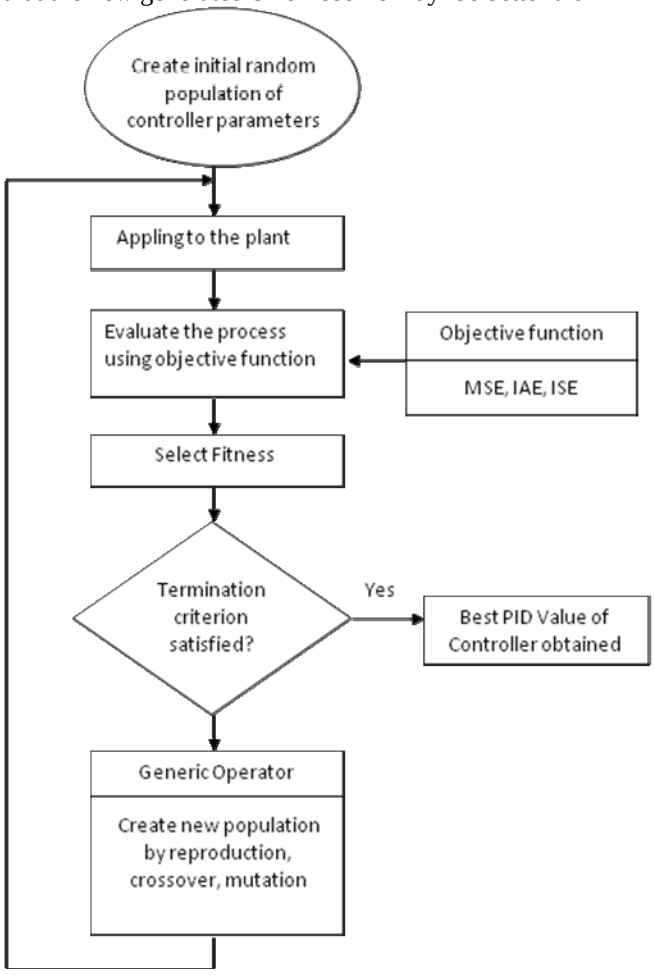

Figure 1 Flowchart of Genetic Algorithm

both the parents if it takes the better characteristics from each of them. It depends on user specified crossover probability. It indicates how often crossover is performed. A probability of 0% means that the 'offspring' will be exact replicas of their 'parents' and a probability of 100% means that each generation will be composed of entirely new offspring. One point crossover, two points, uniform, arithmetic and heuristic are few types of crossover.

C. Mutation

Mutation is the last operation in GA. It is used to maintain genetic diversity from one generation of a

population of chromosome to the next generation. It depends upon the user defined mutation probability. Mutation probability values of around 0.1% or 0.01% are common, these values represent the probability that a certain string will be selected for mutation i.e. for a probability of 0.1%; one string in one thousand will be selected for mutation. Mutation alters one or more gene values in a chromosome from its initial state. This can result a fairly new gene value being added to the population and with new gene value the GA is able to get better solution in contrast to previous solution. Mutation helps to prevent the population from stagnating at any local minima. The mutation operators are of many types such as flit bit, Boundary, Non uniform, Uniform and Gaussian.

4. Process Evaluation Based on Fitness Function

A. Fitness function / Performance index

The most crucial action to choose the fitness function to evaluate the fitness of each chromosome. Performance indices such as mean square error (MSE), integral time multiplied by absolute error (ITAE), integral absolute error (IAE) and integral square error are commonly used as the fitness function in applying GA [7].

B. Fitness Value

The PID controller is designed to minimize the fitness function which is function of system error. The smaller value of fitness function indicates the higher fitness value of the corresponding chromosome and vice versa, and it is represented by

$$fitness\ value = \frac{1}{fitness\ function} \tag{1}$$

5. Problem Formulation

Figure 2 depicts the schematic diagram of the proposed genetic tuning of PID parameters. The scheme composes of usual feedback control system which has the full model of coupled nonlinear multivariable plant and the PID controller. The parameters of controller have been recursively tuned online by GA. To begin with, we assume that system to be controlled has multiple inputs $u(k) \in \Re^{m\,x\,1}$ and multiple outputs $y(k) \in \Re^{p\,x\,1}$ and the control objective is to follow a prescribe set points $r(k) \in \Re^{p\,x\,1}$. Let the tracking error be defined by

$$e(k) = r(k) - y(k) \tag{2}$$

and the controlled input of the system is

$$u(k) = K(k)X(k) \tag{3}$$

where $K(k) \in \Re^{m\,x\,3}$ is the set of controller's parameters $[k_p(k)\ \ k_i(k)\ \ k_d(k)]$ and of and $X(k) \in \Re^{3\,x\,p}$ is the set of errors which is represented by $[x_1(k)\ \ x_2(k)\ \ x_3(k)]^T$.

$$u(k) = k_p(k)x_1 + k_i(k)x_2 + k_d(k)x_3 \tag{4}$$

where $x_1(k) = e(k)$, $x_2 = \sum_{k=1}^{n} e(k)T$,

$x_3 = \frac{e(k) - e(k-1)}{T}$, and k_p, k_i, k_d are proportional, integral, and derivative gains respectively and T is sampling time. The convergence criterion of a GA is a user-specified condition and termination of tuning of PID parameters can be done by reaching the maximum number of generations or when the fitness value exceeds a certain threshold**.** To get the satisfactory dynamic characteristics IAE has been considered as the fitness function in the present work. To limit the controlled input from being too large, it also accumulates the quadratic term of controlled input to the fitness function. The expression for modified fitness function can be represented as follows

$$J = \sum_{k=1}^{n} \left(w_1 |e(k)| + w_2 u^2(k) \right) \tag{5}$$

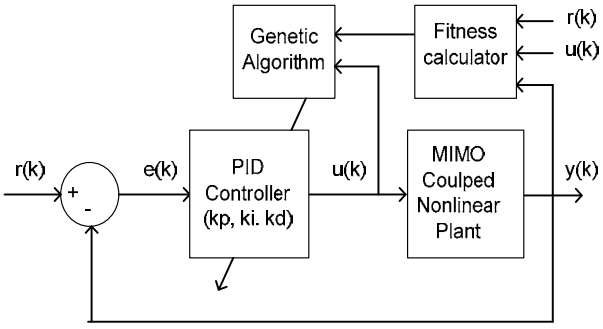

Figure 2 Schematic diagram of PID tuning based on GA

6. The Turbo - Generator Plant

The schematic diagram of laboratory scale turbo-generator plant is shown in Figure 3, It was developed as an emergency power supply for biological experiments [6]. A compressed centre air supply runs a turbine which drives a Y - connected three phase synchronous generator. The field of the generator is separately excited by an external source. A balanced three phase resistance serves as a load which can be switched between 1.5 Ω and 2.5 Ω. A tacho generator is used for speed measurements. The percentage of valve opening V (%) and field current i_E (mA) are input signals $u_1(t)$ and $u_2(t)$ respectively. The turbine speed n (min^{-1}) and the rectified mean value of the generated voltage U_A (V) are considered as the output signals $y_1(t)$ and $y_2(t)$ respectively. The numbers of machines poles are constant so the frequency f (Hz) of the generated unrectified voltage is proportional to speed n.

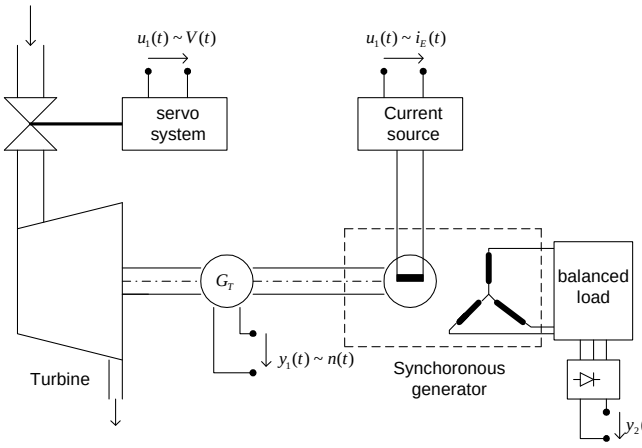

Figure 3. Schematic diagram of laboratory scale turbo-generator plant

7. Simulation Results

Turbo- Generator plant which is nonlinear coupled MIMO system is used to illustrate the effectiveness of the proposed scheme. The Input-Output relation is as follows:

$$y_1(k) = 0.4y_1(k\text{-}1) + \frac{u_1(k\text{-}1)}{1+u_1^2(k\text{-}1)} + 0.2u_1^3(k-1) + 0.5u_2(k-1) \qquad (6)$$

$$y_2(k) = 0.2y_2(k\text{-}1) + \frac{u_2(k\text{-}1)}{1+u_2^2(k\text{-}1)} + 0.4u_2^3(k-1) + 0.2u_1(k-1) \qquad (7)$$

The GA is used to tune for the optimal PID parameters that minimize the fitness function (Eq. 5). Therefore the parameter tuning task of the PID controller using GA can be considered by selecting the three parameters k_p, k_i and k_d such that the response of plant will be as closest to desire response. The GA parameters chosen for simulation are shown in Table 1.

Table 1 Parameters of GA

GA property	Value/ Method
Population Size	30
Maximum Number of generations	100
Fitness Function	Quadratic form as in Eq (5)
Selection Method	Roulette wheel selection
Crossover Probability	0.90
Crossover Method	Arithmetic Crossover
Mutation Probability	0.01

Initially many individual solutions are randomly generated to form an initial population, allowing the entire range of feasible solutions that results in stable response ($0<k_{p1}<0.7$, $0<k_{i1}<0.9$, $0<k_{d1}<0.3$, $0<k_{p2}<1$, $0<k_{i2}<1$, $0<k_{d2}<1$). Initial solution can be generated by following expression

$$x = a + (b-a)*rand \qquad (8)$$

where a, b are upper and lower limits of the parameter value k_p, k_i and k_d and rand is a random number between 0 to 1. System response to sum of delayed step function is shown in Figure 4 and a fair comparison among three different techniques is also shown. It can be seen that with the help of proposed scheme system response becomes quite faster, rise time becomes shorter and smaller controlled input is required to meet the desire response (Figure 5). The optimization process of the fitness function is shown in Figure 6 which shows the optimize value of fitness function at each iteration. Finally optimize PID parameters are $K = \begin{bmatrix} 0.1985 & 0.1458 & 0.0119 \\ 0.1166 & 0.0454 & 0.0207 \end{bmatrix}$.

All the computation has been done on Intel Core 2, 6320@1.86GHz machine and a fair comparison of computational burden is shown in Table 2 which indicates that due to complexity, proposed algorithm consumes more time to tune the PID parameters.

Table2 Computational burden

Technique	Computational time(sec)
Fixed PID	0.0290
DRNN based PID Tuning	0.0500
GA based PID Tuning	3.6020

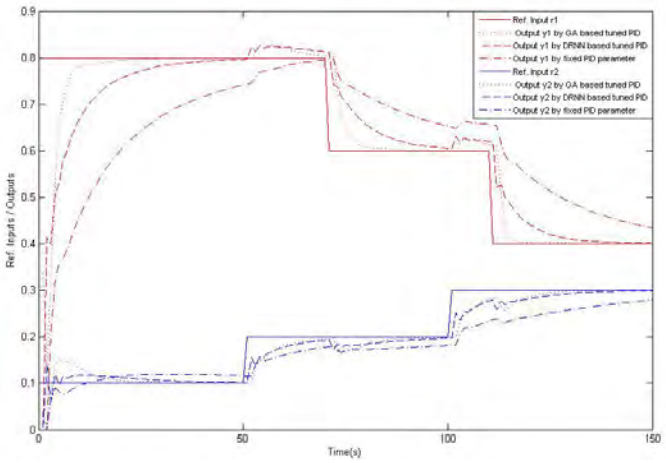

Figure 4 System response to sum of delayed step function

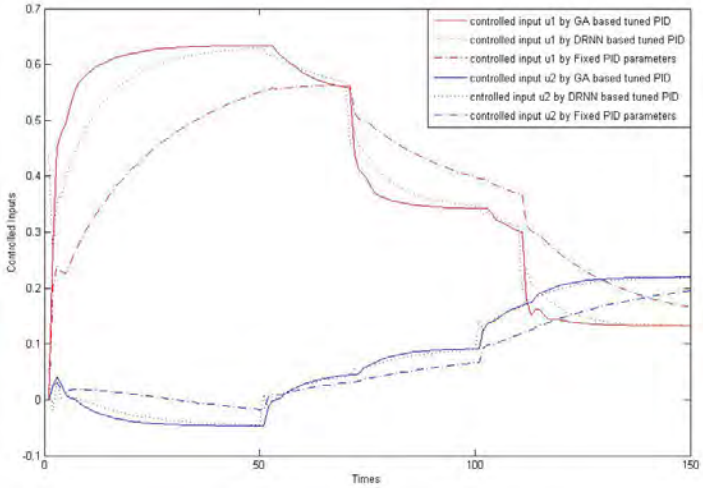

Figure 5 Controlled inputs

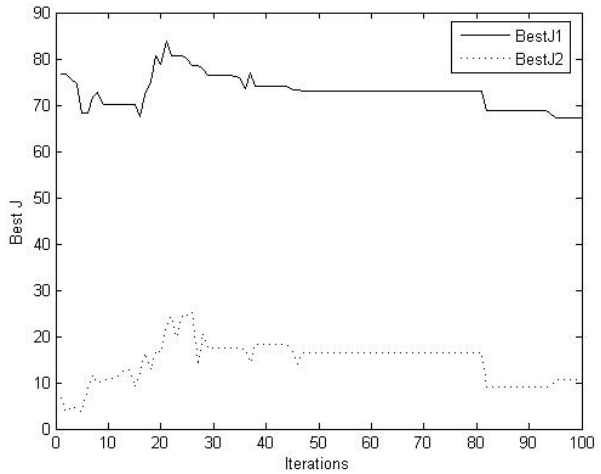

Figure 6 Optimization Process of fitness function

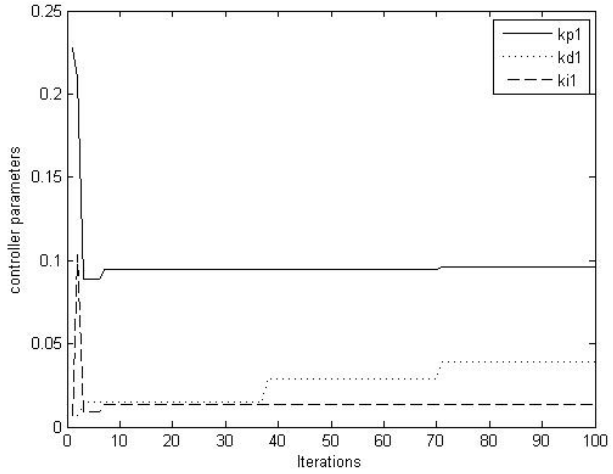

Figure 7 Controller's Parameter for first input

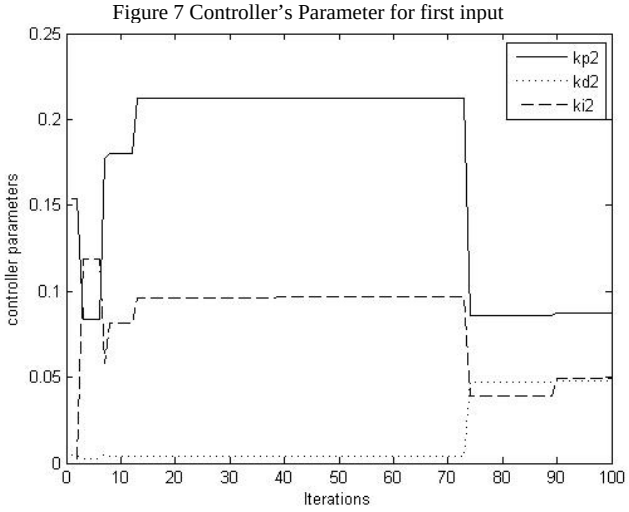

Figure 8 Controller's Parameter for Second input

8. Conclusions

This paper demonstrates that how GA can be used to optimize the parameters of PID controller for turbo-generator plant. The features of the proposed scheme are summarized as follows:

- Optimized parameter can be obtained by optimizing the PID parameters controller with GA.
- It is important to select permissible upper and lower limits of parameters otherwise an optimal solution is not possible in realistic time frame i.e. online / real time.
- The parameter optimization is global and has there is no connection with initial population.
- With lower rise time and controlled input the proposed scheme is capable to better rack the delayed step function compare to other techniques.
- Controlling input effort is reduced and this offers a major advantage.

9. Acknowledgements

Tarun Varshney is with the Department of Electronic Instrumentation Engineering of Moradabad Institute of Technology, Moradabad, India and currently pursuing research at Motilal Nehru National Institute of Technology, Allahabad, India. He wishes to acknowledge the all support and facility of Moradabad Institute of Technology for his work.

10. References:

[1] D.E. Goldberg, 'Genetic algorithm in Search, Optimization and Machine learning', Addison-Welsey Pulbilcation Co. Inc, 1989.

[2] Dr A.H Jones and P.B. de Moura Oliveira, 'Genetic Auto-Tuning of PID controller', International Conference on Genetic Algorithms in Engineering Systems: Innovations and Applications, Sheffield, UK, pp 141-145, 1995

[3] Takhiro Ota, Sigeru Omatu, 'Tuning of the PID Control Gains by GA', IEEE Conference on Emerging Technologies and Factory Automation, Kauai, Hawaii, pp 272-274, 1996

[4] Y. Mitsukura, T. Yamamoto and M. Kaneda, 'A Genetic Tuning Algorithm of PID parameters', IEEE International Conference On Systems, Man, And Cybernetics , Orlando, Florida, USA, vol. 1, pp 923-928,1997.

[5] Yasue Mitsukura, Toru Yamamoto and Masahiro Kaneda, 'A design of self tuning PID controllers using genetic algorithm', Proceeding of American control conference, San Diego, California, pp 1361-1365, 1999.

[6] Thomas F. Junge, Heinz Unbehauen, 'Recursive identification of a Turbo- Generator plant using structurally adaptive neural network', Proceedings of IEEE International Conference on Industrial Technology, Goa, India, pp 572-577, 2000.

[7] T O. Mahony, C J Downing and K Fatla, 'Genetic Algorithm for PID Parameter Optimization: Minimizing Error Criteria', Process Control and Instrumentation, University of Stracthclyde, pp 148-153, 2000.

[8] Maja Atanasijevi C-Kunc, Rihard Karba, 'Multivariable controller tuning by genetic algorithms', International Conference on Information

Technology Interfaces, Pula, Croatia, pp 337-342, 2000.

[9] J.M. Herrero, X. Blasco, M. Martínez, J.V. Salcedo, 'Optimal PID tuning with genetic algorithms for non linear process models', 15th Triennial World Congress, Barcelona, Spain,2002

[10] Ian Griffin, 'On line PID controller tuning using genetic algorithm', Dublin City University, 2003.

[11] Farag and H. Werner, "Structure selection and tuning of multivariable PID controller for an industrial benchmark problem", IEE proceeding of control theory and applications, vol.153, no 3, pp 262 – 267, 2006.

[12] Jih-Gau Juang, Ming-Te Huang, and Wen-Kai Liu, " PID control using presearch genetic algorithms for MIMO systems", IEEE Transactions on systems, man, and cybernetics —Part C: applications and reviews, vol. 38, No. 5, pp 716-727, 2008.

[13] Jin-Sung Kim, Jin- Hwan Kim, Ji-Mo Park, Sung-Man park and Won-Yong Choe, 'Auto Tuning PID controller based on improved Genetic algorithm for reverse osmosis plant', World Academy of Science, Engineering and Technology, pp 384-389, 2008.

[14] Zhu Supeng, Fu Wenxing , Yang Jun and Luo Jianjun, 'Applying Genetic algorithm to optimization parameters of missile control system', International conference on Hybrid Intelligent system, Shenyang, China, pp 416-419, 2009.

[15] Neenu Thomas, Dr. P. Poongodi, 'Position Control of DC Motor using genetic algorithm based PID controller', Proceeding of world congress on Engineering,Vol. II, London, UK, 2009.

[16] P. Poongodi, S. Victor, 'Genetic Algorithm based PID controller design for LTI system via reduced order model' International conference on Instrumentation, Control and Automation, Bandung, Indonesia, pp 115-118. 2009.

[17] Mohammed Obaid Ali, S. P Koh, K. H. Chong, S.K. Tiong and Zeyad Assi Obaid, 'Genetic Algorithm Tuning based PID controller for liquid level tank system', International Conference on Man-Machine System, Batu Ferringhi, Penang, Malaysia, pp 4A5-1- 4A5-5, 2009.

[18] Monica Patrascu, Adrian Bogdan Hanchevici, Ioan Dumitrache , 'Tuning of PID Controllers for Non-Linear MIMO Systems Using Genetic Algorithms', 18th IFAC World Congress Milano (Italy), pp 12644-12649, 2011.

[19] Tarun Varshney, Satya Sheel, "A New Online Tuning Approach for PID Control of Multivariable Systems using Diagonal Recurrent Neural Network", IEEE International Conference on Control System, Computing and Engineering, Penang, Malaysia,2011.

[20] Daniel Carmona morles, Jorge E. Jimenez-Hornero, Francisco Vazquez and Fernando Morilla, " Education toolfor optimal controller tuning using evolutionary strageties", IEEE transaction on Education, vol. 55, No. 1. 2012.

Biographies

Tarun Varshney was born in India in 1978. He received the B.E. degree in Electronics & Instrumentation Engineering from Rajasthan University, Jaipur, India, in 2001, M.Tech. in Control & Instrumentation from Motilal Nehru National Institute of Technology, Allahabad, India, in 2007. Currently he is pursuing Ph.D. at NIT, Allahabad. His research interests include intelligent control systems, multi-variable systems modeling and neural networks.

Satya Sheel received his Bachelors ('68) in Electrical, Masters ('76) in Control systems and Ph.D. in Systems and Control Engineering ('82). Currently he is a Professor at the National Institute of Technology at Allahabad, India. He is a senior member of IEEE, fellow of Institution of Engineers (I) and has been India representative of AMSE (France). He is a reviewer for journals, conferences and books in control, instrumentation. His current interests are intelligent control of multivariable systems, PID controller tuning, embedded systems, process control, machinery health diagnostics and control engineering education.

www.icgst.com

Closed Loop Controller for Stochastic Systems with Uncertain Parameters

Mohamed F. Hassan and Hala A. Mourad
Electrical Engineering Department, College of Engineering,
Kuwait University, 13060 Kuwait
phone: +965-2498-7634; fax: +965-2481-7451
m.f.hassan47@gmail.com & m.fahim@ku.edu.kw

Abstract
In this paper an observer-based stochastic controller is developed for linear stochastic discrete-time dynamical systems with uncertain parameters. A state estimator, based on Kalman filter, is firstly developed which incorporates in its structure the statistical information of the uncertain parameters. Although the developed estimator uses the nominal values of the system parameters; it showed to be stable, robust and gives satisfactory results. Such an estimator is then used to design an observer-based controller for discrete-time linear stochastic dynamical systems. The effectiveness of the theoretical derivation of the developed estimator and the observer-based controller are illustrated via a numerical example and a practical case study.

Keywords: *Discrete-time systems, linear systems, nonlinear systems, state estimation, stochastic systems, control design.*

1. Introduction
Since most, if not all, real control systems are stochastic by their nature, it has been essential to develop and enhance stochastic control theory which mainly deals with this type of problems. With the progress of computational tools, and the development of state space approach, it became a systematic procedure to represent system models by state equations rather than frequency domain models. In practice, the states of the system are not accessible to direct measurements. Therefore, it was mandatory to develop a theory for state reconstruct of the system in order to generate the desired control strategies. For deterministic linear finite–dimensional time invariant systems, an observer was first introduced by Luenberger [1] leading to the asymptotic estimation of the state. In case of linear dynamical system with random disturbances, where the stochastic phenomena appears, the state estimation problem is solved using Kalman filter (KF) [2]. In standard Kalman filter, all the system characteristics (i.e. system model, initial conditions, and noise characteristics) have to be specified a priori. However, if there is an uncertainty in any of these characteristics, the filter may not be robust enough. For state estimation of linear discrete systems with uncertain parameters, interested readers can refer to [3] and references therein. On the other hand, for nonlinear dynamical systems, the stability, and hence the robustness of the estimator become worse. Several algorithms have been proposed to estimate the states of nonlinear systems [4, 5, 6, 7, and 8] and references therein. In general, the extended Kalman filter (EKF) is the most extensively used algorithm for state estimation of nonlinear systems. However, it is not the optimal estimator, and it may diverge if the system acquires strong nonlinearities, or the initial estimate of the state is wrong, or the process is modeled incorrectly, owing to linearization [9, 10, 11].

In this paper, a new approach is proposed to estimate the states of linear stochastic discrete-time dynamical system with uncertain parameters. The system model and the measurements are assumed to be corrupted by uncorrelated zero mean white Gaussian noise sequences. The parameters of the system are assumed to be uncertain, which obviously leads to an estimation problem of nonlinear (bilinear) stochastic discrete-time dynamical system. The new filter handles this problem and its performance is compared with that of the KF, when the parameters are assumed to be certain, and with the EKF, when the parameters are decided to be estimated. The proposed estimation technique is used to design an observer-based controller for linear stochastic discrete-time system with uncertain parameters. For linear stochastic systems with certain parameters, the separation principle holds. Therefore, controller design and state estimator can be performed separately. This leads to an optimal closed loop stochastic controller [12]. However, in case of stochastic systems with uncertain parameters, the separation principle does not hold, since additional terms will appear in the state space representation of the augmented system due to the uncertain components of the system parameters. Although this is the case, we can still design a closed loop suboptimal observer-based controller provided that it leads to an asymptotically stable system. To show the effectiveness of the developed estimation approach, illustrative examples are solved using the proposed estimator, the KF and the EKF

with parameter estimation. MATLAB is used as a programming tool and Monte Carlo simulation is applied to compare the behavior of the different filters. An observer-based controller, using the developed estimator, is designed to regulate a DC motor. The obtained results show the applicability and efficiency of the proposed procedure in handling this problem.

The rest of the paper is organized as follows. In section 2, the control problem for stochastic linear discrete-time dynamical systems with uncertain parameters is formulated. Section 3 is devoted to the presentation of the mathematical structure of the developed estimator. The dynamics of the observer-based controller is presented in section 4. The algorithm used to implement the closed loop stochastic controller is given in section 5. In section 6, illustrative examples are solved to show the effectiveness of the proposed design approach. The paper is concluded in section 7.

2. Problem Formulation

Let us define the following stochastic control problem:

$$\min \boldsymbol{J} = \boldsymbol{E}\left\{\frac{1}{2}\sum_{k=k_o}^{k_f-1}\left[\left\|\boldsymbol{x_k}-\boldsymbol{x^d}\right\|_{\boldsymbol{M}}^2+\left\|\boldsymbol{u_k}\right\|_{\boldsymbol{N}}^2\right]\right\} \quad \text{(1-a)}$$

Subject to:

$$\boldsymbol{x_{k+1}} = \boldsymbol{A_k x_k} + \boldsymbol{B_k u_k} + \boldsymbol{d} + \boldsymbol{w_k} \quad \text{(1-b)}$$

$$\boldsymbol{y_{k+1}} = \boldsymbol{C_{k+1} x_{k+1}} + \boldsymbol{v_{k+1}} \quad \text{(1-c)}$$

where: $\boldsymbol{x_k} \in \boldsymbol{R^n}$ is the state vector, $\boldsymbol{y_k} \in \boldsymbol{R^m}$ is the output vector, $\boldsymbol{u_k} \in \boldsymbol{R^r}$ is the control vector, $\boldsymbol{d} \in \boldsymbol{R^n}$ is a constant vector, $\boldsymbol{x^d} \in \boldsymbol{R^n}$ is the desired state vector, $\boldsymbol{A_k} = \left[\boldsymbol{a_{ij_k}}\right] \in \boldsymbol{R^{nxn}}$ is the system matrix with uncertain parameters, $\boldsymbol{a_{ij_k}}; \boldsymbol{i,j} \in \{1,2,....,\boldsymbol{n}\}$ assumed to be uncorrelated white Gaussian random variables with the following statistics $\boldsymbol{a_{ij_k}} \sim \boldsymbol{N}(\bar{\boldsymbol{a}}_{\boldsymbol{ij}}, \boldsymbol{\sigma}^2_{\boldsymbol{a_{ij}}})$, $\boldsymbol{B_k} \in \boldsymbol{R^{nxr}}$ is the control transition matrix, $\boldsymbol{w_k} \in \boldsymbol{R^n}$ is a zero mean white Gaussian input noise vector with covariance matrix $\boldsymbol{Q_k} = \boldsymbol{E}\{\boldsymbol{w_k w_k^T}\} \in \boldsymbol{R^{nxn}}$, $\boldsymbol{C_{k+1}} = \left[\boldsymbol{c_{ij_{k+1}}}\right] \in \boldsymbol{R^{mxn}}$ is the output measurement matrix with uncertain parameters, $\boldsymbol{c_{ij_{k+1}}}; \boldsymbol{i} \in \{1,2,....,\boldsymbol{m}\}, \boldsymbol{j} \in \{1,2,....,\boldsymbol{n}\}$ assumed to be uncorrelated white Gaussian random variables with the following statistics $\boldsymbol{c_{ij_{k+1}}} \sim \boldsymbol{N}(\bar{\boldsymbol{c}}_{\boldsymbol{ij}}, \boldsymbol{\sigma}^2_{\boldsymbol{c_{ij}}})$, $\boldsymbol{v_{k+1}} \in \boldsymbol{R^m}$ is a zero mean white Gaussian output noise vector with covariance matrix $\boldsymbol{R_{k+1}} = \boldsymbol{E}\{\boldsymbol{v_{k+1} v_{k+1}^T}\} \in \boldsymbol{R^{mxm}}$ $\boldsymbol{M} \in \boldsymbol{R^{nxn}}$ is positive semi-definite weighting matrix for the states, $\boldsymbol{N} \in \boldsymbol{R^{rxr}}$ is positive definite weighting matrix for the control, $\boldsymbol{x_o} \in \boldsymbol{R^n}$ is the initial conditions of the states assumed zero mean random Gaussian vector with covariance matrix $\boldsymbol{P_o} = \boldsymbol{P_{o|o}} = \boldsymbol{E}\{\boldsymbol{x_o x_o^T}\} \in \boldsymbol{R^{nxn}}$, and finally $\boldsymbol{k} \in \{0,1,2,...\}$ is the discrete time instant.

Let $\boldsymbol{b_k} \in \boldsymbol{R^{n^2}}, \boldsymbol{c_{k+1}} \in \boldsymbol{R^{nm}}$ be the parameter vectors defined as:

$$\begin{aligned} \boldsymbol{b_k} &= [\boldsymbol{a}_{11_k}, \boldsymbol{a}_{12_k}, ..., \boldsymbol{a}_{21_k}, \boldsymbol{a}_{22_k}, ...]^{\boldsymbol{T}}, \\ \boldsymbol{c_{k+1}} &= [\boldsymbol{c}_{11_{k+1}}, \boldsymbol{c}_{12_{k+1}}, ..., \boldsymbol{c}_{21_{k+1}}, \boldsymbol{c}_{22_{k+1}}, ...]^{\boldsymbol{T}} \end{aligned} \quad (2)$$

In the above model it is assumed that $\boldsymbol{x_o}, \boldsymbol{b_k}, \boldsymbol{c_{k+1}}, \boldsymbol{w_k}, \boldsymbol{v_{k+1}}$ are all independent. Moreover, it is assumed that the model has the following properties:

$$\begin{aligned} &\boldsymbol{E}\{\boldsymbol{x_k w_j^T}\} = 0, \forall \boldsymbol{k} \le \boldsymbol{j}; \quad \boldsymbol{E}\{\boldsymbol{x_k v_j^T}\} = 0, \forall \boldsymbol{k}, \boldsymbol{j}; \\ &\boldsymbol{E}\{\boldsymbol{y_k v_j^T}\} = 0, \forall \boldsymbol{k} < \boldsymbol{j}; \quad \boldsymbol{E}\{\boldsymbol{x_k b_j^T}\} = 0, \forall \boldsymbol{k} \le \boldsymbol{j}; \\ &\boldsymbol{E}\{\boldsymbol{x_k c_j^T}\} = 0, \forall \boldsymbol{k}, \boldsymbol{j}; \quad \boldsymbol{E}\{\boldsymbol{y_k c_j^T}\} = 0, \forall \boldsymbol{k} < \boldsymbol{j}; \\ &\boldsymbol{E}\{\boldsymbol{b_k c_j^T}\} = 0, \forall \boldsymbol{k}, \boldsymbol{j} \end{aligned} \quad (3)$$

Since the parameters of the system are uncertain, then we have a bilinear estimation problem rather than linear, which intern leads to a non-Gaussian estimation problem. Our objective is to get a good estimator for the state vector, and hence use the estimated states to generate the desired control signal.

3. The Developed Estimator

Let us for the moment consider the following problem:

$$\boldsymbol{x_{k+1}} = \boldsymbol{A_k x_k} + \boldsymbol{w_k} \quad \text{(1'-a)}$$

$$\boldsymbol{y_{k+1}} = \boldsymbol{C_{k+1} x_{k+1}} + \boldsymbol{v_{k+1}} \quad \text{(1'-b)}$$

The system model (1') has the same definitions and properties of the system model (1) in section 2.

State estimation problems with uncertain parameters is usually solved by treating the parameters as static states, i.e. $\boldsymbol{\beta_{k+1}} = \boldsymbol{\beta_k}$ with the prior at k=0 being $\boldsymbol{N}(\bar{\boldsymbol{\beta}}, \boldsymbol{\Sigma})$, where $\bar{\boldsymbol{\beta}}$ is the vector of the mean or nominal values of the parameters and $\boldsymbol{\Sigma}$ is its covariance matrix. This approach increases the dimensionality of the problem, and hence the computational burden. To avoid this difficulty, the nominal values of the parameters will be used in the estimator. However, the impact of this approximation on the dynamics of the estimator will be investigated.

Assume that the filtered estimate $\hat{\boldsymbol{x}}_{\boldsymbol{k|k}}$ and its associated covariance matrix $\boldsymbol{P_{k|k}}$ are given at the $\boldsymbol{k^{th}}$ sampling instant, and used to approximate the conditional probability density function $\boldsymbol{p}(\boldsymbol{x_k} | \boldsymbol{Y^k})$ by Gaussian distribution with conditional mean and covariance matrix as given above.

The filtered estimate of system (1') and its associated covariance matrix are given by:

a) *The predicted estimate of the state vector* $\hat{\boldsymbol{x}}_{\boldsymbol{k+1|k}}$, *its associated covariance matrix* $\boldsymbol{P_{k+1|k}}$, *and the predicted estimate of the output vector* $\hat{\boldsymbol{y}}_{\boldsymbol{k+1|k}}$, *are given by:*

$$\hat{\boldsymbol{x}}_{\boldsymbol{k+1|k}} = \bar{\boldsymbol{A}} \hat{\boldsymbol{x}}_{\boldsymbol{k|k}} \quad (4)$$

$$\boldsymbol{P_{k+1|k}} = \bar{\boldsymbol{A}} \boldsymbol{P_{k|k}} \bar{\boldsymbol{A}}^{\boldsymbol{T}} + \hat{\boldsymbol{\Phi}}_{\boldsymbol{k|k}} \boldsymbol{\Gamma_k} \hat{\boldsymbol{\Phi}}^{\boldsymbol{T}}_{\boldsymbol{k|k}} + \boldsymbol{\Xi_k} + \boldsymbol{Q_k} \quad (5)$$

$$\hat{\boldsymbol{y}}_{\boldsymbol{k+1|k}} = \bar{\boldsymbol{C}} \hat{\boldsymbol{x}}_{\boldsymbol{k+1|k}} \quad (6)$$

b) The filtered estimate of the state vector $\hat{\boldsymbol{x}}_{\boldsymbol{k+1|k+1}}$, *its associated covariance matrix* $\boldsymbol{P_{k+1|k+1}}$, *and the filtered estimate of the output vector* $\hat{\boldsymbol{y}}_{\boldsymbol{k+1|k+1}}$, *are such that:*

$$\hat{x}_{k+1|k+1} \cong \hat{x}_{k+1|k} + K_{k+1}\tilde{y}_{k+1|k} \quad (7)$$

$$K_{k+1} = P_{k+1|k}\bar{C}^T[\bar{C}P_{k+1|k}\bar{C}^T + \hat{\Psi}_{k+1|k}U_{k+1}\hat{\Psi}^T_{k+1|k} + L_{k+1} + R_{k+1}]^{-1} \quad (8)$$

$$P_{k+1|k+1} \cong (I - K_{k+1}\bar{C})P_{k+1|k} \quad (9)$$

$$\hat{y}_{k+1|k+1} \cong \bar{C}\hat{x}_{k+1|k+1} \quad (10)$$

Proof:

a) Derivation of the Prediction Estimator and the Corresponding Covariance Matrix:

Equation ($1^{'}$-a) can be rewritten as:

$$\begin{aligned} x_{k+1} &= (\bar{A} + \tilde{A}_k)(\hat{x}_{k|k} + \tilde{x}_{k|k}) + w_k \\ x_{k+1} &= \bar{A}\hat{x}_{k|k} + \bar{A}\tilde{x}_{k|k} + \tilde{A}_k\hat{x}_{k|k} + \tilde{A}_k\tilde{x}_{k|k} + w_k \end{aligned} \quad (11)$$

where $\bar{A}$ is the matrix contains the nominal (mean) values of the parameters, while $\tilde{A}_k$ contains the perturbations around these nominal values.

Let $\tilde{b}_k = [\tilde{a}_{11_k}, \tilde{a}_{12_k}, ..., \tilde{a}_{21_k}, \tilde{a}_{22_k}, ...]^T \in R^{n^2}$ be a vector contains the deviation of the parameters of the matrices A_k around their nominal values $\bar{A}$, and define:

$$\hat{\Phi}_{k|k} = \begin{bmatrix} \hat{x}^T_{k|k} & O & O..... \\ O & \hat{x}^T_{k|k} & O..... \\ ..... & & \\ O & O & .....\hat{x}^T_{k|k} \end{bmatrix} \in R^{nxn^2}, \qquad \tilde{\Phi}_{k|k} = \begin{bmatrix} \tilde{x}^T_{k|k} & O & O..... \\ O & \tilde{x}^T_{k|k} & O..... \\ ..... & & \\ O & O & .....\tilde{x}^T_{k|k} \end{bmatrix} \in R^{nxn^2} \quad (12)$$

where $O = [0 \quad 0 \quad 0.....] \in R^n$ is a vector of zero elements.

Then, (11) can be rearranged in the following form:

$$x_{k+1} = \bar{A}\hat{x}_{k|k} + \bar{A}\tilde{x}_{k|k} + \hat{\Phi}_{k|k}\tilde{b}_k + \tilde{\Phi}_{k|k}\tilde{b}_k + w_k \quad (13)$$

The predicted value of the state vector is given by:

$$\hat{x}_{k+1|k} = E\{x_{k+1} \mid Y^k\} \quad (14)$$

Using the model properties (3), the predicted estimator is such that:

$$\hat{x}_{k+1|k} = \bar{A}\hat{x}_{k|k} \quad (15)$$

From (13), (15), the prediction error is given by:

$$\tilde{x}_{k+1|k} = \bar{A}\tilde{x}_{k|k} + \hat{\Phi}_{k|k}\tilde{b}_k + \tilde{\Phi}_{k|k}\tilde{b}_k + w_k \quad (16)$$

The covariance matrix of the estimation error is such that:

$$P_{k+1|k} = E\{\tilde{x}_{k+1|k}\tilde{x}^T_{k+1|k}\} \quad (17)$$

Using the model properties (3), $P_{k+1|k}$ is given by:

$$P_{k+1|k} = \bar{A}P_{k|k}\bar{A}^T + \hat{\Phi}_{k|k}\Gamma_k\hat{\Phi}^T_{k|k} + \Xi_k + Q_k \quad (18)$$

where:

$$\Gamma_k = diag[\sigma^2_{a_{11_k}} \quad \sigma^2_{a_{12_k}} \quad .....\sigma^2_{a_{nn_k}}] \quad (19\text{-a})$$

$$\Xi_k = diag[e_{11_k} \quad e_{22_k} \quad .....e_{nn_k}] \quad (19\text{-b})$$

$$e_{ii_k} = \sum_{j=1}^{n} P_{k|k_{jj}}\sigma^2_{a_{ij_k}} \quad (19\text{-c})$$

Equation ($1^{'}$-b) can also be written in the form:

$$\begin{aligned} y_{k+1} &= (\bar{C} + \tilde{C}_{k+1})(\hat{x}_{k+1|k} + \tilde{x}_{k+1|k}) + v_{k+1} \\ y_{k+1} &= \bar{C}\hat{x}_{k+1|k} + \bar{C}\tilde{x}_{k+1|k} + \tilde{C}_{k+1}\hat{x}_{k+1|k} + \tilde{C}_{k+1}\tilde{x}_{k+1|k} + v_{k+1} \end{aligned} \quad (20)$$

where $\bar{C}$ is the matrix contains the nominal (mean) values of the parameters, while $\tilde{C}_{k+1}$ contains the perturbations around these nominal values.

Let $\tilde{c}_{k+1} = [\tilde{c}_{11_{k+1}}, \tilde{c}_{12_{k+1}}, ..., \tilde{c}_{21_{k+1}}, ..]^T \in R^{nm}$ be the vector contains the deviation of the parameters of the matrix C_{k+1} around their nominal values $\bar{C}$. Then, by rearranging (20), one gets:

$$y_{k+1} = \bar{C}\hat{x}_{k+1|k} + \bar{C}\tilde{x}_{k+1|k} + \hat{\Psi}_{k+1|k}\tilde{c}_{k+1} + \tilde{\Psi}_{k+1|k}\tilde{c}_{k+1} + v_{k+1} \quad (21)$$

where:

$$\hat{\Psi}_{k+1|k} = \begin{bmatrix} \hat{x}^T_{k+1|k} & O & O..... \\ O & \hat{x}^T_{k+1|k} & O..... \\ ..... & & \\ O & O & .....\hat{x}^T_{k+1|k} \end{bmatrix} \in R^{mx(nm)}, \qquad \tilde{\Psi}_{k+1|k} = \begin{bmatrix} \tilde{x}^T_{k+1|k} & O & O..... \\ O & \tilde{x}^T_{k+1|k} & O..... \\ ..... & & \\ O & O & .....\tilde{x}^T_{k+1|k} \end{bmatrix} \in R^{nx(nm)} \quad (22)$$

From (21), the predicted output is given by:

$$\hat{y}_{k+1|k} = \bar{C}\hat{x}_{k+1|k} \quad (23)$$

Accordingly, $\tilde{y}_{k+1|k}$ is such that:

$$\tilde{y}_{k+1|k} = \bar{C}\tilde{x}_{k+1|k} + \hat{\Psi}_{k+1|k}\tilde{c}_{k+1} + \tilde{\Psi}_{k+1|k}\tilde{c}_{k+1} + v_{k+1} \quad (24)$$

Hence:

$$\begin{aligned} P_{\tilde{y}_{k+1|k}\tilde{y}_{k+1|k}} &= E\{\tilde{y}_{k+1|k}\tilde{y}_{k+1|k}\} \\ &= \bar{C}P_{k+1|k}\bar{C}^T + \hat{\Psi}_{k+1|k}U_{k+1}\hat{\Psi}^T_{k+1|k} + L_{k+1} + R_{k+1} \end{aligned} \quad (25)$$

where:

$$U_{k+1} = diag[\sigma^2_{c_{11_{k+1}}} \quad \sigma^2_{c_{12_{k+1}}} \quad .....\sigma^2_{c_{mn_{k+1}}}]$$

$$L_{k+1} = diag[l_{11_{k+1}} \quad l_{22_{k+1}} \quad .....l_{mm_{k+1}}] \quad (26)$$

$$l_{k+1_{ii}} = \sum_{j=1}^{n} P_{k+1|k_{jj}}\sigma^2_{c_{ij_{k+1}}}$$

b) Derivation of the Filtered Estimator and the Corresponding Covariance Matrix:

The filtered estimate of x_{k+1} is given by:

$$\begin{aligned} \hat{x}_{k+1|k+1} &= E\{x_{k+1} \mid Y^k, y_{k+1}\} \\ &\cong \hat{x}_{k+1|k} + P_{x_{k+1}\tilde{y}_{k+1|k}}P^{-1}_{\tilde{y}_{k+1|k}\tilde{y}_{k+1|k}}\tilde{y}_{k+1|k} \end{aligned} \quad (27)$$

$$\begin{aligned} P_{x_{k+1}\tilde{y}_{k+1|k}} &= E\{x_{k+1}\tilde{y}^T_{k+1|k}\} \\ &= E\{(\hat{x}_{k+1|k} + \tilde{x}_{k+1|k})\tilde{y}^T_{k+1|k}\} \end{aligned} \quad (28)$$

Using (24) in (28), and due to the independency between $\tilde{x}_{k+1|k}, \tilde{c}_{k+1}, v_{k+1}$, one gets:

$$P_{x_{k+1}\tilde{y}_{k+1|k}} = P_{k+1|k}\bar{C}^T \quad (29)$$

Let $K_{k+1} = P_{x_{k+1}\tilde{y}_{k+1|k}} P^{-1}_{\tilde{y}_{k+1|k}\tilde{y}_{k+1|k}}$ (30)

Using (25), (29) in (30) one can get K_{k+1} as given by (8). Hence:

$$\hat{x}_{k+1|k+1} \cong \hat{x}_{k+1|k} + K_{k+1}\tilde{y}_{k+1|k} \quad (31)$$

The filter estimation error is such that:

$$\tilde{x}_{k+1|k+1} \cong \tilde{x}_{k+1|k} - K_{k+1}\tilde{y}_{k+1|k} \quad (32)$$

Using (32), the covariance matrix of the filter estimation error is such that:

$$P_{k+1|k+1} \cong (I - K_{k+1}\bar{C})P_{k+1|k} \quad (33)$$

4. Control Design

In the system model (1), since parameters of the system as well as the states are random, the system is bilinear rather than linear. Therefore, the separation principle does not hold. However, the problem will be treated as deterministic and the resulted control strategy will be applied to the stochastic problem. It is obvious in this case that the resulting closed loop control system is suboptimal rather than optimal.

Let us consider the following servo-mechanism discrete-time linear deterministic system:

$$\min J = \frac{1}{2}\sum_{k=k_o}^{k_f-1}\left[\left\|x_k - x^d\right\|^2_M + \left\|u_k\right\|^2_N\right] \quad (34)$$

Subject to:

$$x_{k+1} = \bar{A}x_k + B_k u_k + d \quad (35)$$

where $x_k \in R^n$ is the state vector assumed to be deterministic, $\bar{A} \in R^{nxn}$ is the matrix contains the nominal values of the parameters, while other variables are as defined in section 2.

By writing the Hamiltonian of this problem, and from the necessary conditions of optimality, the expression for the control is such that [13]:

$$u_k = -N^{-1}B_k^T\bar{A}^{T^{-1}}\left[\left(P_{rk} - M\right)x_k + \xi_k + Mx^d\right] \quad (36)$$

where $P_{r_k} = M + \bar{A}^T P_{r_{k+1}}\Im^{-1}\bar{A}$ *with* $P_{r_{k_f}} = [0]$ (37)

with $\Im = I + B_k N^{-1}B_k^T P_{r_{k+1}}$

(38)

$$\xi_k = -\bar{A}^T P_{r_{k+1}}\Im^{-1}B_k N^{-1}B_k^T\xi_{k+1} - Mx^d + \bar{A}^T P_{r_{k+1}}\Im^{-1}d + \bar{A}^T\xi_{k+1} \quad \textit{with}\ \xi_{k_f} = 0 \quad (39)$$

Since the state vector x_k is not available for direct measurement, the estimate of this vector $\hat{x}_{k|k}$ will be used in conjunction with the state feedback controller (36). Therefore, the dynamics of the observer-based closed loop stochastic controller at the k^{th} iteration can be summarized as follows:

a) Calculate, off-line, P_{rk}, ξ_k for $k = k_o, ..., k_{f-1}$ using (37)-(39).

b) Calculate the control signal using (36).

c) Calculate the predicted value of the state vector as given by:

$$\hat{x}_{k+1|k} = \hat{x}_{k|k} + B_k u_k \quad (40)$$

d) The covariance matrix $P_{k+1|k}$, and the predicted estimate of the output $\hat{y}_{k+1|k}$ are as given by (5), (6).

e) The filtered estimate of the state vector $\hat{x}_{k+1|k+1}$, its associated covariance matrix $P_{k+1|k+1}$, and the filtered estimate of the output vector $\hat{y}_{k+1|k+1}$ are as given by (7)-(10).

The flowchart of the observer-based controller is given in the following section.

5. The Flowchart of the Algorithm

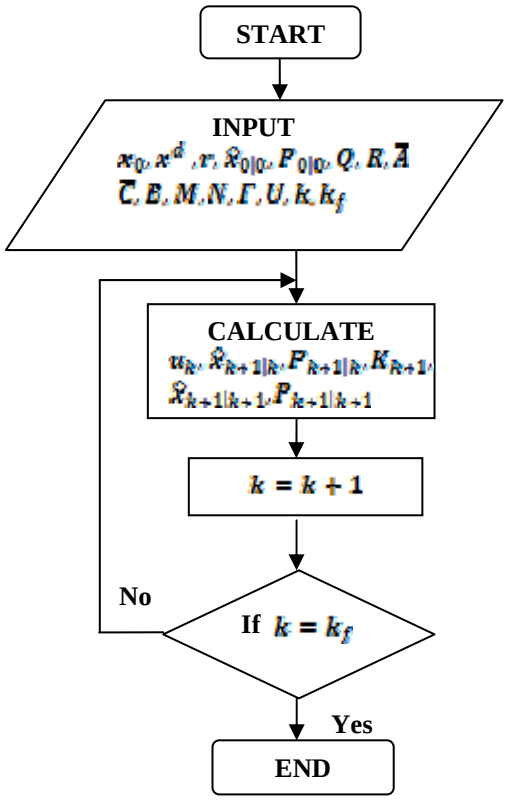

6. Simulation Results

6.1 ***Illustrative Example*** **:**

To investigate the effectiveness of the developed estimator, we employ firstly the following numerical values of a three dimension (3-D) discrete-time linear system model:

$$\bar{A} = \begin{bmatrix} 1 & 0.009983 & 0 \\ -0.009889 & 0.9949 & 0.0091 \\ -1.98 & -0.9874 & 0.8305 \end{bmatrix}, \bar{C} = [1 \quad 0 \quad 0],$$

$x_o = [1 \quad 1 \quad 1]^T$, $\hat{x}_{o|o} = [0 \quad 0 \quad 0]^T$,

$P_{o|o} = I$ where $I \in R^{3x3}$ is the unity matrix.

The states of the system are estimated using the developed filter, KF, and EKF. Different values of Q, R and different levels of uncertainties in the system parameters are used in our simulation. For comparison purposes, Monte Carlo simulation is applied to explore the qualitative behavior of the root mean square errors

(RMSE) of the estimated states resulting from the application of the three filters. This is defined by:

$$RMSE\,(x_j(k),\hat{x}_j(k\mid k)) = \sqrt{\frac{\sum_{i=1}^{MI}(x_j(k)-\hat{x}_j(k\mid k))^2}{MI}}$$

for $\forall k = 1,...,k_f \quad and\ j = 1,....,n$ (41)

where *MI* is the number of Monte Carlo iterations.
Moreover, the root mean square error index (RMSE index) for each state is calculated using the following formula:

$$RMSE\ index(x_j) = \sqrt{\frac{\sum_{k=0}^{k_f}\sum_{i=1}^{MI}(x_j(k)-\hat{x}_j(k\mid k))^2}{(k_f)(MI)}} \quad (42)$$

Table (1) shows the RMSE indices calculated over 100 Monte Carlo iterations for each case study while using the three filters.

Table 1: RMSE index (*MI* = 100)

Case	x_i	Q	R	Pn%	RMSE index		
					MKF	KF	EKF
a	1	0.1	0.1	10	0.2597	0.269	Div.
b		0.5	1.0	20	0.7947	1.821	
c		0.5	1.0	30	0.8235	8.233	
d		1.0	1.0	30	0.8717	26.444	
a	2	0.1	0.1	10	1.8834	1.887	Div.
b		0.5	1.0	20	19.687	25.099	
c		0.5	1.0	30	61.726	66.207	
d		1.0	1.0	30	576.66	686.21	
a	3	0.1	0.1	10	10.054	10.09	Div.
b		0.5	1.0	20	95.214	125.57	
c		0.5	1.0	30	299.092	345.97	
d		1.0	1.0	30	2.23e+3	2.87e+3	

From Table 1, the proposed filter has the best performance in all cases. It has the minimum RMSE index calculated over 100 Monte Carlo iterations, whereas the (EKF) fails to estimate the states since it diverges. The RMSE plots of the states using the three filters for Case-a are shown in Figures (1-3), and for Case-b are shown in Figures (4-6).

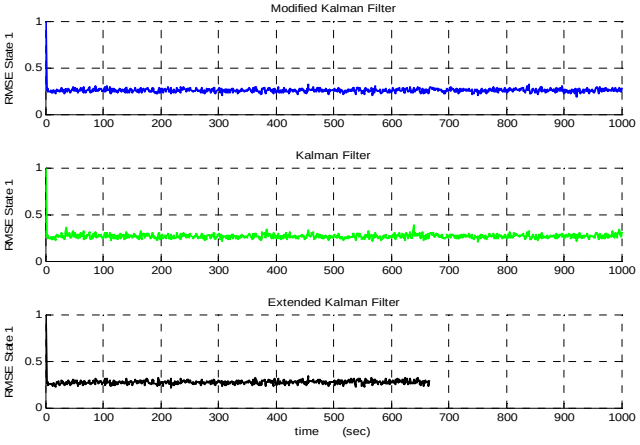

Figure 1: RMSE of $x1$ (Case-a).

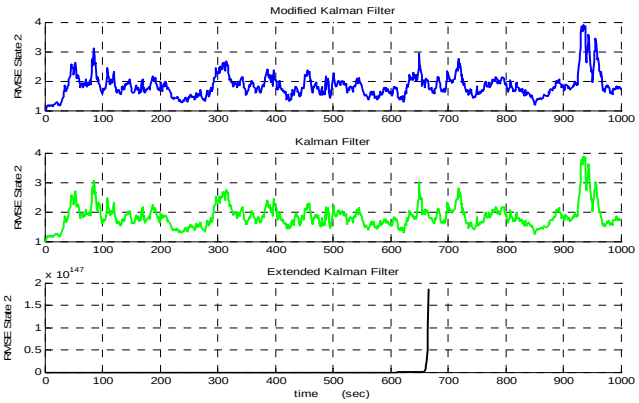

Figure 2: RMSE of $x2$ (Case-a).

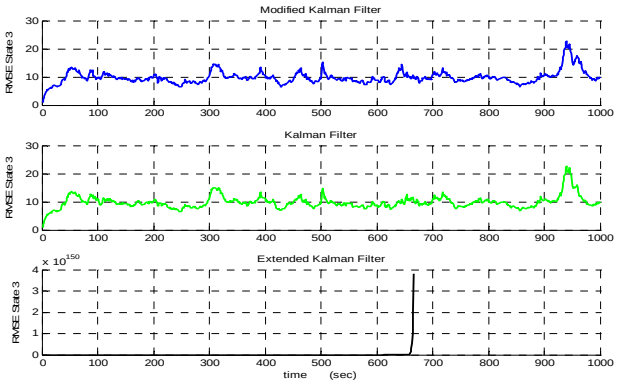

Figure 3: RMSE of $x3$ (Case-a).

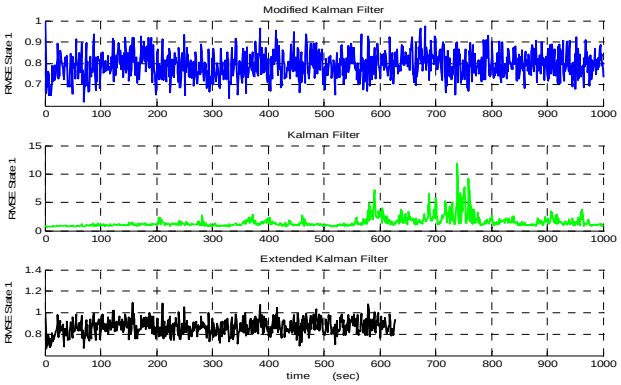

Figure 4: RMSE of $x1$ (Case-b).

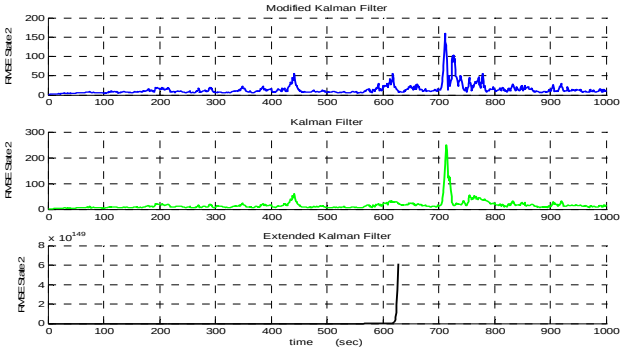

Figure 5: RMSE of $x2$ (Case-b).

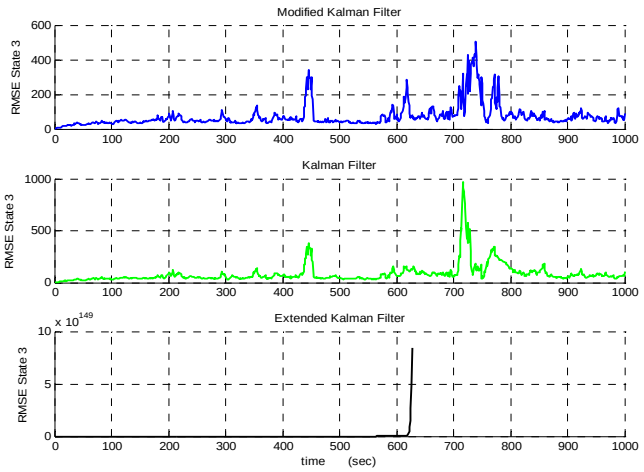

Figure 6: RMSE of x_3 (case-b)

6.2 ***Case Study*:**

The transfer function of a DC motor is given by [14]:

$$\frac{\theta(s)}{E(s)} = \frac{K_T}{s[(sL_a + R')(sJ + B) + K_T K_b]} \quad (43)$$

where,

θ is the motor angle displacement.

$\dot{\theta}$ is the motor rotating speed, where $\dot{\theta} = \frac{d\theta}{dt}$.

i_a is the armature winding current.

E is the applied voltage.

K_T is the motor torque constant.

K_b is the back emf constant.

L_a is the armature winding inductance.

R' is the armature winding resistance.

J is the moment of inertia of rotor and load.

B is the damping coefficient.

The state vector x is defined by $x^T = [\theta \quad \dot{\theta} \quad i_a]^T$.

For the above model, it is assumed that the rotating speed of the motor $\dot{\theta}$ is measured at the output.

6.2.a) *State estimation under no control:*

The continuous state equation of the DC motor is:

$$\frac{d}{dt}\begin{bmatrix}\theta \\ \dot{\theta} \\ i_a\end{bmatrix} = \begin{bmatrix}0 & 1 & 0 \\ 0 & -B/J & K_T/J \\ 0 & -K_b/L_a & -R/L_a\end{bmatrix}\begin{bmatrix}\theta \\ \dot{\theta} \\ i_a\end{bmatrix} + \begin{bmatrix}0 \\ 0 \\ 1/L_a\end{bmatrix} E \quad (44)$$

$$y = [0 \quad 1 \quad 0]\begin{bmatrix}\theta \\ \dot{\theta} \\ i_a\end{bmatrix} \quad (45)$$

where E=150 is the reference input.

The above model is discretized using Euler's method with sampling period Ts= 0.005. Therefore, the discrete model is such as:

$$\begin{bmatrix}\theta_{k+1} \\ \dot{\theta}_{k+1} \\ i_{ak+1}\end{bmatrix} = \begin{bmatrix}1 & 0.005 & 0 \\ 0 & 0.9994 & 0.0749 \\ 0 & -0.9632 & -0.9238\end{bmatrix}\begin{bmatrix}\theta_k \\ \dot{\theta}_k \\ i_{ak}\end{bmatrix} + \begin{bmatrix}0 \\ 0 \\ 0.5023\end{bmatrix} 150 \quad (46)$$

$$y_{k+1} = [0 \quad 1 \quad 0]\begin{bmatrix}\theta_{k+1} \\ \dot{\theta}_{k+1} \\ i_{ak+1}\end{bmatrix} \quad (47)$$

where, the system model is corrupted by an input noise $\boldsymbol{w}(\boldsymbol{k}) \sim \boldsymbol{N}(0, 0.1)$ and measurement disturbance $\boldsymbol{v}(\boldsymbol{k}) \sim \boldsymbol{N}(0, 0.01)$.

The system parameters K_T, K_b, L_a and R', are assumed to be uncertain with a standard deviation equals to certain percentage P_n of their nominal values.

$\boldsymbol{x_o} = [10 \quad 80 \quad 0.5]^{\boldsymbol{T}}, \hat{\boldsymbol{x}}_{\boldsymbol{o|o}} = [5 \quad 79 \quad 1]^{\boldsymbol{T}}, \boldsymbol{P_{o|o}} = \boldsymbol{I} \in \boldsymbol{R}^{3x3}$

The RMSE indices of the states calculated over 100 Monte Carlo iterations using the three filters are shown in Table 2. RMSE plots for Case-b are shown in Figures (7-9).

Table 2: RMSE index, Q=0.1, R=0.01 (*MI* = 100).

Case	State	Pn%	RMSE index		
			MKF	KF	EKF
a	θ	5	8.6057	8.6057	Div.
b		10	9.3070	9.3070	
a	$\dot{\theta}$	5	0.1034	0.1231	
b		10	0.1044	0.2213	
a	i_a	5	6.6085	12.4121	
b		10	15.5597	34.4408	

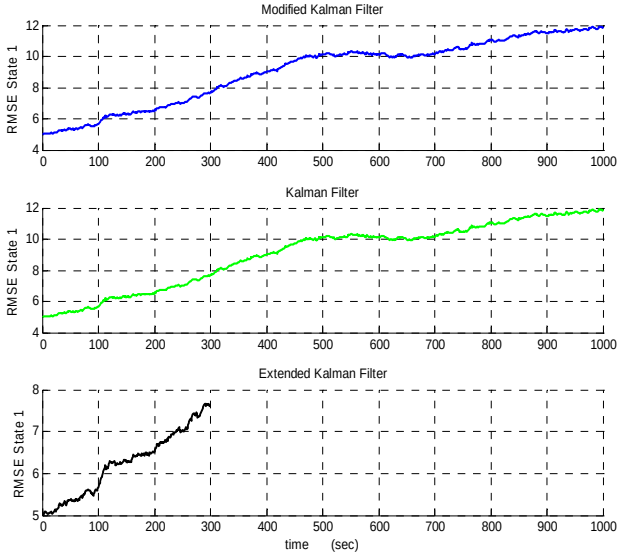

Figure 7: RMSE of θ (case-b)

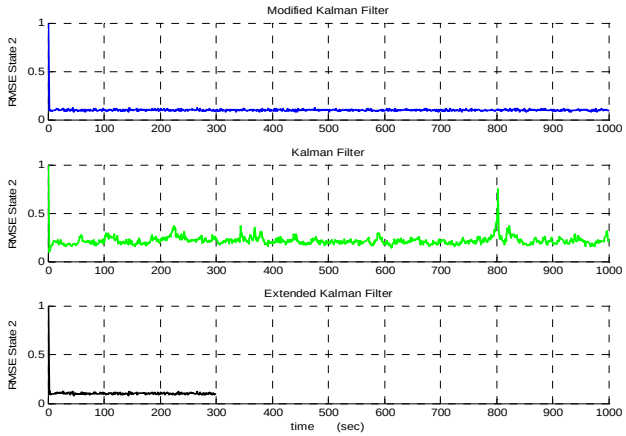

Figure 8: RMSE of $\dot{\theta}$ (Case-b).

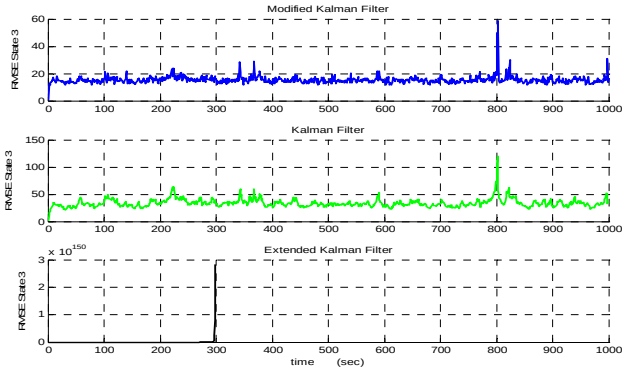

Figure 9: RMSE of i_a (Case-b).

From the simulation results, the proposed estimation procedure showed to be the best, and leads to the minimum value of the RMSE index. Therefore, it will be used in the implementation of the observer-based controller as shown in Figure (10).

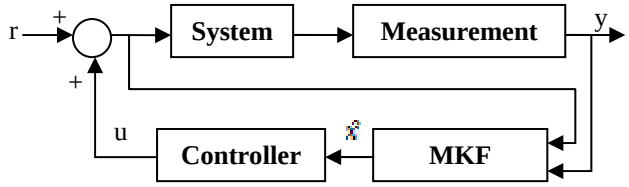

Figure 10: Block diagram of the closed loop system.

6.2.b) *Observer-based Controller*:

For the problem in hand, it is desired to regulate the system to the rotating speed $\dot{\theta}^d = 76.8085\,rpm$. The initial values for the states, the estimated states, and covariance matrix P are as follows: $\boldsymbol{x_o} = [5 \;\; 40 \;\; 1]^T, \hat{\boldsymbol{x}}_{o|o} = [0 \;\; 0 \;\; 0]^T, \boldsymbol{P_{o|o}} = \boldsymbol{I} \in \boldsymbol{R}^{3x3}$

The state weighting matrix is $\boldsymbol{M} = diag[0 \;\; 1 \;\; 1]$, the control weighting matrix is $\boldsymbol{N}$ =[1], the covariance matrix of the input noise is $Q = 0.1I$, the covariance matrix of the output noise is $\boldsymbol{R} = 0.01$, and the percentage change in the parameters is $P_n = 10\%$. The actual and estimated closed loop trajectories as well as the control signal are shown in Figures (11-14).

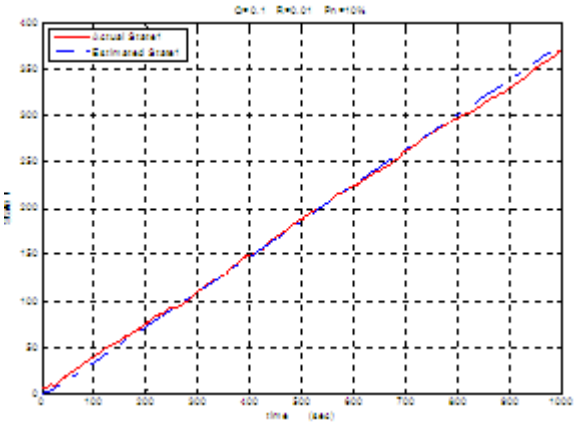

Figure 11: Actual and Estimated motor angle displacement θ.

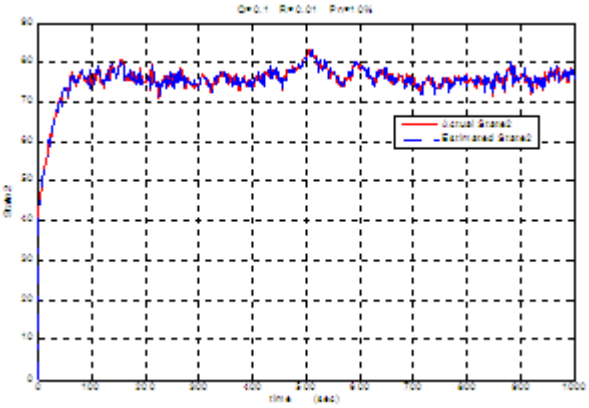

Figure 12: Actual and Estimated motor rotating speed $\dot{\theta}$.

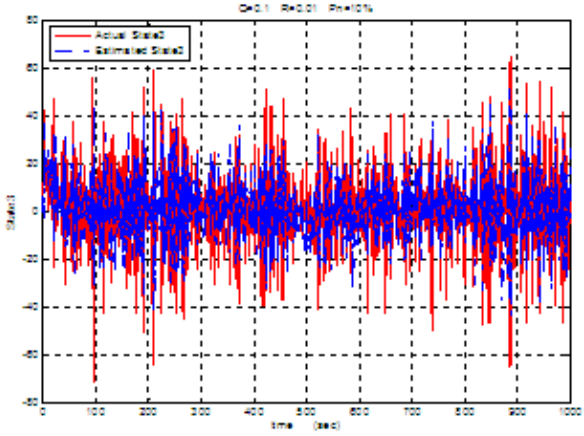

Figure 13: Actual and Estimated armature winding current i_a.

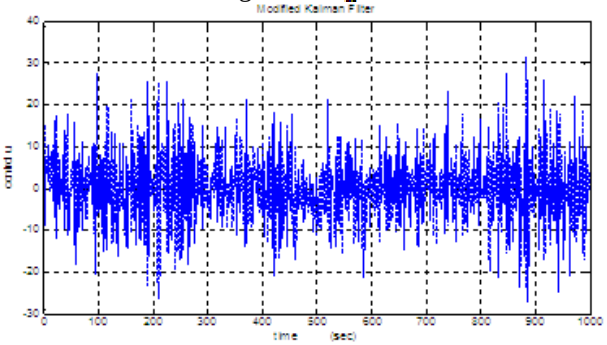

Figure 14: Feedback Control u.

7. Conclusion

In this paper, an observer-based controller is developed for linear stochastic discrete-time dynamical systems with uncertain parameters. A state estimator, based on Kalman filter, is firstly developed which incorporates the statistical information of the uncertain parameters in its structure. Although this problem is treated in the literature as a nonlinear estimation problem; with the developed approach the system is still treated as linear and without any increase in its dimensionality. As a result, we have less computational burden and better numerical properties. Based on the developed filter, an observer-based feedback controller is proposed. Simulation of different illustrative examples showed that the state estimation using the proposed filter is better than KF, while the EKF diverged and failed to estimate the system states. Moreover, although the separation principle does not hold, simulation results showed that the regulated system is asymptotically stable, and the states of the DC motor reached the desired ones. However, it is still necessary to analyze the stability of the controlled system more rigorously in a theoretical frame work. This problem will be treated in the future.

8. References

[1] D.G. Luenberger, Obserevers for multivariable systems. IEEE Trans. Automat Control AC-11, pp.190-7, 1966.

[2] R.E. Kalman R.E. , Anew approach to linear filtering and prediction problems. Transactions of ASME-Journal of Basic engineering, 82-D, pp. 35-45, 1960.

[3] T. Cimen State-dependent Riccati equation (SDRE): A survey. Proceeding of the 17th World Congress, The International Federation of Automatic Control, Seoul, Korea, July 6-11, pp.3761-3774, 2008.

[4] E.L. Haseltine and J.B. Rawlings, Critical evaluation of extended Kalman filtering and moving horizon estimation. Ind.Eng.Chem. Res.,vol. 44, no. 8, 2005

[5] M.S. Arulampalam, S. Maskell, N. Gordon, and T. Clapp A., Tutorial on Particle Filters for Online Nonlinear/Non-Gaussian Bayesian Tracking. IEEE Trans.On Signal Processing, vol. 50, no.2, pp174-188, Feb. 2002.

[6] G. Evensen , Data Assimilation: The Ensemble Kalman Filter. Springer-Berli, 2009.

[7] E.A. Wan and R. var der Merwe, The unscented Kalman filter for nonlinear estimation. Proc. IEEE Symposium on Adaptive Systems for Signal Processing, Comm. And Control, Lake Louise, Canada, pp. 153-158, Oct. 2000.

[8] D. Simon, Optimal State Estimation: Kalman, H infinity and Nonlinear approach.Wiley, 2006.

[9] Y. Govindarajan and D. Sivakumar , Attack Analysis of Robust Watermarking Technique for Patent Infringement.Graphics,Vision and Image processing GVIP, vol. 11, no.3, pp39-45, Jul. 2011.

[10] A. Asokan and D. Sivakumar, Fault Detection and Diagnosis for a Three-tank system using Structured Residual Approach. Automatic Control and System Engineering ACSE, vol. 7, no.2, pp1-8, Nov. 2007.

[11] S.Abraham Lincon and D.Sivakumar and J.Prakash, State and Fault Parameter Estimation Applied To Three-Tank Bench Mark Relying On Augmented State Kalman Filter. Automatic Control and System Engineering ACSE, vol.7, no.1, pp 33-41, May 2007.

[12] J.S. Meditch, Stochastic Optimal LinearEstimation and Control. McGraw Hill, 1965.

[13] D.E. Kirk, Optimal Control Theory: An Introduction, Englewood Cliffs, N.J., Prentice Hall, 1970.

[14] S.K. Yang , An experiment of state estimation for predictive maintenance using Kalamn filter on a DC motor. Reliability Engineering and System Safety, 2002.

Biographies

Mohamed F. Hassan was born in Cairo, Egypt on June 21, 1947. He received the B.Sc. and M.Sc. degrees in Electrical Engineering from Cairo University, Faculty of Engineering, Cairo, Egypt in 1970 and 1973 respectively, and D.Sc. (Doctor d'Etat) in Systems Science and Automatic Control from Paul Sabatier University, Toulouse, France, 1978. He is a Professor of Systems Science and Control Engineering in the Electrical, College of Engineering and Petroleum, Kuwait University since 2002 till now. He has been a faculty member in Electronics and Communication Department, Faculty of Engineering, Cairo University since 1978 where he held the positions of Assistant Professor associate Professor and Professor . His research activities are in the areas of large scale systems, optimization theory, stochastic control theory, estimation theory and adaptive control. Prof Hassan is a co-author of one book, author of many book chapters and encyclopedia chapters . Moreover, he is an author and co-author of more than 150 technical papers in most of the international journals and conferences. Prof. Hassan is a reviewer of many international journals and conferences.

Hala A. Mourad was born in Kuwait on January 11, 1966. She received the B.Sc. and M.Sc. degrees in Electrical Engineering from Kuwait University, College of Engineering and Petroleum, Kuwait in 1987 and 2011 respectively.

www.icgst.com

A Novel Nine-Level MPC Inverter for Direct Torque Control Induction Motor Drive

O. Chandra Sekhar, K.Chandra Sekhar
Dept. of Electrical and Electronics Engg, Vignan`s Lara Institute of Technology and Science, Vadlamudi, Guntur, India
Dept.of Electrical and Electronics Engg, R.V.R & J.C College of Engg, Chowdavaram, Guntur, India
Sekhar.obbu@gmail.com,cskoritala@gmail.com

Abstract
In this paper a novel nine–level inverter system for Direct Torque Control (DTC) induction motor drive is presented. DTC strategy of a nine–level Multi Point Clamped (MPC) Voltage Source Inverter (VSI) fed induction motor is implemented. Nine-level MPC inverter is an advanced technology and are commonly applied to high power electrical drives instead of the two-level VSI.Nine-level inverter has 729 space vector switching states and there are 106 effective vectors are possible. The proposed nine-level inverter scheme is capable for enough degrees of freedom to control both electromagnetic torque and stator flux with very low ripple. From the simulation results shows that feeding electrical drive with nine-level inverter can greatly improves the drive performance as compared to the seven-level inverter. The performance of this control method has been demonstrated by simulations performed using a versatile simulation package, Matlab/Simulink.

Keywords: *DTC, Nine-level inverter Multi point Clamping, Switching table, Induction motor, Matlab/Simulink.*

1. Introduction
Multilevel converters have recently increased interest in the research and industry communities [3]–[7]. In these kind of converters, the output voltage can take several discrete levels of equal magnitude. The multilevel converter first proposed in [1] was aimed at reducing the harmonic content of generated voltage or current waveforms. The harmonic content of such a waveform is greatly reduced, if compared with a two-level waveform. Nowadays, there are three prominent multilevel topologies. Multilevel structures derived from those proposed in [2] and [3] are known as diode-clamped (or neutral-point-clamped) and flying-capacitor multilevel converters, respectively. Both of them are based on a serial connection of low-voltage power semiconductors. The use of voltage clamps to equally share the input voltage between the serial-connected devices and at the same time having a multilevel output voltage is a common feature of these two structures. Thus, by this means, the known problems posed by the serial connection of power semiconductors are avoided and a multilevel output voltage is also possible.

Feeding electrical motors with multilevel inverters can greatly improve the motor performance. The harmonic content of the voltage applied to the motor's terminals will be greatly reduced. Recently, the high *dv*/*dt* produced by modern power electronic based inverters has been identified as the source of several motor failures [8], [9].The ability of multilevel inverters to deliver a multistepped voltage waveform will prevent motor failures by reducing the voltage change rate of the applied voltage. Any of the three prominent multilevel topologies can be used in motor drive applications.

MPC is so called since in their architecture there are several points clamped to specific voltages using some components. Even diode-clamped converters belong to this family because the bus between two switches is clamped by a clamping diode. Furthermore, when the number of voltage level is odd, the converters are called Neutral Point Clamped (NPC) because the neutral point is clamped, has found wide application in medium-voltage high-power applications [10][11]. The main features of the MPC converter include reduced *dv*/*dt* and Total Harmonic Distortion (THD) in its AC output voltages in comparison to the conventional two level converters. As in any multilevel converter it can be used in the medium-voltage applications to reach a certain voltage level without series connection of power semiconductors.

In principle, DTC method is based on instantaneous space vector theory. By optimal selection of the space voltage vectors in each sampling period, DTC achieves effective control of the electromagnetic torque and the stator flux on the basis of the errors between theirs references and estimated values. It is possible to directly control the inverter states through a switching table, in order to reduce the torque and flux errors within the desired bands limits[12][13]. The present work is based on the study of the application of DTC to the nine-level MPC VSI, and the advantages that can be obtained from using this topology when compared to the seven-level inverter.

The paper is organized as follows: the concept of nine - level MPC VSI is discussed in section 2 and representation of proposed DTC scheme is discussed in section 3. The simulation results and discussion of the proposed method are exposed at the next section. Finally conclusions are given in the last section

2. Nine-Level MPC VSI and Related Output Voltage Vectors

The architecture of MPC is several points clamped to specific voltages using some components. Even diode-clamped converters belong to this family because the bus between two switches is clamped by a clamping diode. Furthermore, when the number of voltage level is odd, the converters are called Neutral Point Clamped (NPC) because the neutral point is clamped. As Figure.1 shows, the 9-level leg is completely different: in MPCs the voltages are clamped using couples switch-diode instead of using a simple diode. Anyway, given a number of levels, the number of switches needed by MPC is the same needed by diode-clamped. The control of MPC leg is more complicated in the respect of other topologies. Even this kind of converter allows finding complementary couples of switches. The constrain so introduced is not physiologically necessary, but it is a simple way to simplify the control scheme and the switching table (Table I).

TABLE I
SWITCHING STATES OF A NINE-LEVEL INVERTER

T_1	T_2	T_3	T_4	T_5	T_6	T_1'	T_2'	T_3'	T_4'	T_5'	T_6'	V
1	0	0	0	0	0	1	0	0	0	0	0	$-4U_0$
0	1	1	1	0	1	1	0	0	0	0	0	$-3U_O$
0	0	1	0	0	1	1	1	0	0	1	0	$-2U_0$
0	0	1	0	0	1	0	0	1	1	1	1	$-U_0$
0	0	0	1	1	1	1	0	0	0	0	0	0
1	1	1	0	0	0	1	1	0	0	0	1	0
0	1	1	1	1	1	0	0	1	0	0	0	U_0
0	1	1	0	1	1	1	0	0	0	0	0	$2U_0$
0	0	1	1	1	1	0	0	1	1	0	0	$3U_0$
1	1	0	0	1	1	1	0	0	0	0	0	$4U_0$

Furthermore, to avoid shortcut, T_5 and T_6 must be complementary controlled. The same must happens for T'_5 and T'_6. Table I is a possible switching table for a 9-level MPC leg; there is an intra-phase redundancy only for the middle level. Anyway, it is better to have T_6 turned on in order to limit the reverse voltage drop uponT_3.Dependently on the switching table used, the maximum reverse voltage drop over the components changes and a preliminary analysis must be done to choose the suitable component. Moreover, the switches in the middle of the leg must carry twice the voltage of the others.

The DC bus voltage of 9-level inverter is split into nine levels by using eight DC capacitors C_1,C_2,C_3,C_4,C_5,C_6,C_7 and C_8 as shown in figure1. The voltage across the switches is $1/8^{th}$ of the DC bus voltage, switching losses are cut in $1/8^{th}$ with reduced harmonics of output waveforms for the same switching frequency, and power rating is increases.

Relatively to the 7-level inverter which is only capable to produce 343 space vector voltages, a 9-level inverter has 9^3=729 switching states are possible as shown in figure. If voltages of eight capacitors are equivalent, some switching vectors are overlapped and there are 106 effective vectors.

According to the magnitude of the voltage vectors, we divided them into thirteen different groups:

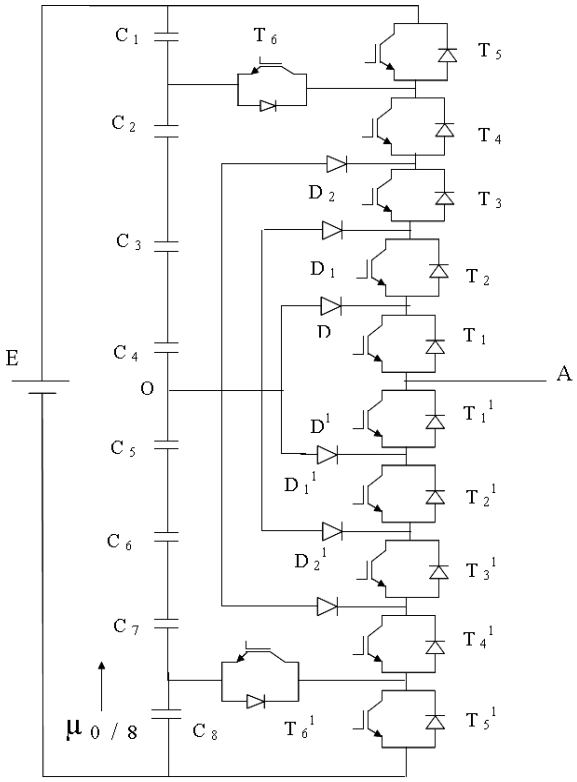

Figure.1: Nine-level multi point Clamped Inverter leg

TABLE II
Magnitudes of the voltage vectors

Group	Magnitudes of the voltage vectors
1	$[V_0]$
2	$[V_1, V_2, V_3, V_4, V_5, V_6]$
3	$[V_{44}, V_{45}, V_{46}, V_{47}, V_{48}, V_{49}]$
4	$[V_{123}, V_{124}, V_{125}, V_{126}, V_{127}, V_{128}]$
5	$[V_{135}, V_{137}, V_{139}, V_{141}, V_{143}, V_{145}]$,
6	$[V_{180}, V_{181}, V_{182}, V_{183}, V_{184}, V_{185}, V_{186}, V_{188}, V_{190}, V_{192}, V_{194}, V_{196}]$
7	$[V_{250}, V_{251}, V_{252}, V_{253}, V_{254}, V_{255}, V_{256}, V_{258}, V_{260}, V_{262}, V_{264}, V_{266}]$
8	$[V_{303}, V_{304}, V_{305}, V_{306}, V_{307}, V_{308}]$
9	$[V_{395}, V_{396}, V_{397}, V_{398}, V_{399}, V_{400}]$
10	$[V_{488}, V_{489}, V_{490}, V_{491}, V_{492}, V_{493}, V_{494}, V_{495}, V_{496}, V_{498}, V_{500}, V_{502}, V_{504}, V_{506}]$
11	$[V_{588}, V_{589}, V_{590}, V_{591}, V_{592}, V_{593}, V_{594}, V_{595}, V_{596}, V_{598}, V_{600}, V_{602}, V_{604}, V_{606}]$
12	$[V_{676}, V_{677}, V_{678}, V_{679}, V_{680}, V_{681}, V_{682}, V_{683}, V_{684}, V_{685}, V_{686}]$
13	$[V_{686}, V_{688}, V_{690}, V_{692}, V_{694}, V_{696}]$

The space vector modulation diagram of 9-level inverter is divided into six sextants, and each sextant is divided into sixty-four triangles regions in order to show the vectors nearest to the reference voltage as shown in figure 2 and 3.

The voltage vectors of 9-level inverter are divided into thirteen groups as shown in table II. The procedure of selection of voltage vectors is similar to that of 3-level inverter is discussed in [8].

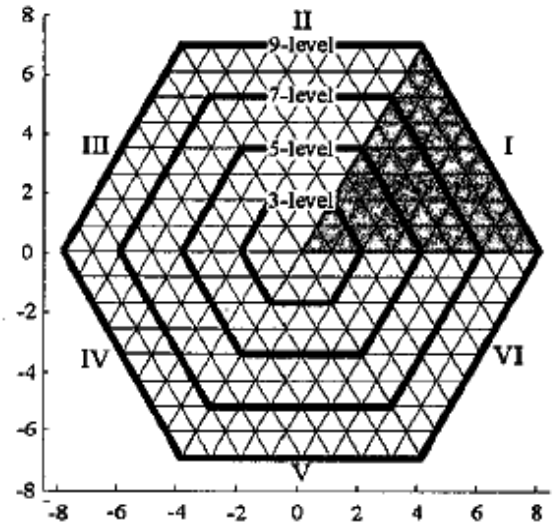

Figure.2: voltage vectors of 9-level MPC VSI

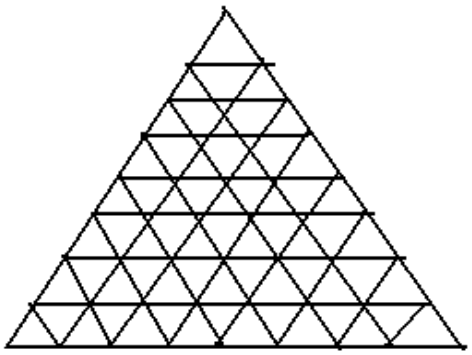

Figure.3: Zoom of the area near to the reference Space vector diagram of 9-level inverter in Sextant-I

3. Representation of Proposed DTC Scheme

The basic requirements of DTC strategy is the estimation of the stator flux and electromagnetic torque. The flux evaluation can be carried out by different techniques depending on the whether the rotor angular speed or position which are measured or observed. For multilevel applications, the voltage model is usually employed. The stator flux can be evaluated by integrating from the stator voltage equation

$$\phi_s = \int (U_s - R_s i_s)\Delta t \qquad (1)$$

Further to calculation of the components of the flux, the estimated torque is determined from the following equation (2)

$$\Gamma_e = \rho(i_{\beta s}\Phi_{ds} - i_{\alpha s}\Phi_{qs}) \qquad (2)$$

As shown on figure, DTC scheme needs only the output voltages and currents of the inverter which feeds the induction motor, the instantaneous values of flux and torque in the machine are then calculated and the error can be gotten after compared with the referring torque and flux (T_{eref} and ψ_{sref})

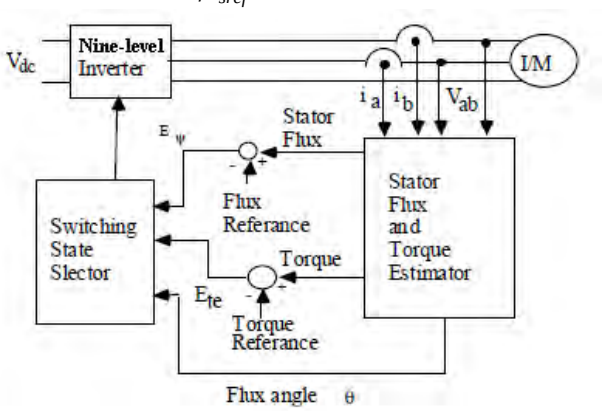

Figure.4: Configuration of proposed DTC Scheme

The flux control is made by two-level hysteresis comparator and C_Φ defines the action wished on the behaviour of the field. Also, a high level performance torque is required and the torque control is controlled by a hysteresis comparator built with eight lower bounds and eight upper know bounds and C_Γ defines the action wished on the behaviour of the torque [9]. The hysteresis blocks are designed as it is shown in figure 5.

For the switching vector selection, it is necessary to know the angular sector in which the actual flux is located. The actual position of the stator flux can be determined by equation (3), from the orthogonal flux components:

$$\theta = \tan^{-1}\left(\frac{\Phi_{\beta s}}{\Phi_{\alpha s}}\right) \qquad (3)$$

The flux position in the α and β Planes is quantified in six sectors S of 60^0 degrees staring with the first sector situated between -30^0 and 30^0.

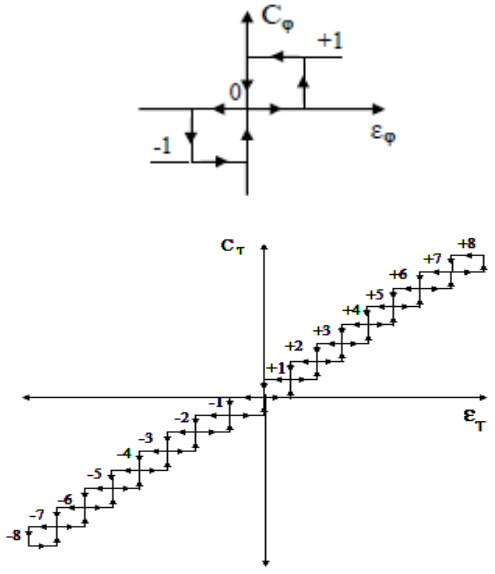

Figure.5: Flux and Torque Hysteresis blocks

TABLE VI

Proposed Switching Table

		S											
C_{Φ}	C_{f}	1	2	3	4	5	6	7	8	9	10	11	12
	-8	684	694	685	696	680	686	681	688	682	690	683	692
	-7	594	604	595	606	590	596	591	598	592	600	593	602
	-6	494	504	495	506	490	496	491	498	492	500	493	502
	-5	254	264	255	266	250	256	251	258	252	260	253	262
	-4	184	194	185	196	180	186	181	188	182	190	183	192
	-3	127	143	128	145	123	135	124	137	125	139	126	141
	-2	307	399	308	400	303	395	304	396	315	397	306	398
	-1	5	48	6	49	1	44	2	45	3	46	4	47
	0	Zero Vector											
	+1	3	46	4	47	5	48	6	49	1	44	2	45
	+2	305	397	306	398	307	399	308	400	303	395	304	396
+1	+3	125	139	126	141	127	143	128	145	123	135	124	137
	+4	182	190	183	192	184	194	185	196	180	186	181	188
	+5	252	260	253	262	254	264	255	266	250	256	251	258
	+6	490	498	491	500	492	502	493	504	488	494	489	496
	7	590	598	591	600	592	602	593	604	588	594	589	596
	8	678	686	679	688	680	690	681	692	676	682	677	684
	-8	696	680	686	681	688	682	690	683	692	684	694	685
	-7	590	596	591	598	592	600	593	602	594	604	595	606
	-6	496	491	498	492	500	493	502	494	504	495	506	490
	-5	251	258	252	260	253	262	254	264	255	266	250	256
	-4	188	182	190	183	192	184	194	185	196	180	186	181
	-3	125	139	126	141	127	143	128	145	123	135	124	137
	-2	397	306	398	307	399	308	400	303	395	304	396	315
	-1	4	47	5	48	6	49	1	44	2	45	3	46
	0	Zero Vector											
	+1	45	3	46	4	47	5	48	6	49	1	44	2
	+2	397	306	398	307	399	308	400	303	395	304	396	305
-1	+3	139	126	141	127	143	128	145	123	135	124	137	125
	+4	183	192	184	194	185	196	180	186	181	188	182	190
	+5	262	254	264	255	266	250	256	251	258	252	260	253
	+6	492	502	493	504	488	494	489	496	490	498	491	500
	+7	602	593	604	588	594	589	596	590	598	591	600	592
	+8	681	692	676	682	677	684	678	686	679	688	680	690
	-8	692	684	694	685	696	680	686	681	688	682	690	683
	-7	604	595	606	590	596	591	598	592	600	593	602	594
	-6	506	490	496	491	498	492	500	493	502	494	504	495
	-5	256	251	258	252	260	253	262	254	264	255	266	250
	-4	188	182	190	183	192	184	194	185	196	180	186	181
	-3	139	126	141	127	143	128	145	123	135	124	137	125
	-2	398	307	399	308	400	303	395	304	396	315	397	306
	-1	48	6	49	1	44	2	45	3	46	4	47	5
	0	Zero Vector											
	+1	47	5	48	6	49	1	44	2	45	3	46	4
	+2	308	400	303	395	304	396	305	397	306	398	307	399
0	+3	145	123	135	124	137	125	139	126	141	127	143	128
	+4	186	181	188	182	190	183	192	184	194	185	196	180
	+5	258	252	260	253	262	254	264	255	266	250	256	251
	+6	498	491	500	492	502	493	504	488	494	489	496	490
	+7	600	592	602	593	604	588	594	589	596	590	598	591
	+8	690	681	692	676	682	677	684	678	686	679	688	680

Using the hysteresis comparator outputs flux C_Φ and torque C_T and the stator flux sector S, the proper output vector can be chosen to correct the error due to the relation in the switching table. The switching configuration is made step by step. The selection of a voltage vector at each cycle period Te is carried in order to maintain the flux and torque within the limits of two hysteresis bands. Several switching tables for three-level inverter are presented in [10].

A new switching table for the 9-level inverter selector has been developed in Table III, to achieve an accurate control. In order to simplify, the mechanical rotor speed will be considered when assigning the voltage vectors needed at each one of those sectors. The speed of the stator flux linkage vector is given by the modulus of the applied voltage vector. Thus, the voltage vectors will be chosen according to the rotor speed [11]. Voltage vectors with low amplitude will be chosen for lower speeds.

4. Simulation Results and Discussion

The proposed scheme is simulated in DTC with multilevel control. The induction motor parameters are as follows: Rs=4.85Ω, Rr=3.805Ω, Ls=274mH, Lr=274mH, Lm=258mH, p=2, J=31g.m2, V=220V, power=1.5kW and speed=1420rpm. All simulations have a sample time for the control loop of 100μs; the voltage of the DC bus is 514V. The requested space voltage vector, demanded by the DTC strategy, is assured as shown by the line voltage in Figure.13 Thus, if compared with a seven-level DTC strategy [9]; the dv/dt applied to the motor terminals is greatly reduced. Furthermore, the electromagnetic torque is also improved. It is possible to reduce pulsation amplitude by approximately a factor of 2 when compared to a seven - level DTC strategy.

To show the effectiveness of the DTC with 7-level and 9-level inverters with SVPWM switching technique a simulation work has been carried out on induction motor.

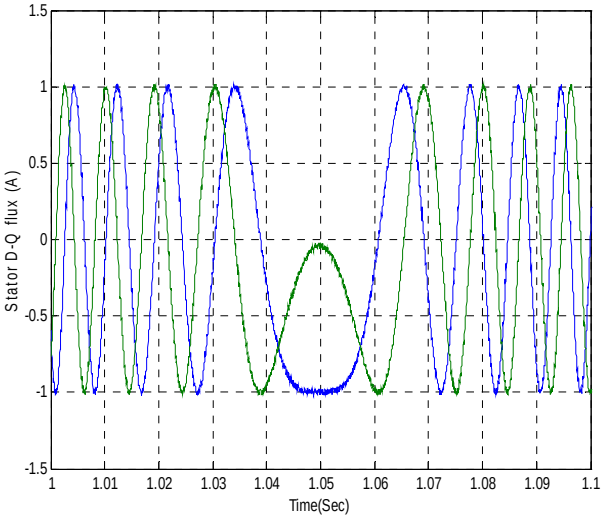

Figure.6: D-Q axis flux response of 7-level Inverter fed DTC IM drive

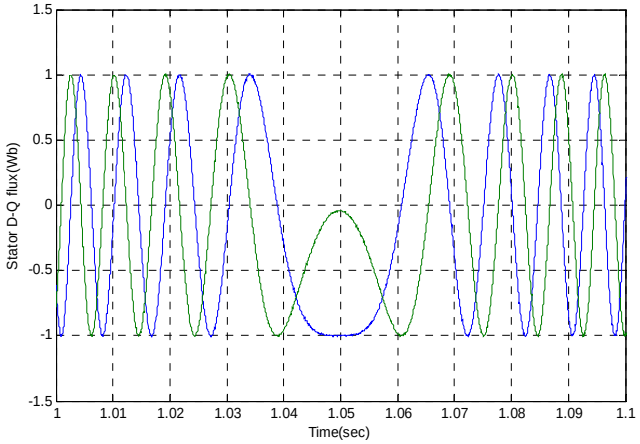

Figure.7: D-Q axis flux response of 9-level Inverter fed DTC IM drive.

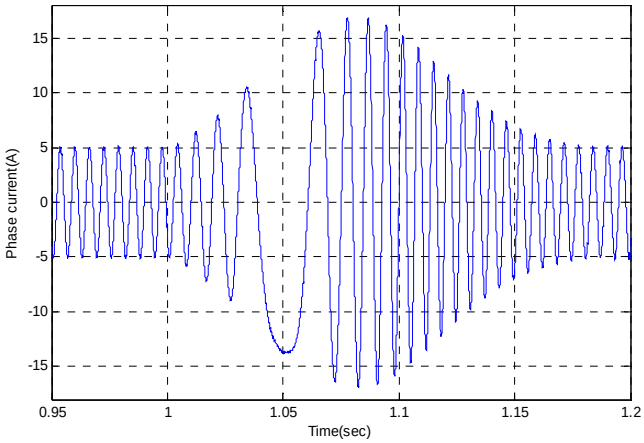

Figure.8: Phase current response of 7-level Inverter fed DTC IM drive .

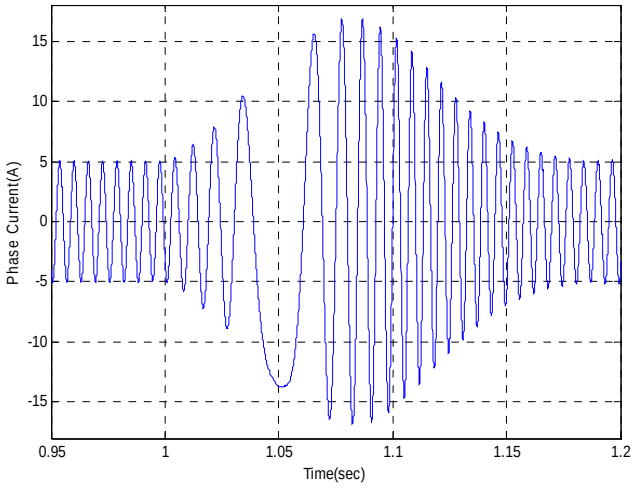

Figure.9: Phase current response of 9-level Inverter fed DTC IM drive

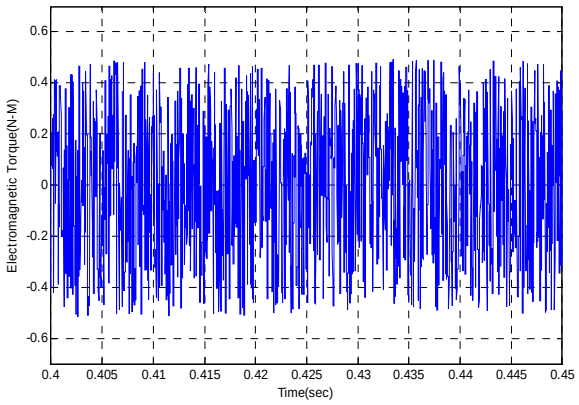

Figure.10: Torque error for 7-level inverter fed DTC IM drive

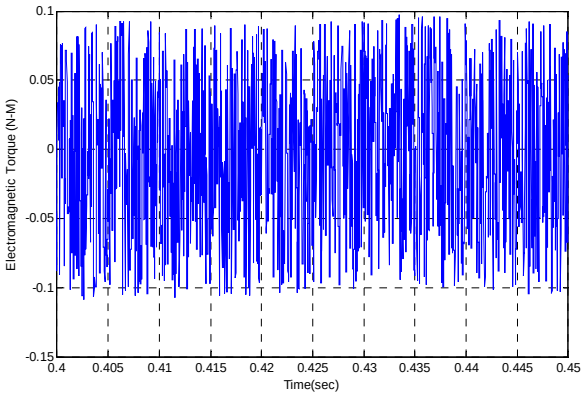

Figure.11: Torque error for 9-level inverter fed DTC IM drive

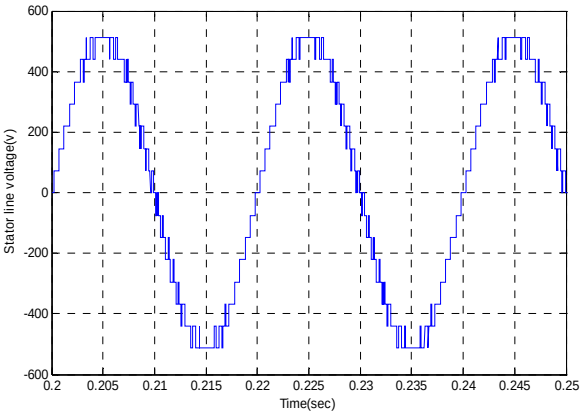

Figure.12: Stator line voltage of 7-level inverter

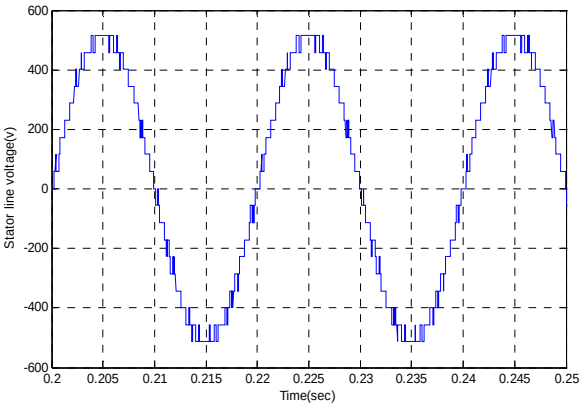

Figure.13: Stator line voltage of 9-level inverter

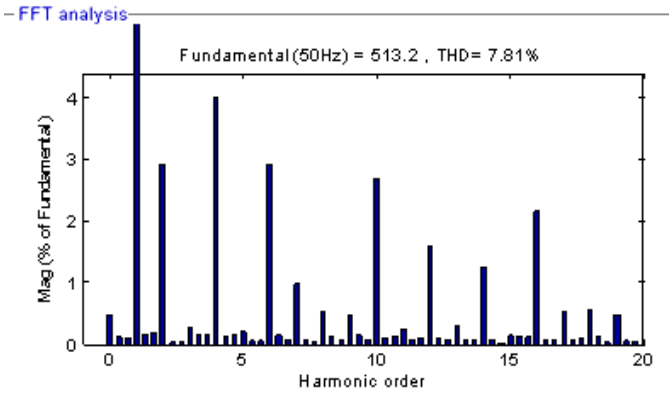

Figure.14:Stator line voltage harmonic spectrum of 9-level inverter

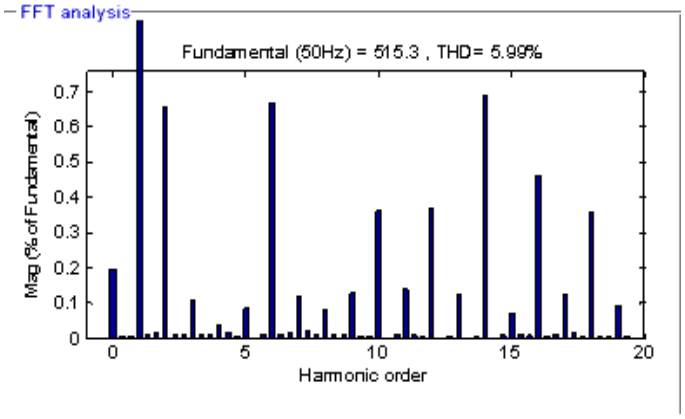

Figure.15: Stator line voltage harmonic spectrum of 9-level inverter

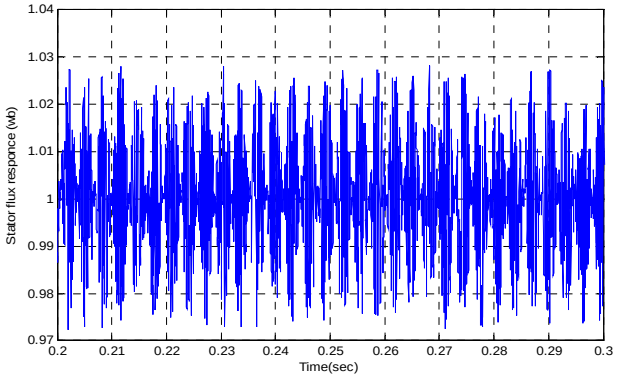

Figure.16:Stator flux error of 7-level Inverter fed DTC IM drive

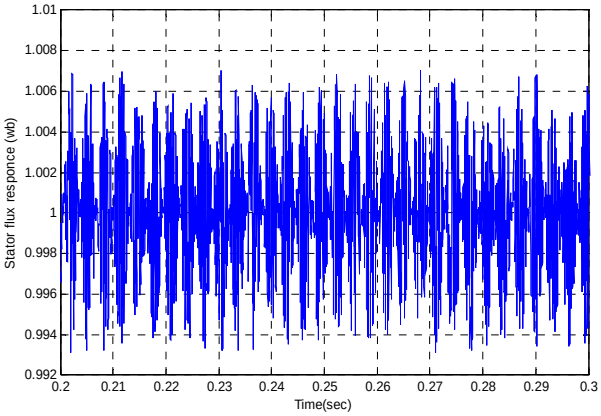

Figure.17: Stator flux error of 9-level Inverter fed DTC IM drive

In figure 6 and 7 D-Q axis flux response of the 7 and 9 - level inverters are compared. It is seen that the performance of the 9-level inverter fed DTC IM drive has lower ripple, so the proposed system is superior to control the flux with reduced ripple content. Figure 8 and 9 illustrate the phase current performance of 7-level and proposed inverter system, ,the phase current response 9-level inverter is fast recovery is obtained .Figure 10 and 11 shows the torque errors of the two systems, from the simulation results 7-level inverter torque error is 0.5 N-M and 9-level inverter fed DTC IM drive torque error is reduced to 0.09 N-M, so from the proposed system torque ripple minimization is possible. The stator line to line voltages of 7-level and 9-level inverter system are illustrated in Figure 12 and 13.

Figures 14, 15 shows the Stator line voltage harmonic spectrum of 7 and 9-level inverter system. The 7-level inverter THD is 7.81% and proposed system THD is reduced to the 5.99%. From the analysis 9-level inverter has reduced THD; it indicates that dv/dt applied to the motor terminals is greatly reduced. Furthermore, the electromagnetic torque is also improved. Figure 16 and 17 shows the stator flux errors response of the two systems (7 and 9-level inverters).

From the above discussion, the proposed DTC IM drive system behavior is good, even in extreme conditions like the reverse speed reference with nominal load torque applied. Reduction in ripple is observed in both electromagnetic torque and flux is due to the use of hysteresis controllers.

5. Conclusions

A nine–level inverter system for DTC induction motor drive is presented. DTC strategy of a nine–level Multi Point Clamped (MPC) voltage source inverter fed induction motor is implemented using Matlab/Simulink .

Nine-level inverter has 729 switching states and there are 106 effective vectors are possible. The proposed DTC IM drive scheme is capable for enough degrees of freedom to control both electromagnetic torque and stator flux with very low ripple.

The following points are most attractive features of multilevel inverter fed DTC IM drive.

- The output voltages with extremely low distortion and lower dv/dt .
- They can operate with a lower switching frequency.
- As the number of levels increased the %THD in the motor phase voltage decreased,.
- The number of level increased the torque ripple is reduced to minimum and the stator flux ripple is also minimized.
- For the proposed system has stator flux trajectory response is a circle and answer the response is faster as compared to the 7-level inverter.

Nomenclature

ϕ_S = Stator flux linkage

U_S = Stator voltage expressed in the stator reference frame

R_S = Stator resistance

I_S = Stator current

Δt = Standard deviation

Γ_e = Instantaneous value of the electromagnetic torque

ρ = Derivation operator

$i_{\beta s}$ = Imaginary component of stator current

$i_{\alpha s}$ = Real component of stator current

Φ_{ds} = D-axis stator flux linkages

Φ_{qs} = Q- axis stator flux linkages

T_{ref} = Torque reference

Ψ_{sref} = stator flux reference

6. References

[1] M. F. Escalante, J-C. Vannier and A. Arzandé.Flying Capacitor Multilevel Inverters and DTC Motor Drive Applications. IEEE Trans. On Industrial Electronics, vol. 49, (No.4), pp. 809-815, 2002.

[2] J. Rodriquez, J-S Lai and F. Z. Peng.Multilevel Inverters: A survey of topologies, controls, and applications.IEEE Trans. On Industrial Electronics, vol. 49, (No.4), 2002.

[3] I. Takahashi and T. Nogushi. A new quick-response and high efficiency control strategy of induction motor. IEEE Trans. On. IA, vol. 22, (No.5), pp. 820-827, 1986.

[4] G. Buja, D. Casadei and G. Serra. Direct torque control of induction motor drives. Proc. IEEE International Symposium on Industrial Electronics, vol. 1, pp.TU2-TU8, 1997.

[5]P. Vas, Sensor less Vector and Direct Torque Control. Oxford, U.K.: Oxford Univ. Press, 1998.

[6]D.Casadei, G.Grandi, G. Serra and A. Tani, Switching strategies in direct torque control of induction machines, ICEM 94, Vol. 2, pp. 204-209, 1994.

[7] I. Messaïf, E.M. Berkouk, N. Saadia and A. Talha, Application of Direct Torque Control Scheme for Induction Motor, International AMSE Conference MS'05, 2005.

[8]I.Messaïf, E.M. Berkouk, N. Saadia, Ripple Reduction in DTC Drives by Using a Three-Level NPC VSI, 14th IEEE International Conference on Electronics, Circuits and Systems, Morocco, ICECS2007.

[9]I. Messaïf, E.M. Berkouk, N. Saadia, An Improved DTC strategy for induction machine control fed by a multilevel voltage source inverter, IEEE International Conference on Electronics, Circuits and Systems, Morocco.

[10]B.P. McGrath,D.G. Holmes and T.A. Lipo,Optimised Space Vector Switching Sequences for Multilevel Inverters , IEEE Transactions on Power Electronics, Vol.18 Issue:6,pp 1293 – 1301,2003.

[11]O.ChandraSekhar and K.ChandraSekhar, Space vector modulation & fuzzy PID speed controller for direct torque control induction motor drive. Journal of

Theoretical and Applied Information Technology**.** Vol.35 no.2,pp 126 – 134, 2012.

[12]T.BrahmanandaReddy,K.Sri Gowri and Ch.Sai Babu,GDPWM Algorithm for Direct Torque Controlled Induction Motor Drive Using the Concept of Imaginary Switching Times Automatic Control and System Engineering ACSE",vol.8,no.3,pages37—44,2008.

[13]N.R. Reddy,T.BrahmanandaReddy, J. Amarnath, and D. Subba Rayudu ,Minimum Switching Loss PWM Algorithms for Three-Phase Voltage Source Inverter Fed Induction Motor Drives, Automatic Control and System Engineering ACSE,vol.10,no.1,pages39-48,2010.

Biographies

Mr.O.Chandrasekhar received his B.Tech degree in Electrical & Electronics Engineering from JNTUH,India in 2005 and M.Tech with power Electronics and Electrical Drives from Vignan's Engineering College,Vadlamudi, India in 2008.He has been with Vignan's Lara Institute of Technology and Science ,Vadlamudi as Associate Professor. Presently he is a part-time research student at J.N.T.U College of Engineering, Hyderabad-500072, India, working towards his doctoral degree. His Research interests are Power Electronics, Industrial Drives.

Dr.K.ChandraSekhar received his B.Tech degree in Electrical & Electronics Engineering from V.R.Siddartha Engineering College, Vijayawada, India in 1991 and M.Tech with Electrical Machines & Industrial Drives from Regional Engineering College, Warangal, India in 1994. He Received the PhD degree from the J.N.T.U College of Engineering, Hyderabad, India in 2008. He is having 17 years of teaching experience. He is currently Professor and Head of Department, EEE, R.V.R & J.C.College of engineering, Guntur, India. His Research interests are Power Electronics, Industrial Drives & FACTS Devices.

www.icgst.com

Hybrid MPPT-Controlled LED Illumination Systems

Akram Abu-aisheh[1] and Sameer Khader[2]
[1]University of Hartford, West Harford, Connecticut, USA
[2]Palestine Polytechnic University, Hebron, Palestine

Abstract
This paper presents a road map for the design and development of sustainable hybrid High Brightness Light Emitting Diode (HB LED) illumination systems with maximum power point tracking (MPPT). The proposed hybrid system design presents the foundation for future sustainable high efficiency illumination systems. The system design presented in this paper individually controls an array of HB LEDs. Each HB LED operates in a different mode defined by the user. Photovoltaic (PV) panels-based systems are used as the primary source of energy in this system while the electric grid is used as the backup source that supplies power to the HB LEDs only when the power of the PV system is not sufficient to supply all the system HB LEDs and the PV system batteries are depleted below the minimum level set in the system design. A matlab/ Simulink model is proposed for studying the system behaviors and operation modes.

Keywords: *MPPT, High Brightness LED; Hybrid; Matlab/ Simulink; DC Chopper*

1. Introduction
The demands for utilizing alternative power sources have increased due to rising oil prices and more stringent environmental regulations. Alternative energy and its applications have been heavily studied for the last decade, and solar energy is the preferred choice in many applications [1]. Among solar energy applications, the photovoltaic (PV) technology has received much attention, and it is being used in many applications [2&3].
This paper presents a sustainable hybrid high brightness LED Illumination System that can be used to replace current illumination systems in order to improve the system efficiency and reliability. In the proposed system, a Single-ended primary-inductor converter (SEPIC) DC-DC converter is used to deliver solar energy via PV cell modules to a battery bank in charging mode during the daytime. At night, it drives an LED lighting system.
The main reason for choosing HB LEDs as the illumination source in this system is due to their high efficiency as compared with incandescent and fluorescent lamps. A second factor is that the world of DC Application is fast expanding with the requirements of data storage and high efficiency requirements in supply distributions. Compact fluorescent lamps are becoming obsolete, and replaced with HB LED lamps driving the efficiency of lighting systems. The system presented in this paper expands on the continued growth of DC power distribution in buildings, and driving this trend toward that end LED-based lighting has been cited as a factor.

2. Hybrid LED Illumination
The principal motivation for this hybrid system is the clear shift to DC systems with more use of alternative energy sources. The AC vs. DC battle raged when Edison promoted DC power while George Westinghouse felt that AC was the way to go. As we know, AC won the battle, since it was so much easier to step the voltage up and down using transformers, and higher voltages greatly reduce resistive loss. This paper explores the continued growth of DC power, and the force driving the trend; LED-based lighting has been cited as one major driver.
Since photovoltaic panels are used to power the illumination system, there is a need for a second source of power for the system when the sun is out for a period of time beyond the capability of the batteries to serve as a backup source. Some products that are appearing in the market use HB LED with build-in converter that can be connected directly to the AC line. These products take advantage of the high efficiency of HB LEDs, but they do not use a sustainable source as the main supply for those LEDs. The authors present this new hybrid HB LED-based illumination system design with automatic transfer switch as given in figure 1. This hybrid system uses solar as the primary source of energy, and it switches to the AC line only when the primary source can't supply the required power to the system.
In the system given in figure 1, LEDs are powered from the solar panel during the daytime as the primary source, with the battery in charge mode, and they operate from the battery at night. If the battery is fully discharged, the HB LED System operates from the AC line as the secondary source. The design of DC-DC converters, DC-AC rectifiers, and DC-AC inverters are well understood and can be followed using senior level or graduate power electronics textbooks [4-8]

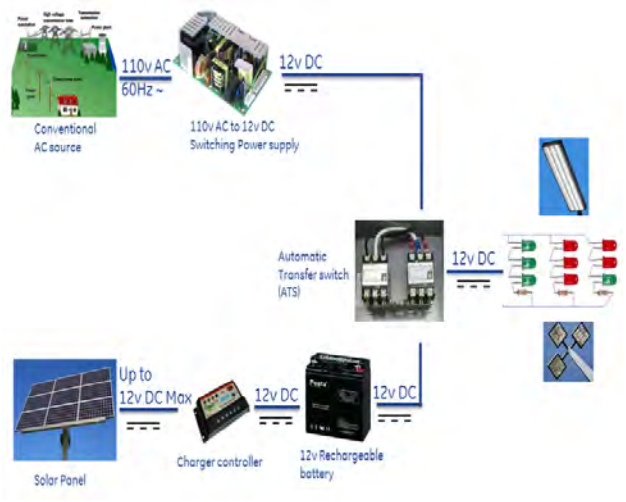

Figure 1: Hybrid High Brightness LED Illumination System

Since LEDs can handle voltage fluctuations, the system can be simplified by using a full wave bridge rectifier instead of the AC-DC converter. The simplified system is given in figure 2 where components can be classified into two different categories. The first one is high tension parts which consist of photo cells and high power LED, and the other is the low tension side which consists of L, C, and battery. The operation of this buck-boost converter has two operation modes: the first is the buck mode for day time battery charging operation, and the second is the boost mode for evening time lighting usage.

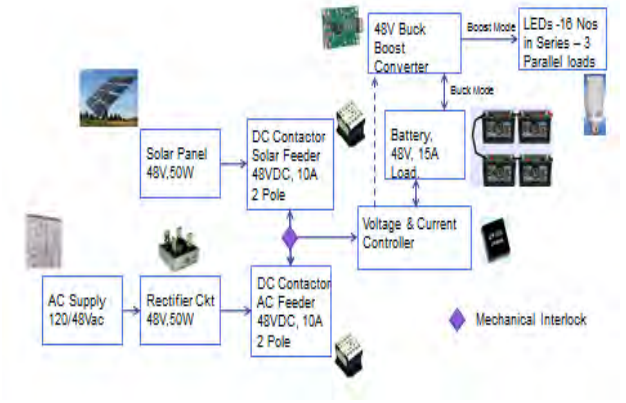

Figure 2: Simplified Hybrid Illumination

This simplified system is sustainable for many applications emerging due to the continued growth of DC power distribution in buildings, and the principal force behind this trend is LED-based lighting which we have cited as one major driver. The main challenges in building such a system include analysis of a switching circuit that controls alternating of power between the AC and DC distribution systems, being fed from Solar panel and switching between the two sources. Figure 3 presents one solution for this problem where an AC contactor and a DC contactor with mechanical interlock are used, and figure 4 presents the relay control for the mechanically interlocked contactors.

The illumination system is designed to be used to individually control an array of HB LEDs. Each HB LED operates in a different mode that is independently defined by the user. The defined sequence of LED illumination is operated by means of a controller circuit, i.e. an FPGA. Figure 5 presents the basic control system layout used for this DC illumination control strategy that gives the user more flexibility and control than the flexibility and control level available for standard AC powered illumination used in incandescent or fluorescent lamps.

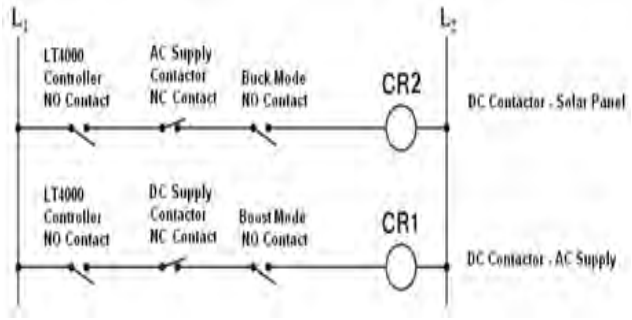

Figure 3: AC and DC Contactors Design to Control the LED Illumination System Switching

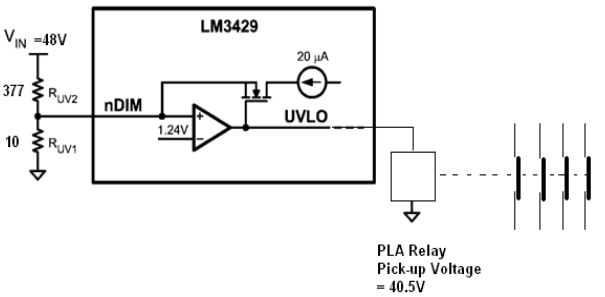

Figure 4: Relay Design used to Control the Hybrid Illumination Switching

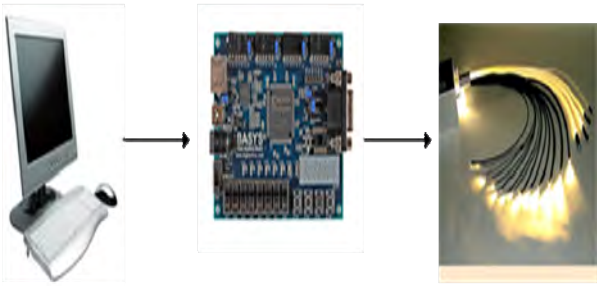

Figure 5: FPGA-Controlled Illumination

The FPGA is programmed using Hardware Description Language (HDL). In this case VHDL is used. [VHDL is a hardware description language used in electronic design automation to describe digital and mixed systems and integrated circuits.] The pattern of the LEDs defined by the user can be modified using this hardware language. Basys Spartan 2 FPGA is used for this application due to its flexibility, low cost, and ease of use.

The application software used in our case is Adept which is a powerful program that allows configuration and data transfer with Xilinx logic devices, and is used as an interface between Xilinx and the Spartan 2 FPGA. For maximum intensity from the LEDs, the typical forward voltage of 3.9V, with forward current 700mA, is supplied to the FPGA. A personal computer provided with Xilinx software environment is used for programming the sequence of the LEDs defined by the user. The programming is done again using VHDL. The developed software was tested using Digilent FPGA.

High brightness LEDs [9&10] can be driven at currents from hundreds of mA to more than an ampere, compared with the tens of mA for other LEDs; however few of the HB LEDs can produce over a thousand lumens. Since overheating is destructive, the HP LEDs may need to be mounted on a heat sink to allow for heat dissipation. If the heat from an HB LED is not removed using a heat sink, the device will burn out in seconds.

A single HB LED can often replace an incandescent bulb in a torch, or be set in an array to form a powerful HB LED system. LEDs can operate on AC power without the need for a DC converter. Each half-cycle part of the LED emits light with the other half cycle being dark, and this is reversed during the next half cycle. The efficacy of this type of HB LED is typically around 40 LM/W. A large number of LED elements in series may be able to operate directly from line voltage. In 2009 Seoul Semiconductor released a high DC voltage capable of being driven from AC power with a simple controlling circuit. The low power dissipation of these LEDs gives them more flexibility than the original AC LED design. In this project the HB LEDs are powered from a DC source.

To control the LED from the FPGA, a driver circuit is needed to boost the power of the FPGA output. An LED driver circuit is an electric circuit used to power a light-emitting diode or LED. The circuit consists of a voltage source powering a current limiting resistor and an LED connected in series. The HB LEDs used in our design have a constant current of 700mA and a supply voltage of +3V. As the current has to be amplified to 700mA for each LED, two transistors are connected together so that the current amplified by the first is amplified further by the second transistor. The overall current gain is equal to the two individual gains multiplied together, i.e $h_{FE} = h_{FE1} \times h_{FE2,}$ where h_{FE1} and h_{FE2} are the gains of the individual transistors.

3. Sustainable PV-Powered Illumination

Since photovoltaic panels are used to power the HB LED illumination systems, there is a need for the development of the DC converter system to power the LEDs. To satisfy this requirement, a forward converter with PV-based LED applied in lighting systems was used. In the proposed DC supply system, the SEPIC is used to deliver solar energy via PV cell modules to a battery bank in charging mode during the daytime. During the nighttime, the converter drives an LED lighting system.

Figure 7 illustrates the principle PV-SEPIC- LED circuit applied in street illumination, where the produced PV voltage is stored in a battery bank throughout the charging unit during the daytime, at night the discharger activates and the LEDs are energized with appropriate voltage throughout the step-up transformer and full bridge rectifier.

SEPIC circuits find widespread application when the input voltage fluctuates above and below average value, while the output voltage must be kept at a constant value with minimum tolerances. One of most important applications of SEPIC circuit is the integration with the photovoltaic system (PV system) and illumination load of series and parallel connected LEDs.

The SEPIC converter is a DC/DC converter topology that provides a positive regulated output voltage from an input voltage that varies from above to below the output voltage. This type of topology is needed when the voltage from an unregulated input power source such as solar where the sun irradiation, temperature and weather changes directly affect the generated output voltage. The standard SEPIC topology [11&12] requires two inductors in additional to step-up transformer, making the power-supply footprint quite large.

Photovoltaic (PV) cells are used to convert the sunlight into electrical energy. On the other hand, it is also an important issue to save the energy demand and increase the energy efficiency [13-15]. High brightness light emitting diodes (LEDs) [16&17] are becoming more widespread for the lighting applications such as automobile safety and signal lights, traffic signals, street lighting and so on. LED power circuitry is discussed thoroughly in the literature [18].

In lighting applications with solar energy, the charger is adapted to convert the solar irradiations for storing in the battery during the daytime. In the nighttime, a discharger is used to release energy in the battery and drive the LED lighting system. Low-power DC-DC converters can be used for the charger and discharger mode. Since the PV voltage from the solar panel is unstable, the buck-boost converter is more suitable for the charger circuit. This converter can also be used in the discharger circuit.

4. DC-DC Converter MPPT Control Design and Analysis Using Computer Simulation

Computer simulation is an important tool for future illumination systems design. The HB LED-based illumination system was simulated using a matlab/Simulink environment [19]. In this section, we present the complete simulation model including the solar PV module, Maximum Power Tracking module (MPPT), DC-DC boost converter and storage unit (Battery). These modules are going to be described as follows:

4.1 Characteristics of PV Array

Basically, PV cell is a P-N semiconductor junction that directly converts light energy into electricity. It has the equivalent circuit shown in Figure1 as represented in [20-22].

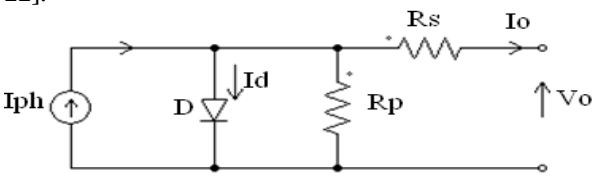

Figure 6: Equivalent circuit for PV cell

Where I_{ph} represents the cell photocurrent; R_p and R_s are the intrinsic shunt and series resistance of the cell respectively; Id is the diode saturation current; V_o and I_o are the cell output voltage and current respectively.

The following are the simplified equations describing the cell output voltage and current:

$$V_o = \frac{A.K.T_c}{q} \ln\left(\frac{I_{ph} + I_d - I_o}{I_o}\right) - R_s.I_o \qquad (1)$$

$$I_o = N_p\left(I_{ph} - I_d\left(e^{\frac{q.Vo/Ns}{A.K.Tc}} - 1\right)\right) \quad (2)$$

$$I_d = I_{or}\left(\frac{T_c}{T_r}\right)^3 . e^{\frac{q.Eg}{B.K}\left(\frac{1}{Tr} - \frac{1}{Tc}\right)} \quad (3)$$

$$I_{ph} = N_p.\{I_{sc}.\phi_n + I_t(T_c - T_r)\} \quad (4)$$

Where, K- Boltzmann constant; N_p and Ns are the number of parallel and series connected cells respectively; E_g is the band gap of the semiconductor; T_c and T_r are the cell and the reference temperature respectively in Kelvin, A and B are the diode ideality factors with values varies between 1 and 2; Φ_n is the normalized insulation; I_{sc} is the short circuit current given at standard condition; I_t and I_{or} are constants given at standard conditions.

4.1 Photovoltaic I-V Performance

In order to study the I-V performance of the PV circuit and to look for appropriate dc chopper for boosting up the output voltage to predetermined value it is necessary to illustrate the obtained PV voltage and current for boost chopper according to specifications given in table 1 at reference irradiation 1000W/m2.

The PV Array voltage can be obtained by multiplying the module voltage and current by N_{sm} and N_{pm} that represents number of series and parallel connected modules respectively.

Table 1: Data specification for PV Array.

q	K	I_{ph}	I_d	R_S	R_P	T_C
1.602e-19 C	1.38e-23J/°K	4 A	0.2mA	23mΩ	0.65kΩ	25°C
N_S	N_P	V_O	V_{OC}	I_{SC}	V_{MPP}	I_{MPP}
38	4	0.6V	21.5 V	4.7A	17.5V	3.7A
N_{Sm}	N_{Pm}	R_{load}				
1	1	4.5Ω(Set of Series connected LED Diodes)				

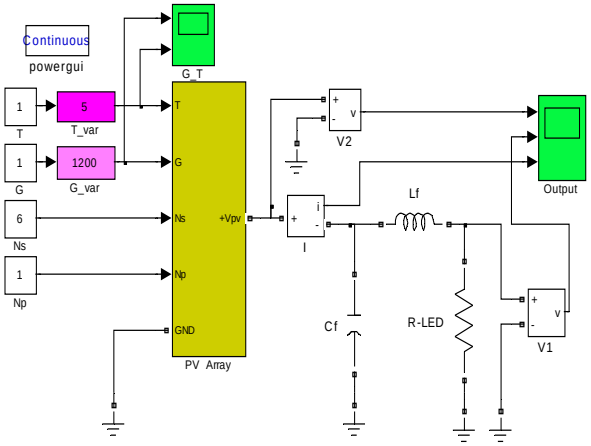

a) Matlab/Simulink module for PV Array

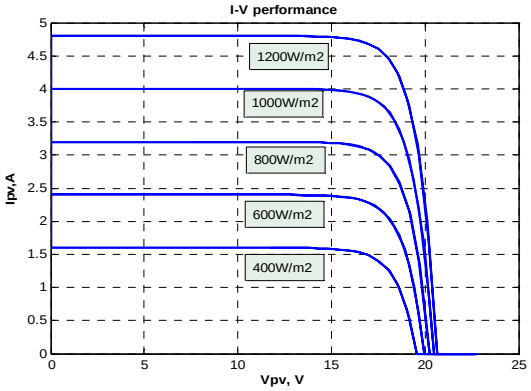

b) I-V Performance of PV module.

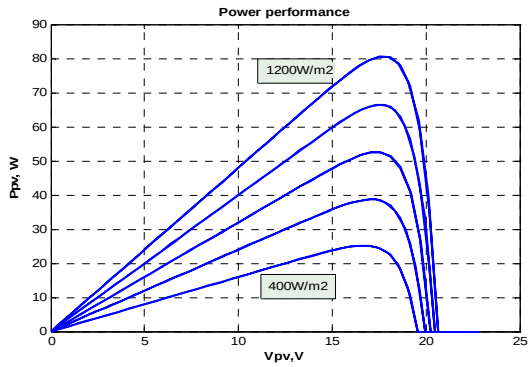

c) Power performance of proposed module

Figure 7: PV Array module & main charaterestics.

Figure 7 illustrates the proposed PV array with R load presenting the equivalent resistance of complete LED set, where the obtained results for different variation levels are presented. From these performances it is shown that the total output PV voltage and current varies according to irradiation level with approximated 65W maximum power at G=1000W/m2.

4.2 Maximum power point derivation

In order to operate the module at maximum extracted power, it is necessary to calculate the coordinates of the maximum power point (V_{MPP}, I_{MPP}). For this, and to simplify the model in Simulink, the coordinates of the maximum power point are given by the following equations:

$$I_{MPP} = I_{ph} - I_d.\left(e^{V_{mpp}/V_T} - 1\right) \quad (5)$$

$$V_{MPP} = V_T.\ln\left(1 + \frac{I_{ph} - I_{m\,pp}}{I_{ph}}\left(e^{V_{OC}/V_T} - 1\right)\right) \quad (6)$$

Where V_T and Voc are the thermal voltage and the cell open circuit voltage respectively and given by:

$$V_T = \frac{K.T_c}{q}$$

$$V_{OC} = V_T.\ln\left(\frac{I_{sc}}{I_d} + 1\right) \quad (7)$$

The maximum power that can be obtained can be expressed as follows:

$$P_{MPP} = V_{MPP}.I_{MPP} \quad (9)$$

Obtaining ng the maximum obtained power form the PV for given solar irradiation requires controlling the duty cycle D of DC Buck-Boost Chopper toward operating the chopper in mode where the extracted from the system power will be maximum. There are several approaches used for realizing MPPT operation mode, one of the most popular and simple approach de is called Perturbation & Observation model (P&O MPPT model).

The mathematical equations realized MPPT approach are expressed as follows:

$$
\begin{aligned}
&Vo = Vpv.\frac{1}{1-D}\\
&Po = Vo^2 / RI\\
&dPo = Po(k+1) - Po(k);\\
&dVo = Vo(k+1) - Vo(k);\\
&(dPo/dVo) = ?..... \rightarrow D = ?
\end{aligned}
\qquad (10)
$$

$$
dPo\begin{cases}
> 0 \rightarrow dVo\begin{cases} > 0 \rightarrow D = D - \Delta D \\ < 0 \rightarrow D = D + \Delta D \end{cases}\\
< 0 \rightarrow dVo\begin{cases} > 0 \rightarrow D = D + \Delta D \\ < 0 \rightarrow D = D - \Delta D \end{cases}
\end{cases}
$$

While figure8 illustrates the Power performance and the flowchart procedure for obtaining the appropriate duty cycle needed to operate the chopper at maximum obtained power.

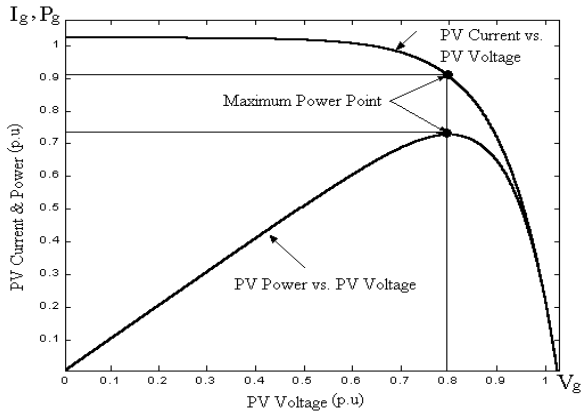

a) Maximum Power Point Tracking procedure

The proposed mathematical equations and corresponds flowchart can be summarized with operation logic as follow:

- (dPo/dVo)<0 ➔ operation at the right hand side of the curve (fig.8a), for D➔ Dmin , then V must be decreased (moving toward decrease).
- (dPo/dVo>0) ➔ operation at the left hand side of the same curve , for D➔ Dmax≈1). Then V must be increased (moving toward increase).

4.3: Boost DC Chopper

The output PV voltage in most of applications is requred to be boost up by applying Boost DC chopper [6]as shown in figure 9, where the principle electrical circuit and the operation mode at continuous current mode (CCM) are illustrated.

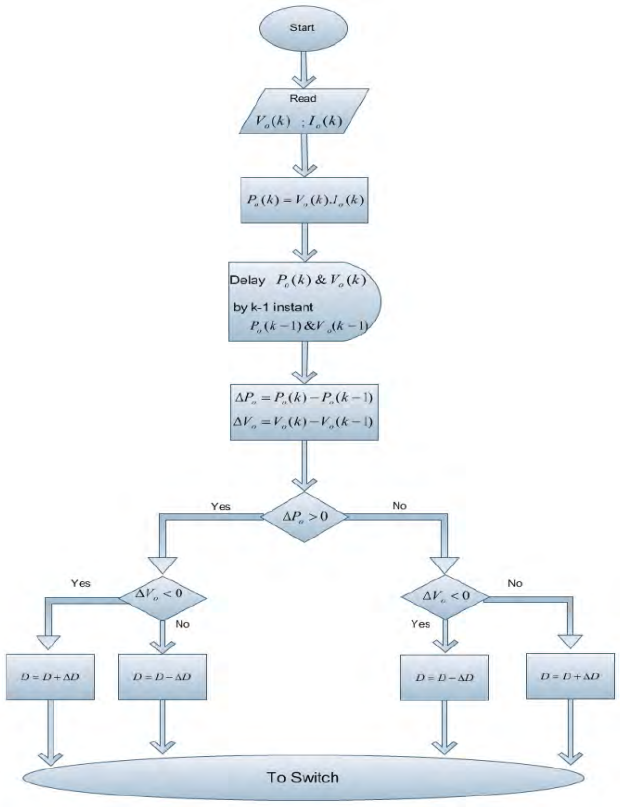

b) Flowchart for tracking procedure

Figure 8: P&O MPPT tracking method.

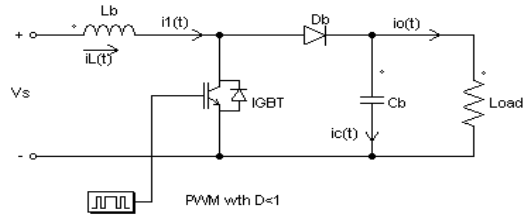

a) Boost DC Chopper

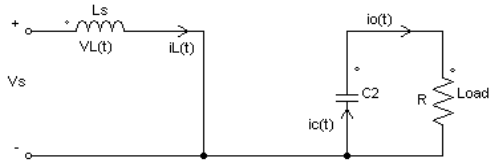

b) Mode#1: IGBT=ON

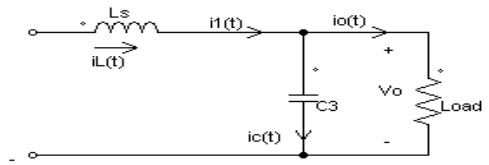

c) Mode#2: IGBT=OFF

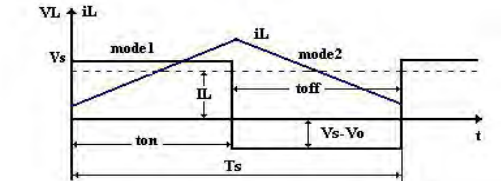

d) Load voltage & current at two operation modes

Figure 9: Equivalent circuit for boost converter operating in CCM

4.4: Matlab Simulation of Proposed Model

The complete electrical circuit for LED illumination system is simulated in mat lab/simulink environment and illustrated in 10

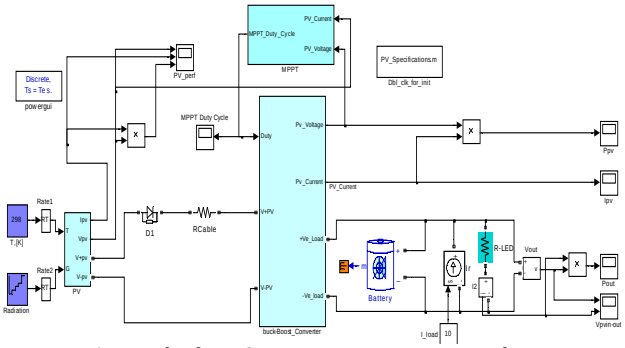

a) Load voltage & current at two operation modes

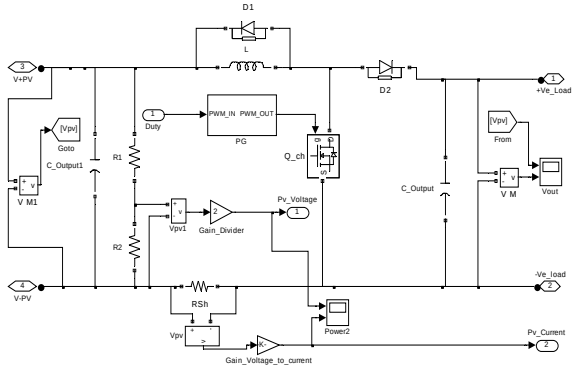

b) DC Chopper simulation module

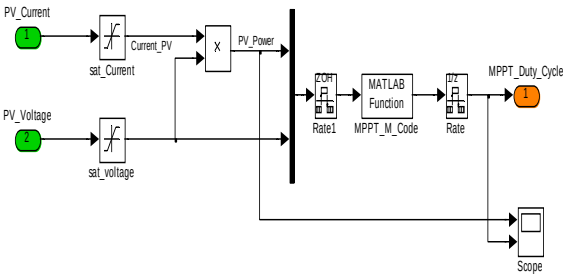

c) MPPT module

Fig.10: Complete Simulation model of PV- LED illumination system.

4.5: Simulation Results

There are various PV and chopper paramtetrs that can be described; some of these are illustrated in figure 11 as follows:

- *Solar irradiation*: Figure 11(a) illustrates the time profile of solar irradiation levels for various periods of daytime in order to show the behaviors of the circuit according to these levels.
- *Chopper duty cycle*: Figure 11(b) illustrates the time profile of calculated dudty cycle , where its shown that for each irradiation level the duyt cycle increases which cause further increase until maximum obtaied power is achieved.
- *PV array current*: Figure 11(c) illustrates the time profile of PV current, where its shown that high irradiation produces large current and power .

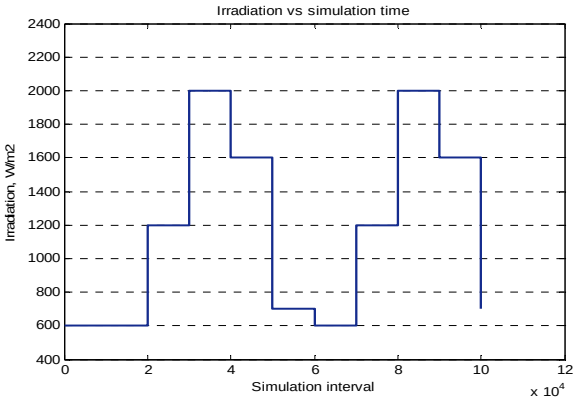

a) Solar irradiations at various daytime intervals.

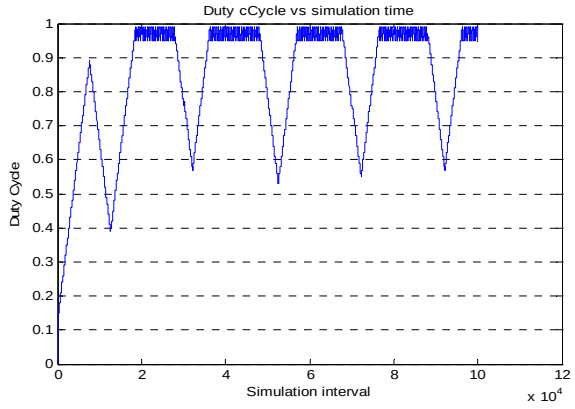

b) Chopper duty cycle.

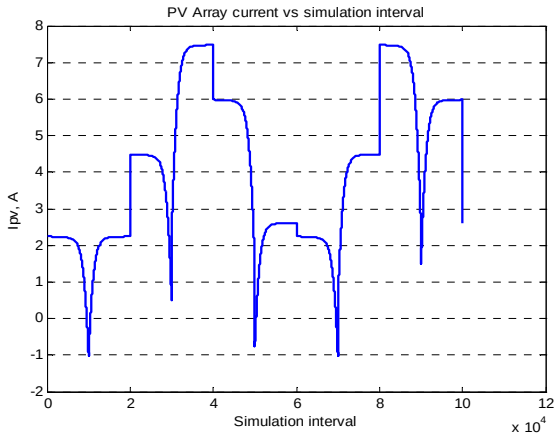

c) Array current of The PV pannel

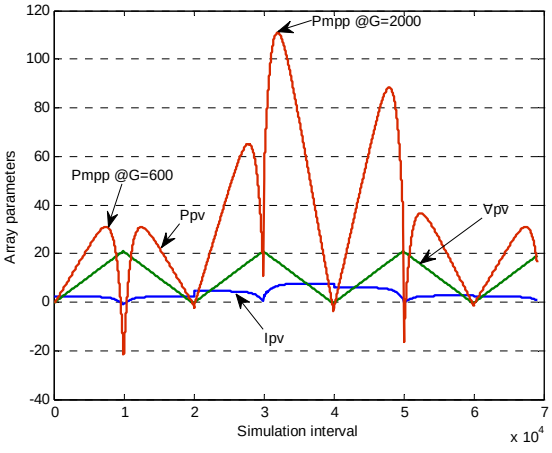

d) PV voltage, current and power

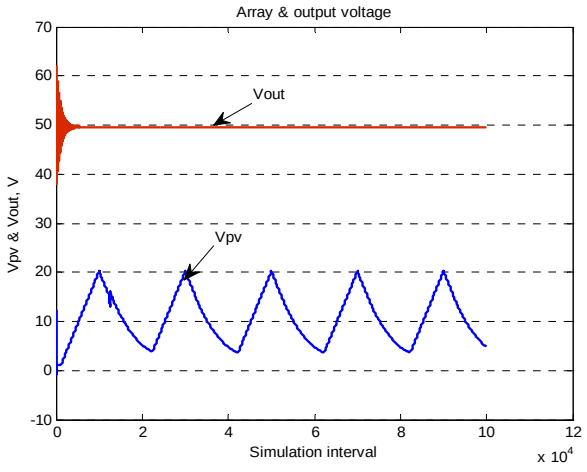

e) PV and chopper voltage

Fig.11: Circuit performances at various irradiations

- *PV voltage, current and power*: Figure 11(d) illustrates the time profile of PV voltage , current and power , where its shown how the power being affected by increasing the irradiation level.

- *Input-output voltage*: Figure 11(e) illustrates the time profile of PV input voltage and output chopper voltage, where its shown how the input voltage varies, while the output voltage is boosted up and fixed at appropriate for the elimination system value.

5. Conclusion

A Sustainable hybrid MPPT-Controlled HB LED-Based Illumination System was developed. This illumination system can be used for many lighting applications since it is more efficient and reliable than existing traditional lighting systems based on incandescent or fluorescent lamps. While the use of HB LEDs adds to the initial cost of the system, it will be paid off in the long term due to their higher reliability, flexible control, and long life time. A simulink model for this illumination system was built in order to study the system behaviors at various irradiation level, the effect of MPPT system and generated duty cycle on chopper operation, which in turn causes better utilization, effecienecy enehancement and loss reduction.

6. References

[1] Donald L. Steeby, “Alternative Energy Sources and Systems,” Delmar Cengage Learning, 2012.
[2] Thomas Kessell, “Introduction to Solar Principles,” Pearson Education, Inc. 2011.
[3] Peter Gevorkian, "Large-Scale Solar Power System Design", Mc Graw Hill Higher Education, 2011.
[4] Issa Batarseh, "Power Electronic Circuits", John Wiley and Sons, Inc. 2004.
[5] Mohammad H. Rashid, "Power Electronics Circuits Devices and Applications", Pearson Education, Inc. 2004.
[6] Daniel W. Hart, "Power Electronics", Mc Graw Hill Higher Education, 2010.
[7] Mohan, Undeland, and Robbins, "Power Electronics Converters Applications and Design", John Wiley and Sons, Inc. 2003.
[8] Shaffer, “Fundamentals of Power Electronics with Matlab”, ISBN# 9781584508526
[9] Kingbright http://www.kingbrightusa.com/default.asp
[10] Lumex http://www.lumex.com/marketingdownloads
[11] Jeff Fallin, "Designing DC/DC converters based on SEPIC topology", Analogue Applications Journal, Power Management, Texas Instruments Incorporated, 4Q, 2008, pp. 18-23
[12] Lin B.R. & Huang C.L., "Analysis and implementation of an integrated SEPIC -forward converter for photovoltaic-based light emitting diode lighting", IET Power Electronics, 2009, Vol.2, Iss.6, pp.635-645.
[13] Hodge B. K., "Alternative Energy Systems & applications", John Willey & Sons, Inc., 2010, pp.114-148.
[14] Chuang Y.C. & Ke Y.L.," High efficiency battery charger with a Buck zero-current switching pulse width modulated converter", 2008, Vol.1, Iss.4, pp433-444.
[15] Jovcic D., "Step-up DC-DC converter for megawatt size applications", IET Power Electronics, 2009, Vol.2, Iss.6, pp.675-685.
[16] Redley R., " Analyzying the Sepic converters", Power System Design Europe, November, 2006, pp.14-18.
[17] Bisogno F.E., Nittayarumphong S., Radecker M., Doprado R.N., " A line power-supply for LED lighting using piezoelectric transformers in class-E topology", proc. IEEE IPEMC'06, 2006, Vol.2, pp1-5.
[18] Joseph T. Verdeyen. “Laser Electronics” 3rd edition Pearson Prentice Hall, 1995.
[19] Matlab and Simulink, The Mathworks, Inc., version R2010, http://www.mathworks.com
[20] Atlas H., Sharaf A.M.," A Photovoltaic array simulation model for Matlab-simulink GUI environment, IEEE, Trans., 2007, pp.341-345.
[21] Chouder A., Silvester S., Malek A., " Simulation of photovoltaic grid connected inverter in case of grid-failure", Revue des energes Renouveables Vol. 9, No4, 2006, pp.285-296.
[22] Buresch M.," Photovoltaic energy systems design and Installation", McGraw-Hill, New York, 1983.

Biographies

AKRAM ABU-AISHEH is an Associate Professor of Electrical and Computer Engineering at the University of Hartford where he has served as the assistant chair of the Electrical and Computer Engineering Department and director of the electronic and computer engineering technology program for two years. Dr. Abu-aisheh has a doctorate in Optical Communications from the Florida Institute of Technology and Master of Science and Bachelor of Science degrees in Electrical Engineering from the University of Florida. His research interests include Fiber Optic Communications, Solar Energy, Power Electronics, and Engineering Education. He has published a book, a book chapter, and several international journals and conference papers. Dr. Abu-aisheh may be contacted at abuaisheh@hartford.edu

SAMEER KHADER is an Associate Professor of Electrical and Computer Engineering at Palestine Polytechnic University (PPU) – Palestine. During the 2010-2011 year he was a visiting professor at the University of Hartford, CT, USA spending his sabbatical year. He is a director of Power Electronics & Signal Processing Research Unit at PPU. Before that he served for ten years as university academic provost, dean of college and Chair of the Electrical & Computer Engineering Department at PPU. His research interests include Electrical machines, Electrical drives, Power Electronics Converters, Renewable Energy Sources and Smart Grids, in addition to engineering education. He has several publications in international journals and conferences. Dr. Khader may be contacted at sameer@ppu.edu

www.icgst.com

A sophisticated Space Vector Pulse Width Modulation Signal Generation for Nine-Level Inverter system for Dual-Fed Induction Motor Drive

G. Sambasiva Rao, K. Chandra Sekhar
Dept. of Electrical Engg, R.V.R & J.C. College of Engineering, Guntur, India
sambasiva.gudapati@gmail.com

Abstract
A sophisticated space vector modulation scheme for a nine-level inverter system for dual-fed induction motor drive, using only the instantaneous sampled reference signals is presented in this paper. The dual-fed structure is realized by opening the neutral-point of the conventional squirrel cage induction motor. The nine-level inversion is obtained by feeding the dual-fed induction motor with symmetrical four-level inverter from one end and symmetrical three-level inverter from other end. The proposed space vector pulse width modulation technique does not require the sector information and look-up tables to select the appropriate switching vectors. The inverter leg switching times are directly obtained from the instantaneous sampled reference signal amplitudes and centers the switching times for the middle space vectors in a sampling time interval, as in the case of conventional space vector pulse width modulation.

Keywords: *dual-fed induction motor, middle space vectors, nine-level inverter, sampled sinusoidal reference signals, space vector PWM.*

Nomenclature

Edc	DC link voltage of an equivalent conventional single two-level Inverter
Ts	Sampling time
E_{A3A5}, E_{B3B5}, E_{C3C5}	Motor phase voltages
Emax, Emin	The maximum and minimum magnitudes of the three sampled sinusoidal reference signals
Eoffset1, Eoffset2	common offset voltages
E^*_{AN}, E^*_{BN}, E^*_{CN}	The modified reference signals after addition of Eoffset1
t_1, t_2	The time durations for the middle inverter space vectors
t_{01}, t_{02}	The time durations for the start and end inverter space vectors
Tx-cross(x=a, b, c)	The time interval, at which the x-phase reference signal, E^*_{XN} crosses the triangular carrier signal
T^*as, T^*bs, T^*cs	The time equivalents of the voltage magnitudes
Tfirst_cross, Tsecond_cross, Tthird_cross	The time intervals, at which the sinusoidal reference signals cross the triangular carrier signals for the first time, second time and third time
T_0	The time interval of the start and end space vector
Tmiddle	The time interval for the middle inverter space vectors

1. Introduction
The two most widely used pulse width modulation (PWM) schemes for multilevel inverters are the carrier-based sine-triangle PWM (SPWM) scheme and the space vector PWM (SVPWM) scheme. The SPWM schemes are more flexible and simpler to implement, but the maximum peak of the fundamental component in the output voltage is limited to 50% of the DC link voltage [1, 2]. The maximum peak of the fundamental component in the output voltage obtained with space vector modulation is 15% greater than with the sine-triangle modulation scheme [2-5]. But the conventional SVPWM scheme requires sector identification and look-up tables to determine the timings for various switching vectors of the inverter, in all the sectors [3, 4]. This makes the implementation of the SVPWM scheme quite complicated. It has been shown that, for two-level inverters, a SVPWM like performance can be obtained with a SPWM scheme by adding a common mode voltage of suitable magnitude, to the sinusoidal reference signals [4 - 6].
The SPWM scheme, when applied to multilevel inverters, uses a number of level-shifted carrier signals to compare with the sinusoidal reference signals [7]. The SVPWM for multilevel inverters [8 - 11] involves mapping of the outer sectors to an inner sub-hexagon sector, will be very complex, as a large number of sectors and inverter vectors are involved.

A modulation scheme is presented in [12], where a fixed common mode voltage is added to the reference signal throughout the modulation range. It has been shown [13] that this common mode voltage addition will not result in a SVPWM-like performance, as it will not centre the middle space vectors in a sampling interval. The common mode voltage to be added in the reference phase voltages, to achieve SVPWM-like performance, is a function of the modulation index for multilevel inverters [13]. A SVPWM scheme based on the above principle has been presented [14], where the switching time for the inverter legs is directly determined from sampled sinusoidal reference signal amplitudes. But it involves region identifications based on modulation indices. While this SVPWM scheme works well for a three-level PWM generation, it cannot be extended to multilevel inverters of levels higher than three, as the region identification becomes more complicated. A carrier-based PWM scheme has been presented [15], where sinusoidal references are added with a proper offset voltage before being compared with carriers, to achieve the performance of a SVPWM. The offset voltage computation is based on a modulus function depending on the DC link voltage, number of levels and the sinusoidal reference signal amplitudes. A SVPWM scheme is presented [18], where the switching time for the inverter legs is directly determined from sampled sinusoidal reference signal amplitudes for five-level inverter where two three-level inverters feed the dual-fed induction motor. A carrier based SPWM scheme is presented [19, 20] for five-level and nine-level inverters. Qualitative SVPWM schemes are presented for five-level inverters in [21, 22].

The objective of this paper is to present an implementation scheme for PWM signal generation for nine-level inverter system for dual-fed induction motor, similar to the SVPWM scheme. In the proposed scheme, the dual-fed induction motor is fed with symmetrical four-level inverter from one end and symmetrical three-level inverter from other end. The PWM switching times for the inverter legs are directly derived from the sampled amplitudes of the sinusoidal reference signals. A simple way of adding an offset voltage to the sinusoidal reference signals, to generate the SVPWM pattern, from only the sampled amplitudes of sinusoidal reference signals, is explained. The proposed SVPWM signal generation does not involve checks for region identification, as in the SVPWM scheme presented in [14]. Also, the algorithm does not require either sector identification or look-up tables for switching vector determination as are required in the conventional multilevel SVPWM schemes [10, 11]. Thus the scheme is computationally efficient when compared to conventional multilevel SVPWM schemes, making it superior for real-time implementation.

2. Nine-level inverter scheme for the dual-fed induction motor

The power circuit of the proposed drive is shown in Figure 1. A symmetrical four-level inverter, Inverter-A and a symmetrical three-level inverter, Inverter-B feed the dual-fed induction motor. The inverter-A is composed of three conventional two-level inverters INV-1, INV-2 and INV-3 in cascade. The Inverter-B is composed of two conventional two-level inverters INV-4 and INV-5 in cascade. The DC link voltages of INV-1, INV-2, INV-3, INV-4 and INV-5 are (2/8)Edc, (2/8)Edc, (2/8)Edc, (1/8)Edc and (1/8)Edc respectively, where Edc is the DC link voltage of an equivalent conventional single two-level inverter drive.

The leg voltage E_{A3n} of phase-A attains a voltage of (2/8)Edc if (i)The top switch S_{31} of INV-3 is turned on (Figure 1) and (ii) The bottom switch S_{24} of INV-2 is turned on. The leg voltage E_{A3n} of phase-A attains a voltage of (4/8)Edc if (i) the top switch S_{31} of INV-3 is turned on (ii) The top switch S_{21} of INV-2 is turned on and (iii)The bottom switch S_{14} of INV-1 is turned on. The leg voltage E_{A3n} of phase-A attains a voltage of (6/8)Edc if (i) the top switch S_{31} of INV-3 is turned on (ii) The top switch S_{21} of INV-2 is turned on and (iii)The top switch S_{11} of INV-1 is turned on. The leg voltage E_{A3n} of phase-A attains a voltage of zero volts if the bottom switch S_{34} of the INV-3 is turned on. Thus the leg voltage E_{A3n} attains four voltages of 0, (2/8)Edc, (4/8)Edc and (6/8)Edc, which is basic characteristic of a 4-level inverter. Similarly the leg voltages E_{B3n} and E_{C3n} of phase-B and phase-C attain the four voltages of 0, (2/8)Edc, (4/8)Edc and (6/8) Edc.

The leg voltage $E_{A5n'}$ of phase-A attains a voltage of (1/8)Edc if (i)The top switch S_{51} of INV-5 is turned on and (ii) The bottom switch S_{44} of INV-4 is turned on. The leg voltage $E_{A5n'}$ of phase-A attains a voltage of (2/8)Edc if (i) The top switch S_{51} of INV-5 is turned on and (ii) The top switch S_{41} of INV-4 is turned on. The leg voltage $E_{A5n'}$ of phase-A attains a voltage of zero volts if the bottom switch S_{54} of the INV-5 is turned on. Thus the leg voltage $E_{A5n'}$ attains three voltages of 0, (1/8)Edc and (2/8)Edc, which is basic characteristic of a 3-level inverter. Similarly the leg voltages $E_{B5n'}$ and $E_{C5n'}$ of phase-B and phase-C attain the three voltages of 0, (1/8)Edc and (2/8)Edc.

Thus, one end of dual-fed induction motor may be connected to a DC link voltage of either zero or (2/8)Edc or (4/8)Edc or (6/8)Edc and other end may be connected to a DC link voltage of either zero or (1/8)Edc or (2/8)Edc. When both the inverters, Inverter-A and Inverter-B drive the induction motor from both ends, nine different levels are attained by each phase of the induction motor. The nine levels generated for phase-A are shown in Table 1.

TABLE 1
THE NINE LEVELS REALIZED IN THE PHASE-A WINDING

Leg-voltage of phase A, E_{A3n}	Leg-voltage of phase A, $E_{A5n'}$	Motor phase voltage $E_{A3A5} = E_{A3n} - E_{A5n'}$	Level
0	(2/8) Edc	-(2/8) Edc	Level 1
0	(1/8)Edc	-(1/8)Edc	Level 2
0	0	0	Level 3
(2/8) Edc	(1/8) Edc	(1/8)Edc	Level 4
(2/8) Edc	0	(2/8)Edc	Level 5
(4/8) Edc	(1/8) Edc	(3/8)Edc	Level 6
(4/8) Edc	0	(4/8) Edc	Level 7
(6/8) Edc	(1/8) Edc	(5/8) Edc	Level 8
(6/8) Edc	0	(6/8) Edc	Level 9

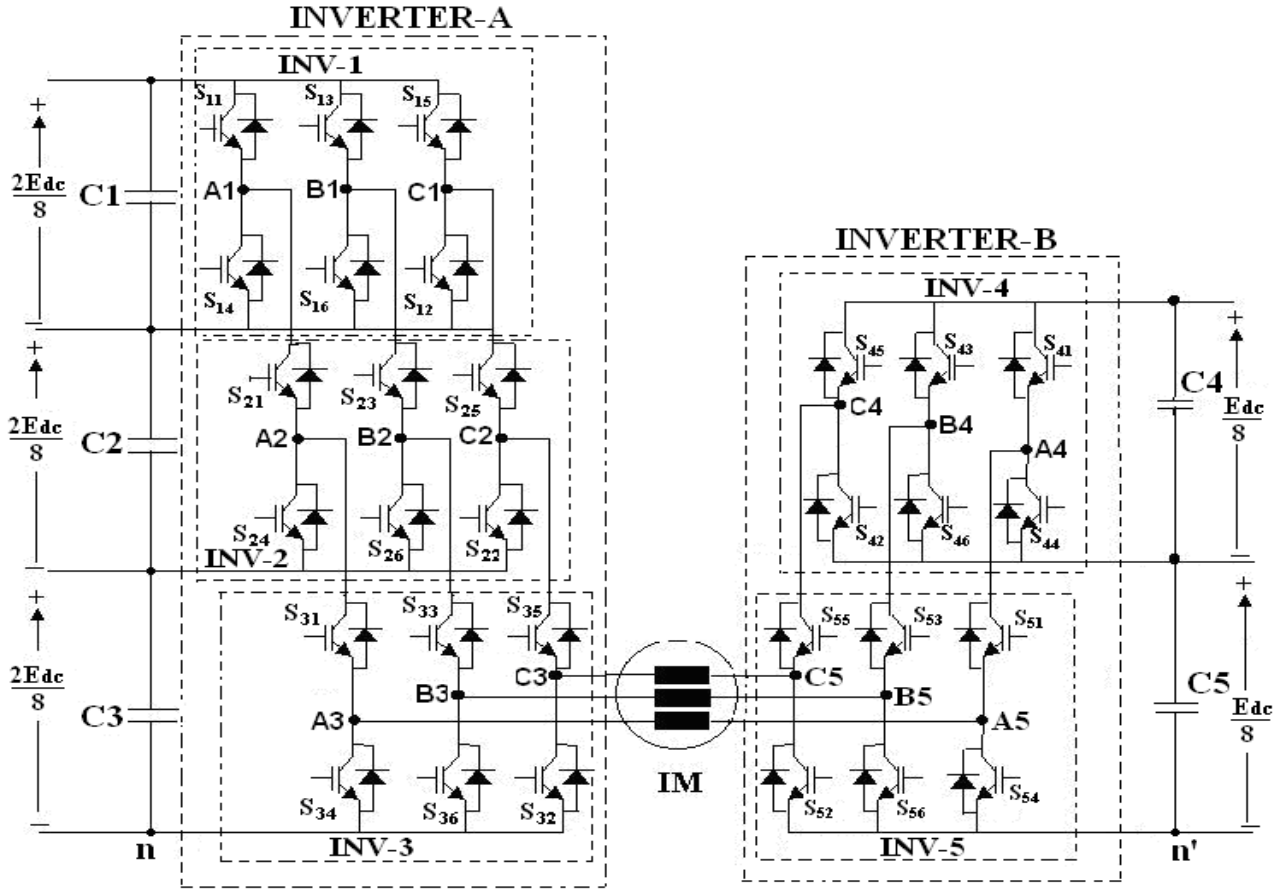

Figure 1. Schematic circuit diagram of the proposed 9-level inverter drive scheme.

3. Proposed SVPWM in linear modulation range

For two-level inverters, in the SPWM scheme, each sinusoidal reference signal is compared with the triangular carrier signal and the individual phase voltages are generated [1]. To attain the maximum possible peak amplitude of the fundamental phase voltage, a common offset voltage, Eoffset1 is added to the sinusoidal reference signals [5, 12], where the magnitude of Eoffset1 is given by

$$Eoffset1 = -(E\max + E\min)/2 \qquad (1)$$

Where Emax and Emin are the maximum and minimum magnitudes of the three sampled sinusoidal reference signals respectively, in a sampling time interval. The addition of Eoffset1, results in the active space vectors being centered, making the SPWM scheme equivalent to the SVPWM scheme [3]. In a sampling time interval, the sinusoidal reference signal which has lowest magnitude crosses the triangular carrier signal first, and causes the first transition in the inverter switching state and the sinusoidal reference signal, which has the maximum magnitude, crosses the triangular carrier signal last and causes the last switching transition in the inverter switching states in a two-level SVPWM scheme [5, 13].

For nine-level inverter, the modified sinusoidal reference signals (E^*_{AN}, E^*_{BN} and E^*_{CN}) after addition of offset voltage Eoffset1, are shown in figure 2 along with eight triangular carrier signals T1 to T8. Each time a sinusoidal reference signal crosses the triangular carrier signal, it causes a change in the inverter switching state. The changes in phase voltage and their time intervals are shown in Figure 3 in a sampling time interval Ts. The sampling time interval Ts can be split into four time intervals t_{01}, t_1, t_2 and t_{02}. The time intervals t_{01} and t_{02} are the time durations for the start and end inverter space vectors respectively and the time intervals t_1 and t_2 are the time durations for the middle inverter space vectors (active space vectors), in a sampling time interval Ts. It should be observed from Figure 3 that the middle space vectors are not centered in a sampling time interval Ts. Because of the level-shifted eight triangular carrier signals (Figure 2), the first crossing and the last crossing of the sinusoidal reference signal cannot always be the minimum and the maximum magnitude of the three sampled sinusoidal reference signals, in a sampling time interval. Thus the offset voltage, Eoffset1 is not sufficient to center the middle inverter space vectors, in a multilevel PWM system (Figure 3). Hence an additional offset (offset2) has to be added to the sinusoidal reference signals of Figure 2, so that the middle inverter space vectors can be centered in a sampling time interval, same as a two-level SVPWM system [3].

4. Determination of the offset voltage for a nine-level inverter

Figure 2 shows modified sinusoidal reference signals and eight triangular carrier signals used for PWM generation for nine-level inverter. The modified sinusoidal reference signals are given by

$$\begin{aligned} E^*_{AN} &= E_{AN} + Eoffset1 \\ E^*_{BN} &= E_{BN} + Eoffset1 \\ E^*_{CN} &= E_{CN} + Eoffset1 \end{aligned} \quad (2)$$

where E_{AN}, E_{BN} and E_{CN} are the sampled amplitudes of sinusoidal reference signals during the current sampling time interval and Eoffset1 is calculated from equation (1). The time interval, at which the A-phase sinusoidal reference signal, E^*_{AN} crosses the triangular carrier signal, is termed as Ta-cross (Figure 4). Similarly, the time intervals, when the B-phase and C-phase sinusoidal reference signals, E^*_{BN} and E^*_{CN} cross the triangular carrier signals, are termed as Tb-cross and Tc-cross respectively. Figure 4 shows a sampling time interval when the A-phase sinusoidal reference signal is in the triangular carrier region T7 while the B-phase sinusoidal reference signal and C-phase sinusoidal reference signal are in carrier region T8 and T1 respectively. As shown in Figure 4, the time interval, Ta-cross, at which the A-phase sinusoidal reference signal crosses the triangular carrier signal is directly proportional to the phase voltage amplitude, ($E^*_{AN} - 3Edc/8$). The time interval, Tb-cross, at which the B-phase sinusoidal reference signal crosses the triangular carrier signal, is proportional to ($E^*_{BN} + 4Edc/8$) and the time interval, Tc-cross, at which the C-phase sinusoidal reference signal crosses the triangular carrier signal, is proportional to (E^*_{CN}). Therefore

$$\begin{aligned} Ta-cross &= (E^*_{AN} - 3Edc/8)\left(\frac{Ts}{Edc/8}\right) = T^*as - 3Ts \\ Tb-cross &= (E^*_{BN} + 4Edc/8)\left(\frac{Ts}{Edc/8}\right) = T^*bs + 4Ts \\ Tc-cross &= (E^*_{CN})\left(\frac{Ts}{Edc/8}\right) = T^*cs \end{aligned} \quad (3)$$

Where T^*as, T^*bs and T^*cs are the time equivalents of the voltage magnitudes. The proportionality between the time equivalents and corresponding voltage magnitudes is defined as follows [6]:

$$\begin{aligned} (Edc/8)/Ts &= E^*_{AN}/T^*as \\ (Edc/8)/Ts &= E^*_{BN}/T^*bs \\ (Edc/8)/Ts &= E^*_{CN}/T^*cs \\ (Edc/8)/Ts &= Eoffset1/Toffset1 \end{aligned} \quad (4)$$

The time interval, at which the sinusoidal reference signals cross the triangular carrier signals for the first time, is termed as Tfirst_cross. Similarly, the time intervals, at which the sinusoidal reference signals cross the triangular carrier signals for the second and third time, are termed as, Tsecond_cross and Tthird_cross respectively, in a sampling time interval Ts.

$$\begin{aligned} Tfirst_cross &= \min(Ta-cross, Tb-cross, Tc-cross) \\ Tsecond_cross &= mid(Ta-cross, Tb-cross, Tc-cross) \\ Tthird_cross &= \max(Ta-cross, Tb-cross, Tc-cross) \end{aligned} \quad (5)$$

The time intervals, Tfirst_cross, Tsecond_cross and Tthird_cross, directly decide the switching times for the different inverter voltage vectors, forming a triangular sector, during one sampling time interval Ts. The time intervals for the start and end space vectors, are t_{01}= Tfirst_cross, t_{02}= (Ts − Tthird_cross), respectively (Figure 3). The middle space vectors are centered by adding a time offset, Toffset2 to Tfirst_cross, Tsecond_cross and Tthird_cross. The time offset, Toffset2 is determined as follows. The time interval for the middle inverter space vectors, Tmiddle, is given by:

$$Tmiddle = Tthird_cross - Tfirst_cross \quad (6)$$

The time interval of the start and end space vector is

$$T_0 = Ts - Tmiddle \quad (7)$$

Thus the time interval of the start space vector is given by

$$T_0/2 = Tfirst_cross + Toffset2$$

Therefore

$$Toffset2 = T_0/2 - Tfirst_cross \quad (8)$$

In this way, we can obtain offset voltages to be added for remaining samples during the time period of sinusoidal reference signal and for different modulation indices.

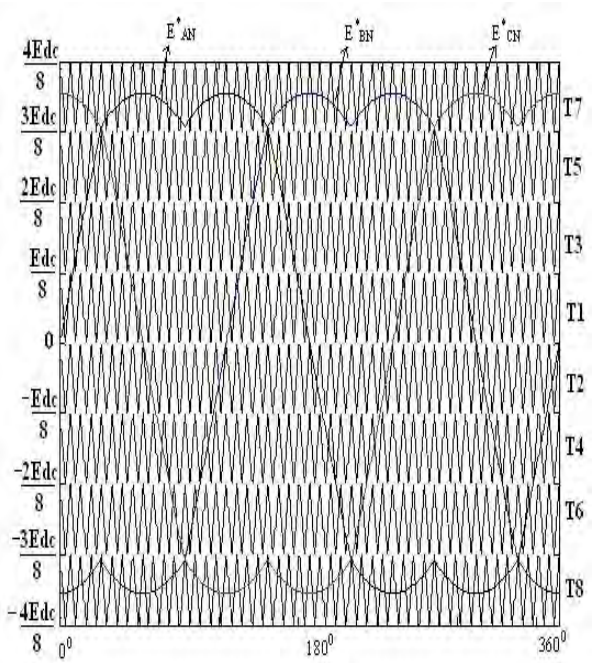

Figure 2. Modified sinusoidal reference signals and triangular carrier signals for a nine-level PWM scheme

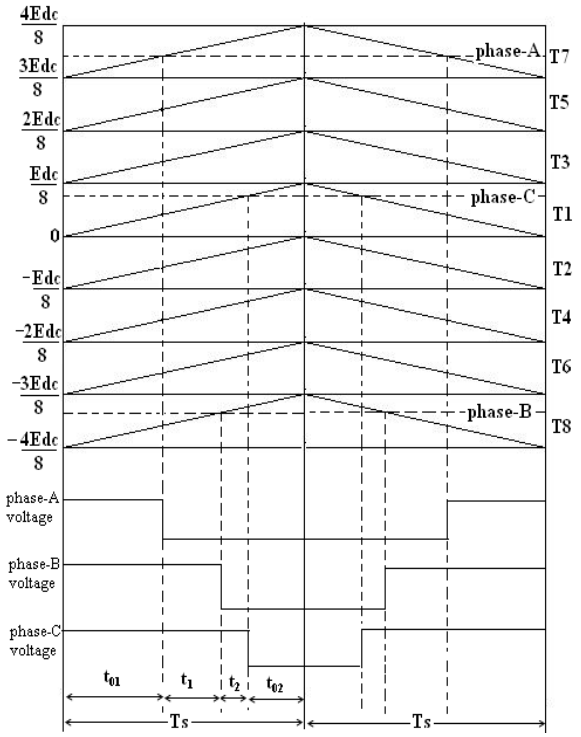

Figure 3. Inverter switching vectors and their switching time durations during sampling time interval Ts

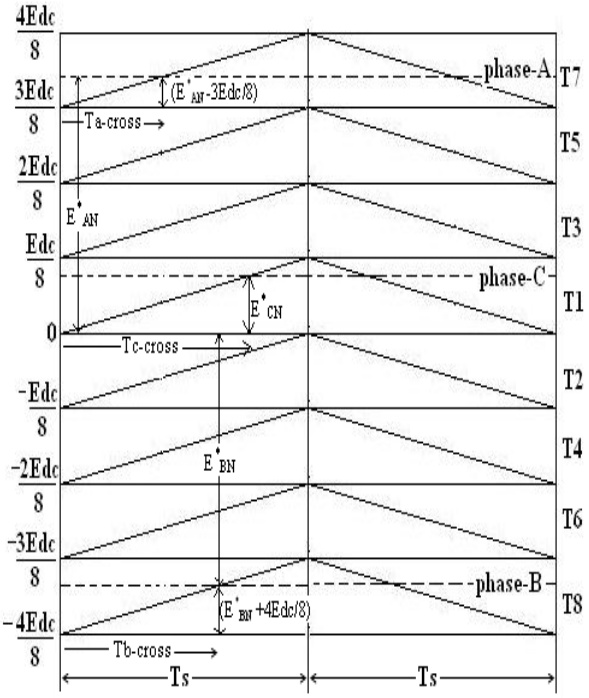

Figure 4. Determination of the Ta-cross, Tb-cross and Tc-cross during sampling interval Ts

5. Simulation results and discussion

The proposed SVPWM scheme is simulated using MATLAB environment with open loop E/f control for different modulation indices. The speed reference is translated to the frequency and voltage commands maintaining E/f. The modified three reference sinusoidal signals which are added by the total offset voltage to make SPWM scheme equivalent to the SVPWM scheme, are simultaneously compared with the triangular carrier set. A DC link voltage (Edc) of 800 volts is assumed for simulation studies. Figure 5(a) shows the total offset voltage to be added to sinusoidal reference signals to make SPWM equivalent to the SVPWM in the lowest speed range which corresponds to two-level mode when modulation index is 0.1, figure 5(b) shows the A-phase sinusoidal reference signal after offset voltage is added and Figure 5(c) shows the motor phase voltage (E_{A3A5}). Figure 6 to Figure 12 show the motor waveforms in the next speed ranges which corresponds to three-level mode to nine-level mode when modulation indices are 0.2, 0.3, 0.42, 0.53, 0.62, 0.74 and 0.85 respectively. It can be observed that the motor phase voltage during 9-level operation is very smooth and close to the sinusoid with lower harmonics.

6. Conclusion

A modulation scheme of SVPWM for nine-level inverter system for dual-fed induction motor drive is presented. The centering of the middle inverter space vectors of the SVPWM is accomplished by the addition of an offset voltage signal to the sinusoidal reference signals, derived from the sampled amplitudes of the sinusoidal reference signals. The SVPWM technique, presented in this paper does not require any sector identification, as is required in conventional SVPWM schemes. The proposed scheme eliminates the use of look-up table approach to switch the appropriate space vector combination as in conventional SVPWM schemes. This reduces the computation time required to determine the switching times for inverter legs, making the algorithm suitable for real-time implementation.

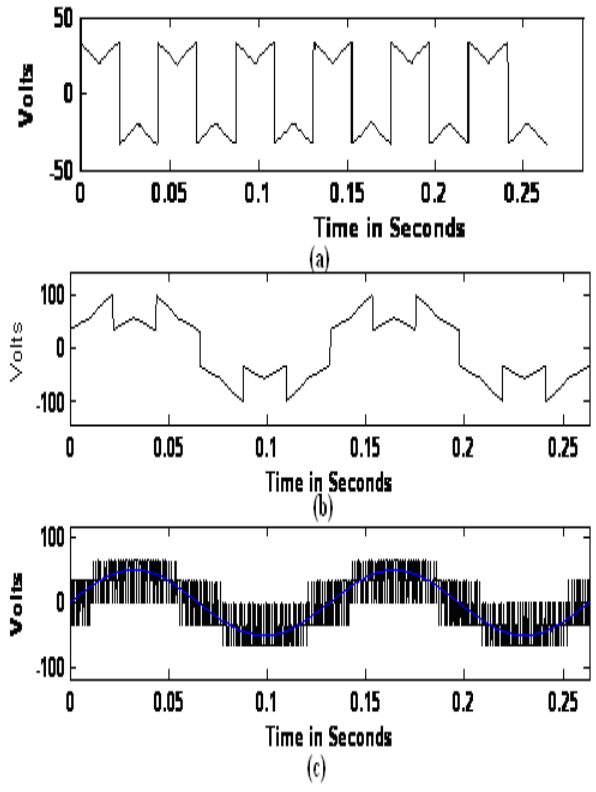

Figure 5. (a)The total offset voltage to be added to sinusoidal reference signals (b)The A-phase sinusoidal reference signal after offset voltage is added (c) Motor phase voltage when M=0.1 (2-level operation)

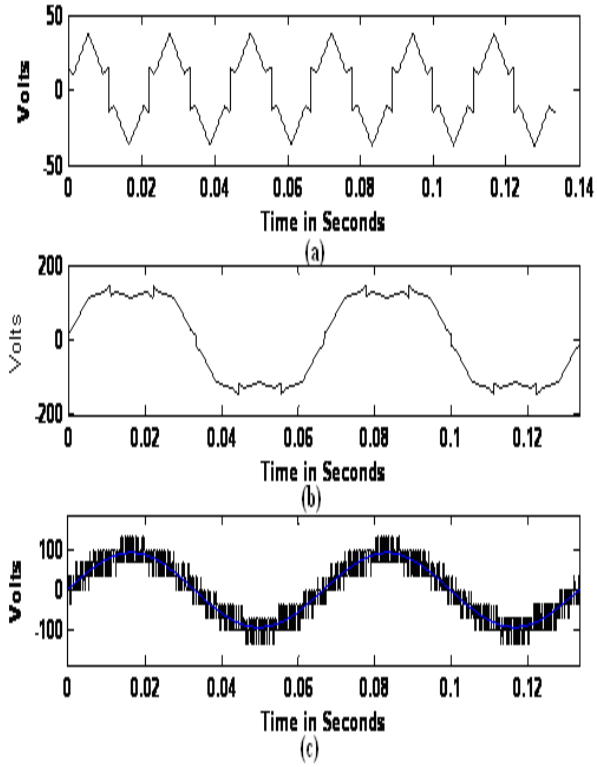

Figure 6. (a)The total offset voltage to be added to sinusoidal reference signals (b)The A-phase sinusoidal reference signal after offset voltage is added (c) Motor phase voltage when M=0.2 (3-level operation)

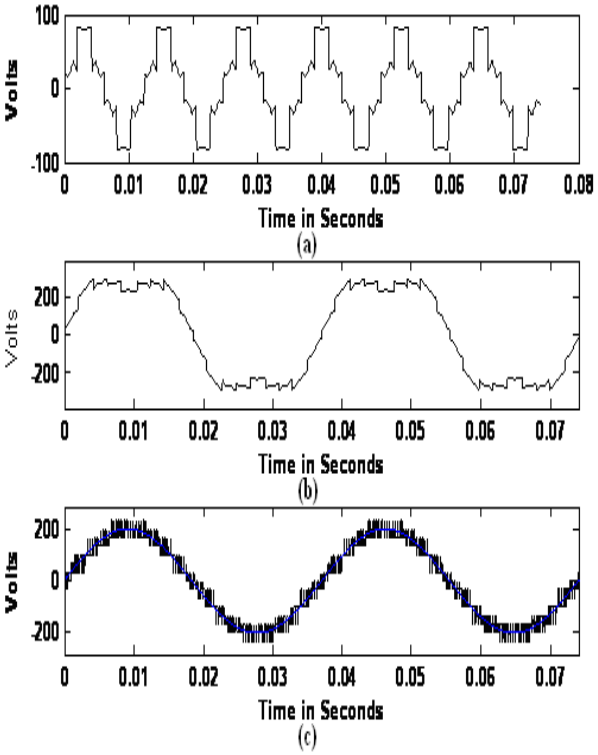

Figure 8. (a)The total offset voltage to be added to sinusoidal reference signals (b)The A-phase sinusoidal reference signal after offset voltage is added (c) Motor phase voltage when M=0.42 (5-level operation)

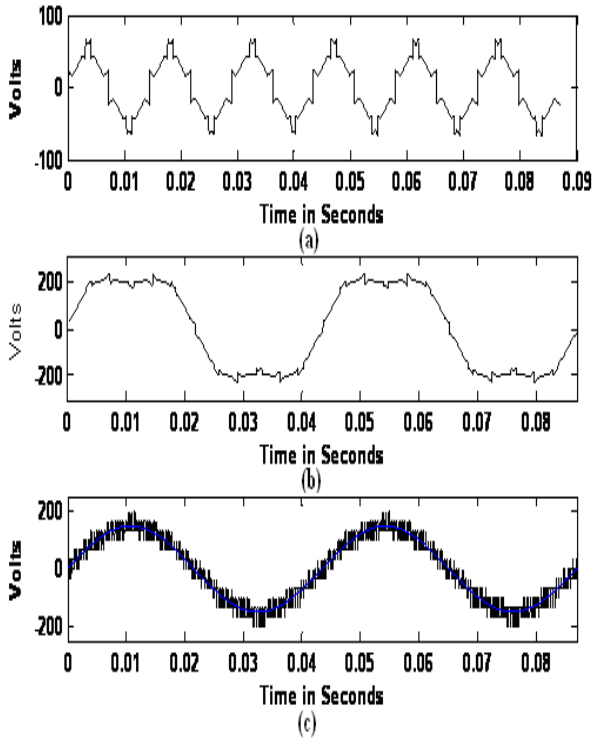

Figure 7. (a)The total offset voltage to be added to sinusoidal reference signals (b)The A-phase sinusoidal reference signal after offset voltage is added (c) Motor phase voltage when M=0.3 (4-level operation)

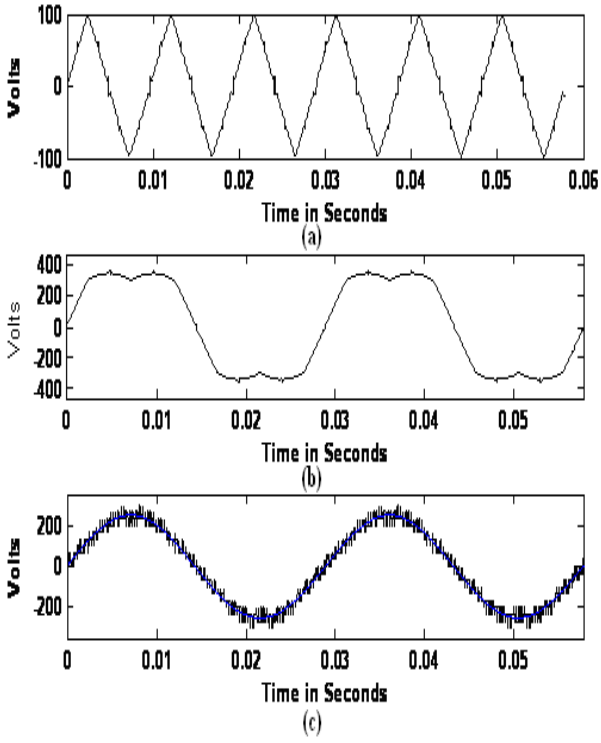

Figure 9. (a)The total offset voltage to be added to sinusoidal reference signals (b)The A-phase sinusoidal reference signal after offset voltage is added (c) Motor phase voltage when M=0.53 (6-level operation)

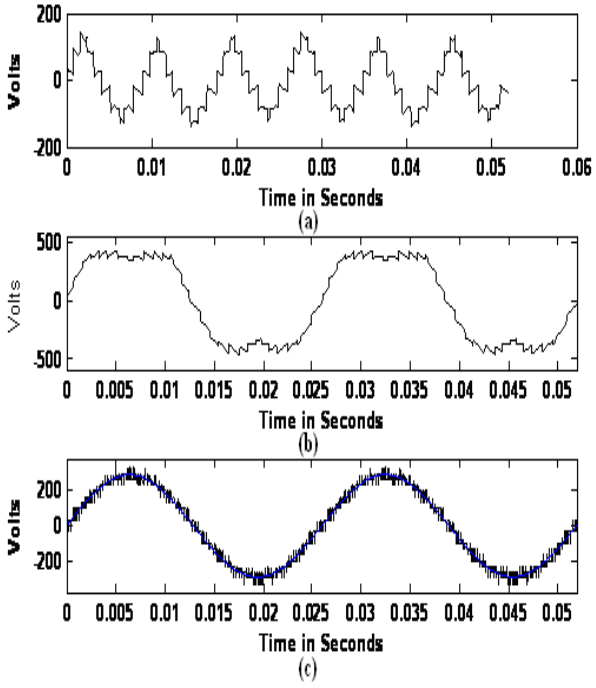

Figure 10. (a)The total offset voltage to be added to sinusoidal reference signals (b)The A-phase sinusoidal reference signal after offset voltage is added (c) Motor phase voltage when M=0.62 (7-level operation)

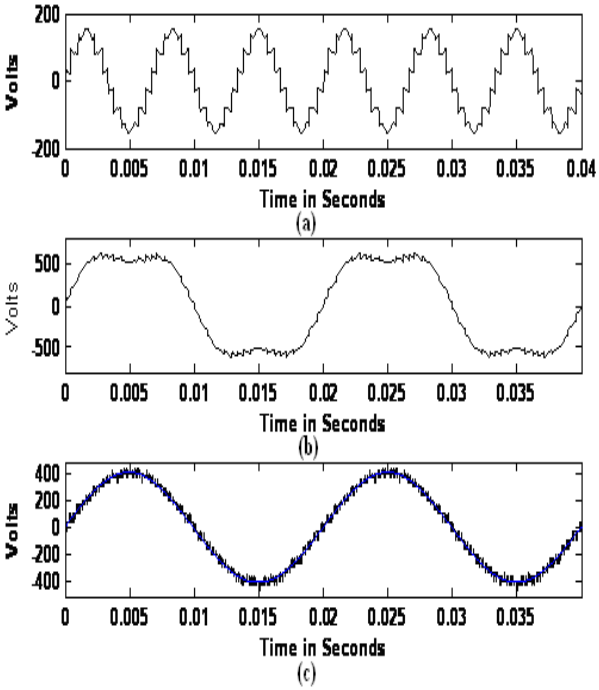

Figure 12. (a)The total offset voltage to be added to sinusoidal reference signals (b)The A-phase sinusoidal reference signal after offset voltage is added (c) Motor phase voltage when M=0.85 (9-level operation)

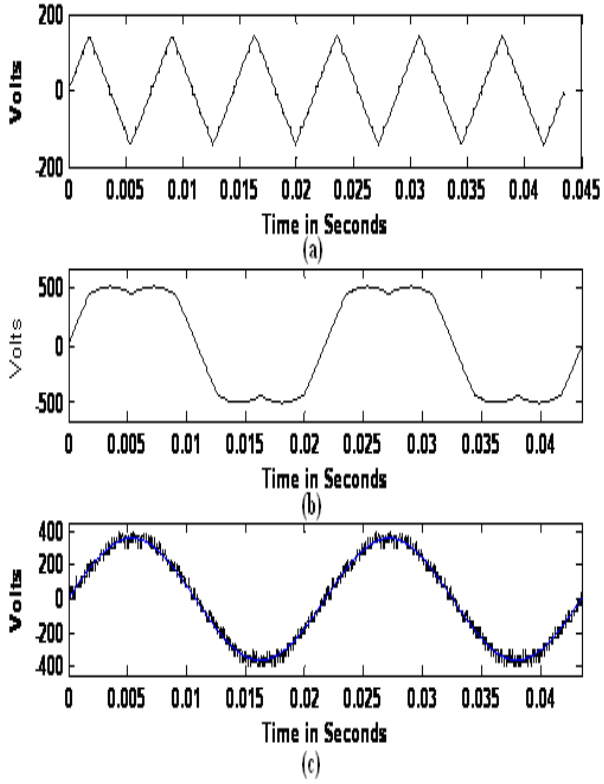

Figure 11. (a)The total offset voltage to be added to sinusoidal reference signals (b)The A-phase sinusoidal reference signal after offset voltage is added (c) Motor phase voltage when M=0.74 (8-level operation)

7. References

[1] Holtz, J., "Pulsewidth modulation–A survey," IEEE Trans. Ind. Electron., 30 (5), pp. 410–420, 1992.

[2] Zhou, K., and Wang, D., "Relationship between space-vector modulation and three-phase carrier-based PWM: A comprehensive analysis," IEEE Trans. Ind. Electron., 49 (1), pp. 186–196, 2002.

[3] Van der Broeck, Skudelny, H.C., and Stanke, G.V., "Analysis and realisation of a pulsewidth modulator based on voltage space vectors," IEEE Trans. Ind. Appl., 24 (1), pp. 142–150, 1988.

[4] Boys, J.T., and Handley, P.G., "Harmonic analysis of space vector modulated PWM waveforms," IEE Proc. Electr. Power Appl.,137 (4), pp. 197–204, 1990.

[5] Holmes, D.G., "The general relationship between regular sampled pulse width modulation and space vector modulation for hard switched converters," Conf. Rec. IEEE Industry Applications Society(IAS) Annual Meeting, pp. 1002–1009, 1992.

[6] Kim, J., and Sul, S. "A novel voltage modulation technique of the Space Vector PWM," Proc. Int. Power Electronics Conf., Yokohama, Japan, pp. 742–747, 1995.

[7] Carrara, G.,Gardella, S.G., Archesoni,M., Salutari, R., and Sciutto, G., "A new multi-level PWM method: A theoretical analysis," IEEE Trans. Power Electron., 7 (3), pp. 497–505, 1992

[8] K.Chandra Sekhar, G.Tulasi Ram Das, "An Eight-level Inverter System for an Induction Motor with Open-end Windings" IEEE PEDS 2005, pp:219-223, 2005.

[9] K.Chandra Sekhar, G.Tulasi Ram Das, "A Nine-Level Inverter System for an Open-End Winding

Induction Motor Drive" in preceedings of IEEE ICIEA 2006.

[10]Shivakumar, E.G., Gopakumar, K., Sinha, S.K., Andre, Pittet, and Ranganathan, V.T., "Space vector PWM control of dual inverter fed open-end winding induction motor drive," Proc. Applied Power Electronics Conf. (APEC), pp. 339–405, 2001.

[11]Suh, J., Choi, C., and Hyun, D., "A new simplified space vector PWM method for three-level inverter," Proc. IEEE Applied Power Electronics Conf. (APEC), pp. 515–520, 1999.

[12]Baiju, M.R., Mohapatra, K.K., Somasekhar, V.T., Gopakumar, K., and Umanand, L. "A five-level inverter voltage space phasor generation for an open-end winding induction motor drive," IEE Proc. Electr. Power Appl., 150 (5), pp. 531–538, 2003.

[13]Wang, FEI, "Sine-triangle versus space vector modulation for threelevel PWM voltage source inverters," Proc. IEEE-IAS Annual Meeting, Rome, pp. 2482–2488, 2000.

[14]Baiju, M.R., Gopakumar, K., Somasekhar, V.T., Mohapatra, K.K., and Umanand, L., "A space vector based PWMmethod using only the instantaneous amplitudes of reference phase voltages for three-level inverters," EPE J., 13 (2), pp. 35–45, 2003.

[15]McGrath, B.P., Holmes, D.G., and Lipo, T.A., "Optimized space vector switching sequences for multilevel inverters," Proc. IEEE Applied Power Electronics Conf. (APEC), pp. 1123–1129, 2001.

[16]Krah, J., and Holtz, J., "High performance current regulation and efficient PWM Implementation for low inductance servo motors," IEEE Trans. Ind. Appl., 36 (5), pp. 1039–1049, 1999.

[17]Somasekhar, V.T., and Gopakumar, K., "Three-level inverter configuration cascading two 2-level inverters," IEE Proc. Electr. Power Appl., 150 (3), pp. 245–254, 2003.

[18]R.S.Kanchan, M.R.Baiju, K.K.Mohapatra, P.P.Ouseph and K.Gopakumar, "Space vector PWM signal generation for multilevel inverters using only the sampled amplitudes of reference phase voltages," IEE Proc.-Electr. Power Appl., 152 (2), pp.297-309, March 2005.

[19]M.R.Baiju,K.Gopakumar,K.K.Mohapatra, V.T Somasekhar and L.Umanand, "Five-Level inverter voltage-space vector phasor generation for an Open-End Winding Induction Motor Drive". In: IEE proc.-power Appl., 150 (5), pp.531-538, Sep2003.

[20]G.Sambasiva Rao, K.Chandra Sekhar "A novel nine-level inverter system for Dual- fed induction motor drive" International Journal of Engineering Research & Industrial Applications, 4 (III), pp: 159-176, August 2011.

[21] P.Satish Kumar, J.Amarnath, S.V.L. Narasimham, "A Qualitative Space Vector PWM Algorithm for a Five-level Neutral Point Clamped Inverter" ICGST International Journal on Automatic Control and Systems Engineering, ACSE, 9 (I), pp:43-50, 2009.

[22]V. Naga Bhaskar Reddy and V. Narasimhulu and Dr. Ch. Sai Babu, "control of cascaded multilevel inverter by using carrier based pwm technique and implemented to induction motor drive" ICGST International Journal on Automatic Control and Systems Engineering, ACSE, 10 (II), pp:11-18, December 2010.

Biographies

G.Sambasiva Rao received B.E. degree in Electrical & Electronics Engineering from Andhra University Engineering College, Visakha Patnam, India in 2000 and M.E. with Power Electronics & Industrial Drives from Sathyabama Institute of Science and Technology, Chennai, India in 2006. Since 2006, he has been with R.V.R & J.C.College of engineering as Lecturer. Presently he is a part-time research student at J.N.T.U College of Engineering, Hyderabad- 500072, India, working towards his doctoral degree.

Dr.K.Chandra Sekhar received his B.Tech degree in Electrical & Electronics Engineering from V.R.Siddartha Engineering College, Vijayawada, India in 1991 and M.Tech with Electrical Machines & Industrial Drives from Regional Engineering College, Warangal, India in 1994. He Received the PhD degree from the J.N.T.U College of Engineering, Hyderabad- 500072, India in 2008. He is having 16 years of teaching experience. Currently he is professor and Head in the Department of EEE, R.V.R & J.C. College of Engineering, Guntur, India. His Research interests are Power Electronics, Industrial Drives & FACTS Devices.

www.icgst.com

Simple and Novel Generalized Scalar PWM Algorithm for Multilevel Inverter Fed Direct Torque Controlled Induction Motor

C. Harikrihsna[1], T. Bramhananda Reddy[2], J. Amarnath[3], and S. Kamakshaiah[3]
[1]*Mother Teresa Institute of Science and Technology, Sathupally, Andhra Pradesh, India*
[2]*G. Pulla Reddy Engineering College (autonomous), Kurnool, Andhra Pradesh, India*
[3]*JNTUH, Kukatpally, Hyderabad, Andhra Pradesh, India*
chalasaniharikrishna@gmail.com, [tbnr, amarnathjinka@rediffmail.com], kamkshaiahsatram@yahoo.co.in

Abstract
This paper presents a simple and novel generalized PWM algorithm for n-level multilevel inverter fed direct torque controlled induction motor drives. The proposed algorithm does not use the angle and sector information and hence reduces the complexity involved in the PWM algorithm. The proposed algorithm has been developed by using the concept of imaginary switching times, which are proportional to the instantaneous phase voltages only. The proposed algorithm generates the modulating waveforms for a n-level inverter, which will be compared with the level shifted triangular carriers to generate the switching pulses to the inverter. To validate the proposed algorithm several numerical simulation studies have been carried out and results are presented. From the simulation results, it can be observed that the proposed algorithm gives reduced harmonic distortion with increased number of levels.

Keywords: *Space vector PWM, Multi Level Inverter DTC, Induction Motor.*

1. Introduction
All most the DC drives are replaced by AC drives because of its variable speed characteristics. The invention of field oriented control (FOC) algorithm has been made a renaissance in the high-performance variable speed drive applications. The FOC algorithm gives the decoupling control of torque and flux of an induction motor drive and control the induction motor similar to a separately excited dc motor [1]. But, the complexity involved in the FOC algorithm is more due to reference frame transformations. To reduce the complexity involved, a new control strategy called as direct torque control (DTC) has been proposed in [2]. A detailed comparison is brought between FOC and DTC in [3] and concluded that DTC gives fast torque response when compared with the FOC. Though, FOC and DTC give fast transient and decoupled control, these operate the inverter at variable switching frequency due to hysteresis controllers. Moreover, the steady state ripples in torque, flux and currents are high in DTC. To reduce the steady state ripples, discrete space vector modulation (DSVM) algorithm has been proposed in [4]. Though, DSVM algorithm reduces the torque ripple up to some extent, it gives variable switching frequency operation of the inverter.

To reduce the harmonic distortion and to obtain the constant switching frequency operation of the inverter, nowadays many researchers have focused their interest on pulsewidth modulation (PWM) algorithms. A detailed survey on various PWM algorithms is carried out in [5] and concluded that space vector pulsewidth modulation (SVPWM) algorithm gives good performance. The generation of switching pulses in SVPWM algorithm is given in [6]. Though the SVPWM algorithm gives good performance, the complexity involved is more due to angle and sector calculations. To reduce the complexity involved in SVPWM algorithm, carrier based SVPWM algorithm is developed in [7] by adding the offset voltage to the reference phase voltages. Hence, to reduce the ripples and to obtain the constant switching frequency operation of the inverter, SVPWM algorithm is used for DTC in the literature [8]-[9].

The two-level inverter fed DTC drives are suitable for low power applications only. In order to meet the medium and high power applications, nowadays multilevel inverters are becoming popular. A diode clamped three level inverter fed induction motor drive is presented in [10]. A detailed survey on various types of multilevel inverters is given in [11]. But, as the number of levels increases, the complexity involved in the PWM algorithms also increases. To reduce the complexity involved in the SVPWM algorithm, a simplified SVPWM algorithm is presented for three-level inverter in [12].

To reduce the complexity, a novel voltage modulation algorithm is presented in [13] by using the concept of effective time. By extending the same concept, various PWM algorithms have been generated for two-level inverters in [14]. The concept of the PWM algorithms which is presented in [13]-[14] is extended for multilevel inverters in [15].

This paper presents a simple generalized scalar PWM algorithm for 2-, 3-, 5- and 7-level inverter. The proposed algorithm has been developed by using the concept of imaginary switching times, which are proportional to the instantaneous sampled phase voltages only. Moreover, the proposed algorithm does not require the calculation of angle and sector information and hence reduces the complexity involved in the PWM algorithm.

2. Simplified SVPWM Algorithm for Two-level inverter

To reduce the complexity involved in the conventional SVPWM algorithm and execution time due to longer calculations, a simplified SVPWM algorithm has been developed using the concept of imaginary switching times. In this approach, the actual switching times for each inverter leg are deduced directly as a simple form. The proposed approach is based on the instantaneous values of the reference voltages of a, b and c phases only. This method does not depend on the magnitude of the reference voltage space vector and its relative angle with respect to the reference axis. The transformation from two-phase voltages to three-phase voltages can be obtained from the stationary frame reference voltages as given in (1)

$$\begin{bmatrix} V_{an} \\ V_{bn} \\ V_{cn} \end{bmatrix} = \begin{bmatrix} 1 & 0 \\ -1/2 & -\sqrt{3}/2 \\ -1/2 & +\sqrt{3}/2 \end{bmatrix} \begin{bmatrix} V_q \\ V_d \end{bmatrix} \quad (1)$$

If the reference voltage vector lies in the first sector as shown in Figure 1, then the actual switching times can be deduced as

$$\begin{aligned} T_1 &= \frac{3V_{ref}}{2V_{dc}} \frac{Sin(60^o - \alpha)}{Sin60^o} * T_s \\ &= \frac{\sqrt{3}}{V_{dc}} \left(\frac{\sqrt{3}}{2} V_{ref} \cos\alpha - \frac{1}{2} V_{ref} \sin\alpha \right) * T_s \end{aligned} \quad (2)$$

$$\begin{aligned} T_2 &= \frac{3V_{ref}}{2V_{dc}} \frac{Sin\alpha}{Sin60^o} * T_s \\ &= \frac{\sqrt{3}}{V_{dc}} \left(V_{ref} \cos\alpha \right) * T_s \end{aligned} \quad (3)$$

But from Figure 1 it can be observed that $V_q = V_{ref} \cos\alpha$ and $V_d = -V_{ref} \sin\alpha$. Hence, the active vector times can be simplified as

$$\begin{aligned} T_1 &= \frac{\sqrt{3}}{V_{dc}} \left(\frac{\sqrt{3}}{2} V_q + \frac{1}{2} V_d \right) * T_s \\ &= \frac{T_s}{V_{dc}} \left(V_q + \left(\frac{1}{2} V_q + \frac{\sqrt{3}}{2} V_d \right) \right) * T_s \\ &= \frac{T_s}{V_{dc}} V_{an} - \frac{T_s}{V_{dc}} V_{bn} \equiv T_{an} - T_{bn} \end{aligned} \quad (4)$$

and

$$\begin{aligned} T_2 &= \frac{\sqrt{3}}{V_{dc}} (-V_d) * T_s = \frac{T_s}{V_{dc}} \left(-\sqrt{3} * V_d \right) \\ &= \frac{T_s}{V_{dc}} \left[\left(\frac{-1}{2} V_q - \frac{\sqrt{3}}{2} V_d \right) - \left(\frac{-1}{2} V_q + \frac{\sqrt{3}}{2} V_d \right) \right] \\ &= \frac{T_s}{V_{dc}} V_{bn} - \frac{T_s}{V_{dc}} V_{cn} \equiv T_{bn} - T_{cn} \end{aligned} \quad (5)$$

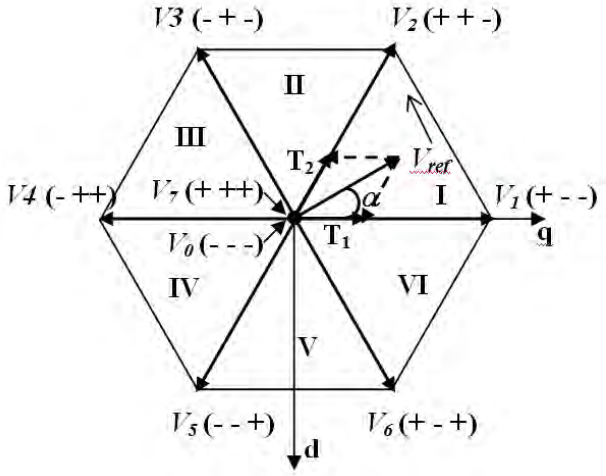

Figure. 1 Voltage space vectors produced by an inverter

From (4) – (5), the imaginary switching time periods proportional to the instantaneous values of the reference phase voltages are defined as

$$\begin{aligned} T_{an} &\equiv \left(\frac{T_s}{V_{dc}} \right) V_{an} \\ T_{bn} &\equiv \left(\frac{T_s}{V_{dc}} \right) V_{bn} \\ T_{cn} &\equiv \left(\frac{T_s}{V_{dc}} \right) V_{cn} \end{aligned} \quad (6)$$

Hence, from (4) – (5), the active vector switching times T_1 and T_2, if the reference voltage vector falls in sector-1 may be expressed as

$$T_1 = T_{an} - T_{bn} \; ; \qquad T_2 = T_{bn} - T_{cn} \quad (7)$$

Thus, the active voltage vector switching times can be represented by the time difference between the imaginary switching time periods. In the SVPWM algorithm, when the reference voltage vector falls in the first sector, the imaginary switching time which is proportional to the a-phase (T_{an}) has a maximum value, the imaginary switching time which is proportional to the c-phase (T_{cn}) has a minimum value and the imaginary switching time which is proportional to the b-phase (T_{bn}) is neither minimum nor maximum switching time. Thus, in general to calculate the active vector switching times, the maximum and minimum values of imaginary switching times are calculated in every sampling time as given in (8) – (9).

$$T_{\max} = Max(T_{an}, T_{bn}, T_{cn}) \quad (8)$$

$$T_{\min} = Min(T_{an}, T_{bn}, T_{cn}) \quad (9)$$

The effective time T_{eff} can be defined as the time difference between $T_{\max}$ and $T_{\min}$ and can be given as in (10).

$$T_{eff} = T_{\max} - T_{\min} \tag{10}$$

The effective time means the duration in which the effective voltage is supplied to the machine terminals. In the actual switching instants, there is one degree of freedom that the effective time can be located anywhere within one sampling interval. To generate actual switching pattern which preserves the effective time, the zero sequence time is subjoined to the phase voltage time. In order to locate the effective time in centre of the sampling interval, the zero sequence voltage has to be symmetrically distributed at the beginning and end of one sampling period. Therefore, the actual switching times for each inverter leg can be simply obtained by the time shifting operation as below.

$$\begin{aligned} T_{ga} &= T_{as} + T_{offset} \\ T_{gb} &= T_{bs} + T_{offset} \\ T_{gc} &= T_{cs} + T_{offset} \end{aligned} \tag{11}$$

To distribute zero voltage symmetrically during one sampling period, the offset time T_{offset} is achieved using a simple sorting algorithm. the zero voltage vector time duration can be calculated as given in (12).

$$T_{zero} = T_s - T_{eff} \tag{12}$$

$$\text{And, } T_{\min} + T_{offset} \Rightarrow T_{zero}/2 \tag{13}$$

$$\text{Therefore, } T_{offset} = T_{zero}/2 - T_{\min} \tag{14}$$

In order to generate symmetrical switching pulse pattern within two sampling intervals, when the switching sequence is 'ON' sequence, the actual switching time will be replaced by the subtraction value with the sampling time as follows:

$$T_{ga,gb,gc} = T_s - T_{ga,gb,gc} \tag{15}$$

As described above, the effective time implies the applied time of a certain active vector. Therefore, with the effective vector concept, the actual switching time can be obtained directly from the stationary frame reference voltage without sector identification, effective time calculation and recombination.

To implement the novel space vector PWM, only a 3-element simple sorting algorithm is needed. Therefore, the calculation efforts of the proposed PWM method is greatly reduced as compared with the conventional space vector PWM method.

3. Topology of n-level Diode-Clamped Multilevel Inverter

An inverter which is capable of three-level or more is termed as Multilevel Inverter. The topology of n-level diode clamped multilevel inverter is as shown in Figure. 2. In this circuit, the dc-bus voltage will be split into suitable number of levels according to the number of capacitors. Although each active switching device is only required to block a voltage level of $\frac{V_{dc}}{(n-1)}$, the clamping diodes must have different voltage ratings for reverse voltage blocking. Assuming that each blocking diode voltage rating is the same as the active device voltage rating, the number of diodes required for each phase will be $(n-1)\times(n-2)$. This number represents a quadratic increase in *n*. when *n* is sufficiently high, the number of diodes required will make the system impractical to implement. If the inverter runs under PWM, the diode reverse recovery of these clamping diodes becomes the major design challenge in high-voltage high-power applications.

4. Proposed Generalized PWM Algorithm for an n-Level Inverter

For a 2-level inverter only one offset time is sufficient to evaluate the switching instants. Because, in a two-level SVPWM algorithm, in a sampling time interval, the imaginary switching time which has lowest magnitude ($T_{\min}$) crosses the triangular carrier first, and causes the first transition in the inverter switching state. While the imaginary switching time, which has the maximum magnitude ($T_{\max}$), crosses the carrier last and causes the last switching transition in the inverter switching states. Thus the switching periods of the active vectors can be determined from the $T_{\max}$ and $T_{\min}$ in a two-level inverter scheme.

But, the SVPWM algorithm for multilevel inverters, involves comparing the modulating signals with a number of symmetrical level-shifted triangular carrier waves for PWM generation. It has been shown that for an n-level inverter, n-1 level-shifted triangular carrier waves are required for comparison with the modulating waveforms. Because of the level-shifted multicarriers, the first crossing (termed the first-cross) of the modulating wave cannot always be the min-phase. Similarly, the last crossing (termed the third-cross) of the modulating wave cannot always be the max-phase. Thus, a single offset time is not sufficient to centre the middle inverter switching vectors, in a multilevel PWM scheme during a sampling period Ts.

The proposed algorithm determines the offset time for the PWM generation in the linear modulation region by using the concept of imaginary switching times. The proposed generalized PWM algorithm presents a simple way to determine the time instants at which the three reference phases cross the triangular carriers. These time instants are sorted to find the offset voltage to be added to the reference phase voltages for SVPWM generation for multilevel inverters for the entire linear modulation range, so that the middle inverter switching vectors are centered (during a sampling interval), as in the case of the conventional two-level SVPWM scheme.

For an n-level inverter, the instantaneous imaginary switching times are calculated as follows:

$$T_{as} = V_{an} \times \frac{T_s}{V_{dc}/(n-1)} \tag{16}$$

$$T_{bs} = V_{bn} \times \frac{T_s}{V_{dc}/(n-1)} \quad (17)$$

$$T_{cs} = V_{cn} \times \frac{T_s}{V_{dc}/(n-1)} \quad (18)$$

where *n* represents number of levels.

The time equivalent of a common mode voltage is termed as $T_{offset1}$ which can be defined as

$$T_{offset1} = -(T_{\max} + T_{\min})/2 \quad (19)$$

where $T_{\max}$ and $T_{\min}$ are the maximum and minimum of T_{as}, T_{bs} and T_{cs}.

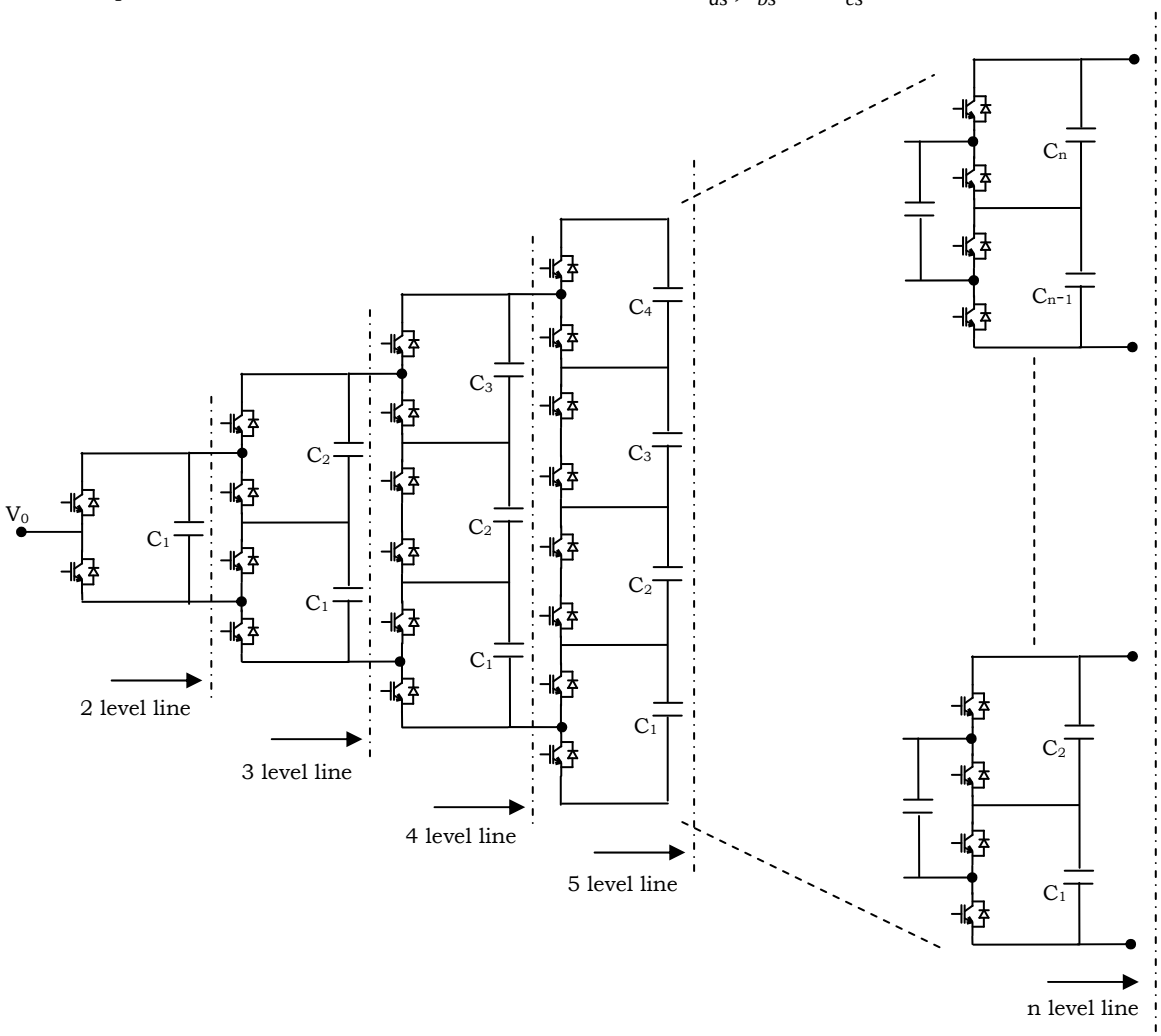

Figure. 2 Topology of n-level multilevel inverter

Then time equivalents of the modified phase voltage magnitudes can be defined as

$$T_{as}^{*} = T_{as} + T_{offset1} \quad (20)$$

$$T_{bs}^{*} = T_{bs} + T_{offset1} \quad (21)$$

$$T_{cs}^{*} = T_{cs} + T_{offset1} \quad (22)$$

The triangular carriers and the modulating waves, for an n-level PWM scheme are shown in Figure. 3a, for n is odd, and in Figure. 3b, for n is even. The (n-1) triangular carriers are compared with reference phase voltages as shown in Figures. 3a and 3b. A carrier index, I, is defined to designate the carrier regions in which the reference phase voltages lie during the sampling interval under consideration. During a sampling interval, the carrier indices, I_a, I_b and I_c (which can be from 1 to n-1), for a, b and c phases, respectively, are determined depending on the carrier region in which the respective phase voltage lies. Then the time durations, $T_{a-cross}$, $T_{b-cross}$ and $T_{c-cross}$ when n is odd, can be determined for a n-level inverter as:

$$T_{a_cross} = T_{as}^{*} + ((I_a - (n-1)/2) * T_s \quad (23)$$

$$T_{b_cross} = I_{bs}^{*} + ((I_b - (n-1)/2) * T_s \quad (24)$$

$$T_{c_cross} = T_{cs}^{*} + ((I_c - (n-1)/2) * T_s \quad (25)$$

When n is even, the time durations, $T_{a-cross}$, $T_{b-cross}$ and $T_{c-cross}$, can be determined for a n-level inverter as:

$$T_{a_cross} = (T_s/2) + T_{as}^{*} + ((I_a - (n/2)) * T_s) \quad (26)$$

$$T_{b_cross} = (T_s/2) + T_{bs}^{*} + ((I_b - (n/2)) * T_s) \quad (27)$$

$$T_{c_cross} = (T_s/2) + T_{cs}^{*} + ((I_c - (n/2)) * T_s) \quad (28)$$

in the proposed generalized PWM algorithm, the $T_{a-cross}$, $T_{b-cross}$ and $T_{c-cross}$ are used to centre the middle switching vectors as in the case of two-level inverters in each sampling time interval. The time-duration, at which the reference phases cross the

triangular carriers for the first time, second time and third time are defined as T_{first_cross} , T_{second_cross} and T_{third_cross} respectively, in a sampling time interval T_s. these can be calculated from (29).

$$\begin{aligned} T_{first_cross} &= \min\left(T_{x_cross}\right) \\ T_{second_cross} &= mid\left(T_{x_cross}\right) \\ T_{third_cross} &= \max\left(T_{x_cross}\right); \quad x = a,b,c \end{aligned} \tag{29}$$

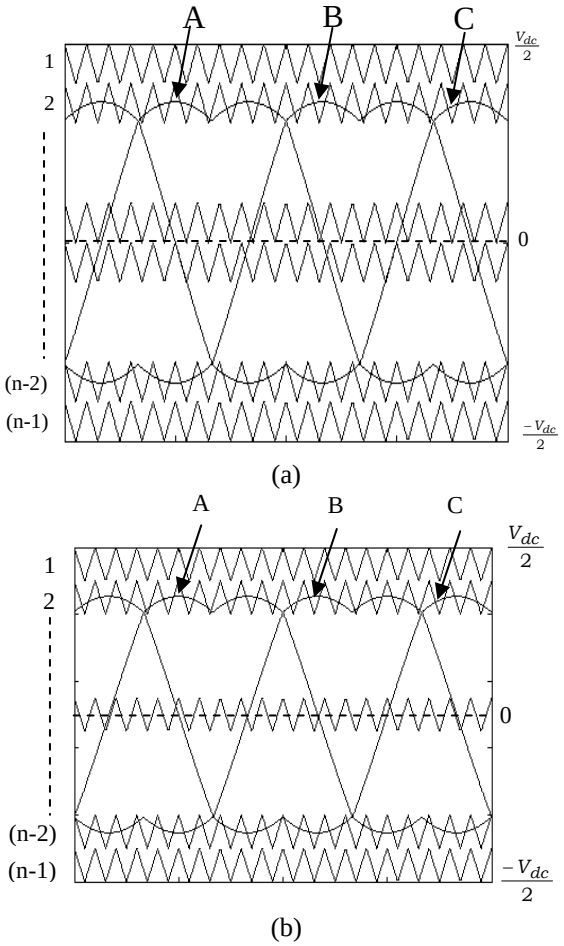

Figure. 3 Triangular carrier and reference signals (a) n-level PWM scheme where n is even (b) n-level PWM scheme where n is even

During one sampling interval Ts, the time durations T_{first_cross} , T_{second_cross} and T_{third_cross} directly decides the switching times for different inverter voltage vectors. An offset time, $T_{offset2}$ is added to T_{first_cross}, T_{second_cross} and T_{third_cross} to centre the middle vector. The offset time, $T_{offset2}$ is determined as follows:

The time duration for the middle inverter switching vectors, T_{middle}, is given as

$$T_{middle} = T_{third_cross} - T_{first_cross} \tag{30}$$

The time duration for start and end vector is

$$T_0 = T_s - T_{middle} \tag{31}$$

The time duration for start vector is given by

$$T_0 / 2 = T_{first_cross} + T_{offset2} \tag{32}$$

$$\text{Therefore, } T_{offset2} = T_0 / 2 - T_{first_cross} \tag{33}$$

By adding the time, $T_{offset2}$ to T_{first_cross} , T_{second_cross} and T_{third_cross} gives the inverter leg switching times T_{ga} , T_{gb} and T_{gc} for phases a, b and c, respectively as (34)-(36).

$$T_{ga} = T_{a_cross} + T_{offset2} \tag{34}$$

$$T_{gb} = T_{b_cross} + T_{offset2} \tag{35}$$

$$T_{gc} = T_{c_cross} + T_{offset2} \tag{36}$$

5. Results and Discussion

To validate the proposed generalized scalar PWM algorithm, several numerical simulation studies have been carried out and results are presented. The details of the induction motor, which is used for simulation studies are as follows:

A 3-phase, 4 pole, 4kW, 1200rpm induction motor with parameters of R_s = 1.57Ω, R_r = 1.21Ω, L_s = L_r = 0.17H, L_m = 0.165H and J = 0.089Kg.m^2.

The steady state simulation results for 2-, 3-, 5-, and 7-level inverter fed DTC-IM drive are shown from Figure. 4 to Figure. 19. From the simulation results it can be observed that as the number of levels increases the harmonic distortion will be decreased. Also, it can be concluded that the proposed PWM algorithm is efficient with reduced complexity. The total harmonic distortion (THD) values of line currents and voltages are given in Table-1.

TABLE I
COMPARISON OF THD IN LINE CURRENT FOR VARIOUS LEVELS

Level	% THD in line current	% THD in line voltage
2 level	*9.84*	*75.96*
3 level	*4.06*	*38.10*
5 level	*2.23*	*17.25*
7 level	*1.37*	*12.17*

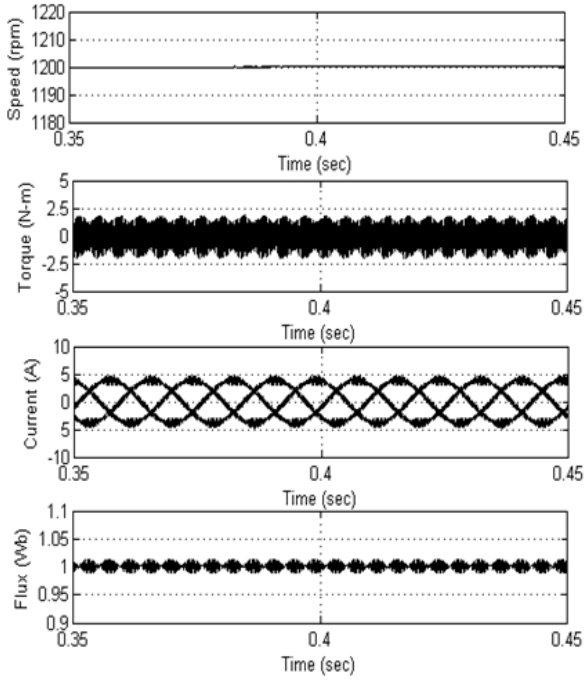

Figure. 4 Simulation results of 2-level SVPWM based DTC: steady-state plots of speed, torque, currents and flux at 1200 rpm

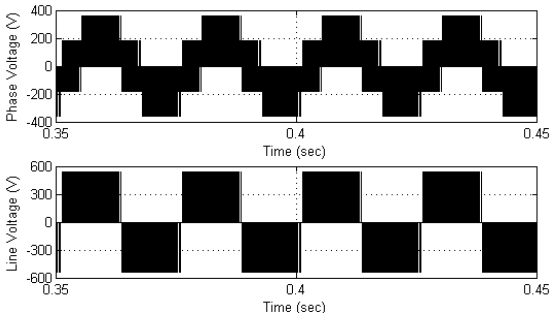

Figure. 5 Simulation results of 2-level SVPWM based DTC: steady state plots of phase and line voltages

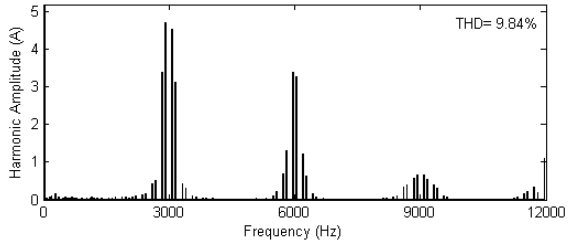

Figure. 6 Harmonic Spectrum of line current for 2-level SVPWM based DTC along with THD

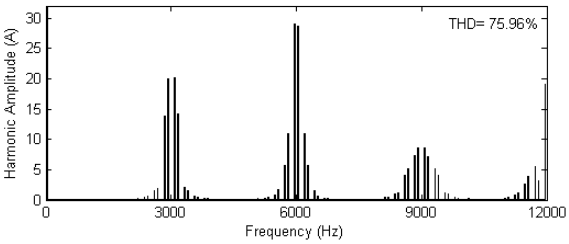

Figure. 7 Harmonic Spectrum of line voltage for 2-level SVPWM based DTC along with THD

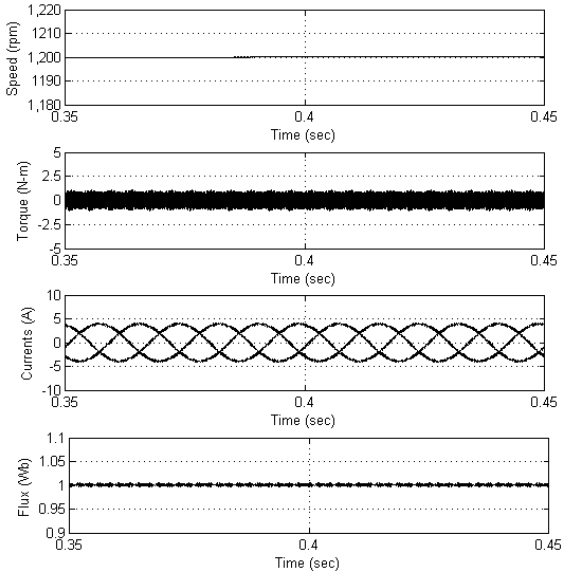

Figure.8 Simulation results of 3-level SVPWM based DTC: steady-state plots of speed, torque, currents and flux at 1200 rpm

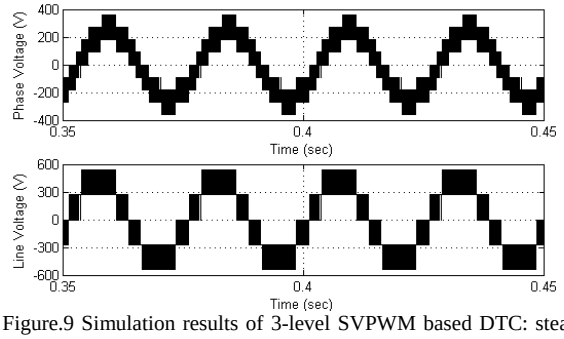

Figure.9 Simulation results of 3-level SVPWM based DTC: steady state plots of phase and line voltages

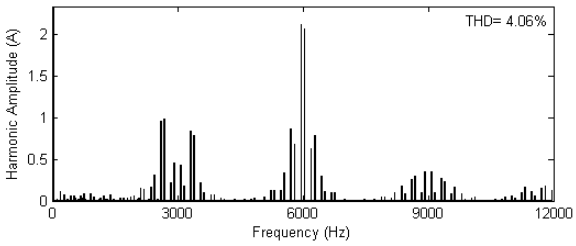

Figure. 10 Harmonic Spectrum of line current for 3-level SVPWM based DTC along with THD.

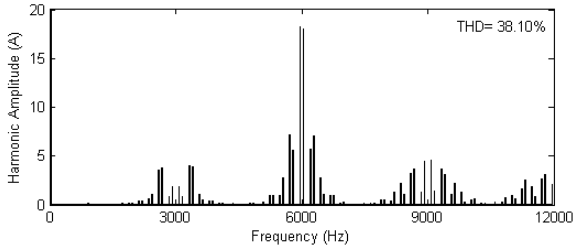

Figure. 11 Harmonic Spectrum of line voltage for 3-level SVPWM based DTC along with THD.

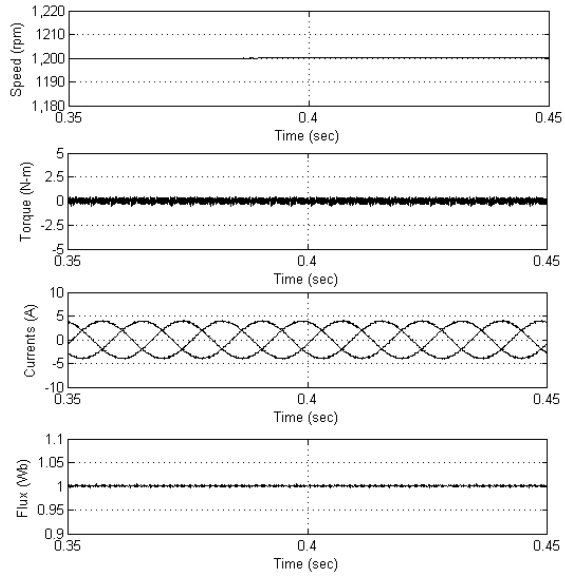

Figure. 12 Simulation results of 5-level SVPWM based DTC: steady-state plots of speed, torque, currents and flux at 1200 rpm

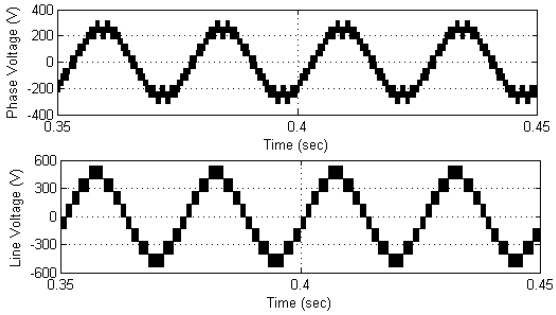

Figure. 13 Simulation results of 5-level SVPWM based DTC: steady state plots of phase and line voltages

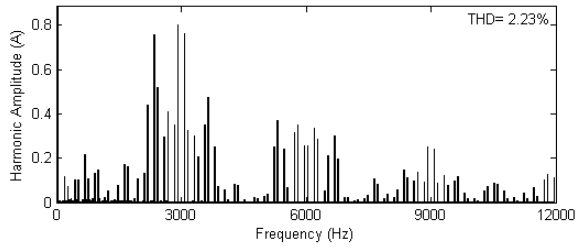

Figure. 14 Harmonic Spectrum of line current for 5-level SVPWM based DTC along with THD

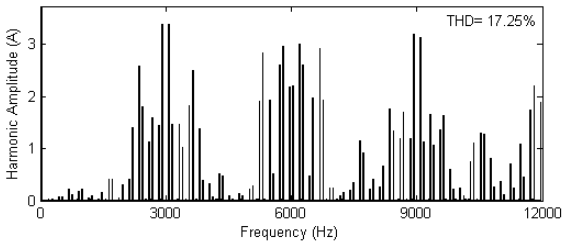

Figure. 15 Harmonic Spectrum of line voltage for 5-level SVPWM based DTC along with THD

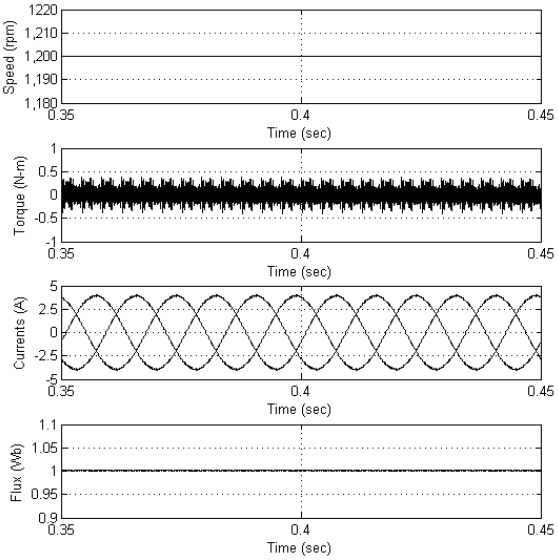

Figure. 16 Simulation results of 7-level SVPWM based DTC: steady-state plots of speed, torque, currents and flux at 1200 rpm

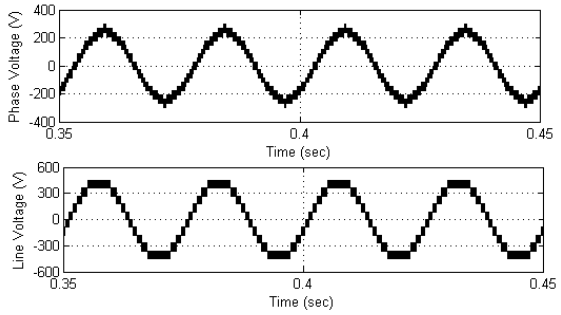

Figure. 17 Simulation results of 7-level SVPWM based DTC: steady state plots of phase and line voltages

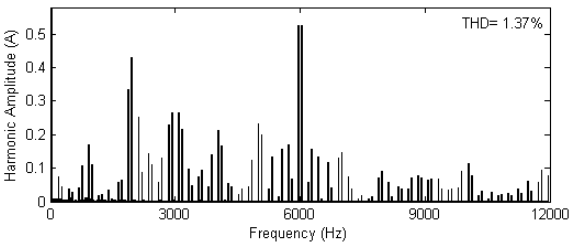

Figure. 18 Harmonic Spectrum of line current for 7-level SVPWM based DTC along with THD

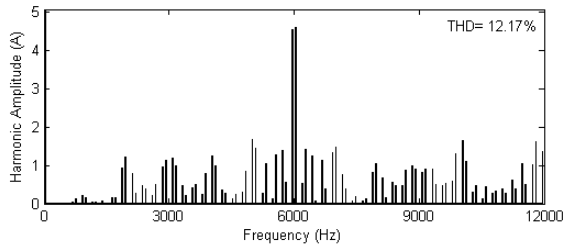

Figure. 19 Harmonic Spectrum of line voltage for 7-level SVPWM based DTC along with THD

6. Conclusion

A simple and novel generalized SVPWM algorithm is presented for an n-level inverter fed direct torque controlled induction motor drive. The proposed algorithm has been developed by using the concept of imaginary switching times, which are proportional to the sampled reference phase voltages only. Hence, the complexity involved id less when compared with the classical PWM algorithms. To validate the proposed algorithm, the simulation studies have been carried out and results are presented. From the simulation results, it can be concluded that the proposed algorithm gives good performance with reduced complexity. Moreover, as the number of levels increases, the harmonic distortion of line current and voltages also decreases.

7. References

[1] F. Blaschke "The principle of field orientation as applied to the new transvector closed loop control system for rotating-field machines," Siemens Review, 1972, pp 217-220.

[2] Isao Takahashi and Toshihiko Noguchi, "A new quick-response and high-efficiency control strategy of an induction motor," IEEE Trans. Ind. Applicat., vol. IA-22, no.5, Sep/Oct 1986, pp. 820-827.

[3] Domenico Casadei, Francesco Profumo, Giovanni Serra, and Angelo Tani, "FOC and DTC: Two Viable Schemes for Induction Motors Torque Control" IEEE Trans. Power Electron., vol. 17, no.5, Sep, 2002, pp. 779-787.

[4] Domenico Casadei, Francesco Profumo, Giovanni Serra, and Angelo Tani, "FOC and DTC: Two Viable Schemes for Induction Motors Torque Control" IEEE Trans. Power Electron., vol. 17, no.5, Sep, 2002, pp. 779-787.

[5] Joachim Holtz, "Pulsewidth modulation – A survey" IEEE Trans. Ind. Electron.., vol. 39, no. 5, Dec 1992, pp. 410-420.

[6] Heinz Willi Vander Broeck, Hnas-Christoph Skudelny and Georg Viktor Stanke, "Analysis and realization of a pulsewidth modulator based on voltage space vectors" IEEE Trans. Ind. Applicat., vol. 24, no. 1, Jan/Feb 1988, pp. 142-150.

[7] Ahmet M. Hava, Russel J. Kerkman and Thomas A. Lipo, "Simple analytical and graphical methods for carrier-based PWM-VSI drives" IEEE Trans. Power Electron., vol. 14, no. 1, Jan 1999, pp. 49-61.

[8] T. Brahmananda Reddy, J. Amarnath and D. Subbarayudu, "Direct torque control of induction motor based on Hybrid PWM method for reduced ripple: A sliding mode control approach" ACSE Journal Vol.(6) Issue(4) Dec.2006,pp.23-30.

[9] Lixin Tang and M.F. Rahman, "A new direct torque control strategy for flux and torque ripple reduction for induction motors drive by using space vector modulation" in Conf. Rec. of IEEE-PESC, 2001, pp.1440-1445.

[10] Nabae, A., Takahashi, I., and Akagi, H, "A neutral-point clamped PWM inverter', IEEE-Trans. Ind. Appl., 1981, 17, (5), pp.518-523.

[11] Jose Rodriguez, Jih-Sheng Lai, Fang Zheng Peng: 'Multilevel Inverters: A Survey of Topologies, Control, and Applications', IEEE Trans. On Ind. Elec., Vol. 49, No. 4, Aug. 2002.

[12] Abdul Rahiman Beig, G. Narayana, V.T. Ranganathan, "Modified SVPWM Algorithm for Three Level VSI With Synchronized and Symmetrical Waveforms", IEEE Trans. Ind. Elect., Vol. 54, No. 1, Feb. 2007, pp 486-494.

[13] Joohn-Sheok Kim and Seung-Ki Sul, "A novel voltage modulation technique of the space vector PWM" in Proc. IPEC, Yokohama, Japan, 1995, pp. 742-747.

[14] Dae-Woong Chung, Joohn-Sheok Kim and Seung-Ki Sul, "Unified voltage modulation technique for real-time three-phase power conversion" IEEE Trans. Ind. Applicat., vol. 34, no. 2, Mar/Apr 1998, pp. 374-380.

[15] R.S. Kanchan, M.R. Baiju, K.K. Mohapatra, P.P. Ouseph and K. Gopakumar, "Space vector PWM signal generation for multilevel inverters using only the sampled amplitudes of reference phase voltages" IEE Proc.-Electr. Power Appl., vol. 152, No. 2, pp. 297-309, March, 2005.

Biographies

Chalasani Hari Krishna was born in 1982. He graduated from Jawaharlal Nehre Technological University, Hyderabad in the year 2003. He received M.E degree from Satyabama University, Chennai in the year 2005. He presently Associate Professor in the Department of Electrical and Electronics Engineering at Mother Teresa Institute of Science and Technology, India. His research area includes DTC and Drives.

Dr. T. Brahmananda Reddy was bornin 1979. He graduated from Sri Krishna Devaraya University, Anantapur in the year 2001. He received M.E degree from Osmania University, Hyderabad, India in the year 2003 and Ph.D from J.N.T.University, Hyderabad in the year 2009. He is presently Associate Professor in the Electrical and Electronics Engineering Department, G. Pulla Reddy Engineering College, Kurnool, India. He presented more than 90 research papers in various national and international conferences and journals. His research areas include PWM techniques, DC to AC converters and control of electrical drives

Dr. J. Amarnath graduated from Osmania University in the year 1982, M.E from Andhra University in the year 1984 and Ph.D from J.N.T.University, Hyderabad in the year 2001.He is presently Professor and Head of the Electrical and Electronics Engineering Department, JNTU College of Engineering, Hyderabad and also he is the Chairman, Board of studies in Electrical and Electronics Engineering, JNTU College of Engineering, Hyderabad. He presented more than 100 research papers in various national and international conferences and journals. His research areas include Gas Insulated Substations, High Voltage Engineering, Power Systems and Electrical Drives.

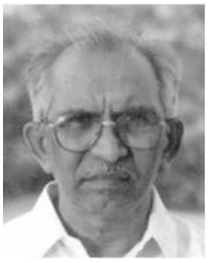

Dr. S. KAMAKSHAIAH is from JNT University, Hyderabad and worked as Professor, Head of the Department & Chairman of Electrical Sciences. He annexed Gold Medal for getting 1st rank in SV University at B.Tech level. He was also awarded Gold Medal for Ph.D. work from I.I.Sc.Bangalore for its industrial application. He was the Best Teacher award winner of the year 1997-98 which was promoted by A.P.State Government. He has got 40 Technical Publications in International level. He is also an author of three text books Introduction to Electrical Engineering, Basic Electrical Engineering and Electrical Technology with his co – author Prof. Naidu, and HVDC Transmission published by Tata McGraw Hill. He carried research work in the area of Vaccum arcs in Triggered Vaccum Gaps (TVG). At present he is working on the problems of Gas Insulated Substation (GIS) ,HVDC and Electric Drives. Presently he is working as Director, Krishna Chaitanya Institute of Technology & Science, Markapur, He visited various countries like Canada, Germany and Doha and presented papers at IEEE International Conference at ATLANTA, USA in the year June 2010.

www.icgst.com

Amélioration du temps de convergence de l'algorithme de calcul du filtre optimal par HOS en DMT

H. Bellahsene, I. F. E. Fatani
Département TCSN, Faculté SNV, Université de A/Mira Béjaia 06000, Algérie
[bellahsene_ho]@yahoo.fr,
http://www.univ-bejaia.dz

Abstract

Ce travail synthétise l'évolution de l'égalisation classique vers l'égalisation par réduction de canal. Il s'agit d'utiliser les statistique d'ordre supérieure à deux à savoir le calcul du maximum de kurtosis pour retrouver le filtre TEQ (Time-domain EQualizer) optimal. Le délai de synchronisation dans l'algorithme du MSSNR (Maximum Shortening Signal to Noise Ratio) est retrouvé par la même technique. Une comparaison entre le filtre optimal retrouvé par d'autres méthodes et celui déterminé par la méthode la notre. La fonction statistique gamma a réduire de manière conséquente le délai de convergence après son introduction dans l'algorithme.[1]

Keywords: *TEQ (Time-domaine EQalizer), High Order Statistics, kurtosis, DMT, fonction Gamma.*

1 Introduction

L'évolution de l'égalisation classique vers l'égalisation par réduction de canal à fait l'objet de nombreux travaux dans la litérature. Nous nous sommes intéressés à l'introduction des HOS dans ce damaine. Nous appliquons le calcul du maximum de kurtosis pour retrouver le filtre TEQ (Time-domain EQualizer) optimal ainsi que le délai de synchronisation dans l'algorithme du MSSNR (Maximum Shortening Signal to Noise Ratio). Nous comparons le filtre optimal retrouvé par d'autres méthodes et celui déterminé par la méthode du maximum du kurtosis. Nous arrivons par utilisation des fonctions statistiques notamment gamma, à réduire de manière conséquente le délai de convergence au prix de la stabilité de l'algorithme.
Des méthodes retrouvent le canal et calculent l'égaliseur optimal [8]. D'autres sont dites sous-optimales et/ou adaptatives [12] réalisent le même travail avec moins de performances. La plupart des approches par modèle TEQ (Time domaine Equalizer) ne sont pas adaptatives, elles nécessitent l'apprentissage ou une estimation du canal avec des calculs assez lourds à mettre en œuvre. L'algorithme amélioré est celui de MERRY (Multicarrier Equalisation by Restoration of RedundancY) [6, 11]. Nous proposons une méthode basée sur les HOS, dite par maximum du kurtosis, et nous calculons également le délai optimum ainsi que le filtre optimal lui correspondant.
Cet article est organisé de la façon suivante: Section 2 met en évidence l'algorithme d'égalisation multiporteuse par rétablissement de redondance.La fonction coût sera donnée en Section 3. Notre contribution sera mentionnée en Section 4. Des simulations et discutions des résultats fairront l'objet de la partie théorique en Section 5.Les résultats importants ainsi que les futurs travaux envisagés seront donnés en conclusion.

[1]Ce travail à été réalisé au département des TCSN, FSNV.

2 Algorithme d'égalisation multiporteuse par rétablissement de redondance

L'algorithme MERRY (Multicarrier Equalization by Restoration of RedundancY) exploite la redondance introduite dans les données à travers le préfixe cyclique, voir figure (2)[6]. C'est une approche basée sur la minimisation de l'espérance mathématique du carré de la différence cyclique qui est la différence entre des valeurs de séparées par un bloc de données.

$$\begin{aligned} y(2) &= h_0 s(2) + h_1 s(1) + h_2 s(0) + h_3 s(-1) + h_4 s(-2) \\ &= h_0 s(10) + h_1 s(9) + [h_2 s(0) + h_3 s(-1) + h_4 s(-2)] \\ y(10) &= h_0 s(10) + h_1 s(9) + [h_2 s(8) + h_3 s(7) + h_4 s(6)] \end{aligned} \quad (1)$$

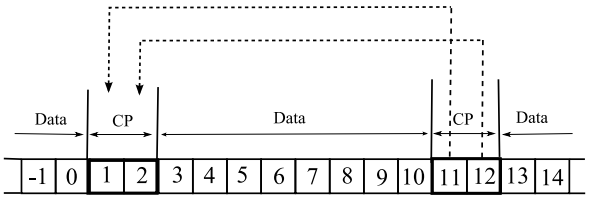

Figure 1: Rajout du CP à la trame de données

La figure 2 fait appel à l'équation 1. Ainsi, les $N + P$ données transmises deviennent périodiques. Cette périodicité est nécessaire pour maintenir l'orthogonalité des multiporteuses [10]. Les derniers symboles sont identiques aux premiers et nous pouvons écrire :

$$s(Mk+i) = s(Mk+i+N), \quad i \in \{1, \cdots, N\} \quad (2)$$

où $M = P + N$ est la durée de tous les symboles et k est l'indice de chaque symbole. La figure 2 montre un exemple où l'on prend $N = 8$, $P = 2$ et $M = 10$ correspondant à $k = 0$. Les données reçues sont obtenues à partir de selon la relation suivante :

$$r(Mk+i) = \sum_{l=0}^{L_c} c_l \cdot s(Mk+i-l) + n(Mk+i) \quad (3)$$

Les données égalisées sont obtenues à partir de suivant cette équation :

$$y(Mk+i) = \sum_{j=0}^{L_f} f_j \cdot r(Mk+i-j) \quad (4)$$

La relation donnée par (1) est détériorée à cause du canal lors de la réception des données, car les ISI qui affectent le CP sont différents de ceux qui affectent les P derniers éléments du symbole. Considérons l'exemple de la figure , Les éléments transmis 2 et 10 sont identiques. Cependant, au niveau du récepteur, l'interférence des éléments avant l'élément 2 ne sont pas toutes égales à celles qui sont avant l'élément 10. Si on considère h_2, h_3 et $h_4$nuls, alors $y(2) = y(10)$ car $s(2) = s(10)$ et $s(1) = s(9)$. Il est clair que pour avoir il faut forcer h_2, h_3 et h_4 à zéro (éléments se trouvant entre crochets dans l'équation 1), cette égalité étant prise dans le sens des moindres carrés. Nous rendons de cette façon le canal effectif de taille équivalente à celle du CP.

3 Algorithme MERRY et sa fonction coût

La fonction coût de l'algorithme MERRY est :

$$J = E\left[\left|y\left(Mk+P+\delta\right) - y\left(Mk+P++N+\delta\right)\right|^2\right] \quad (5)$$

avec $\delta \in \{0, \cdots, M-1\}$, δ étant le délais désiré (c'est le coefficient de synchronisation). Le gradient stochastique de (5) donne l'algorithme de réduction de canal adaptatif aveugle MERRY (Multicarrier Equalization by Restoration of RedundancY) [MAR 05], avec: Pour un δ donné, le symbole $k = 0, 1, 2, \cdots$,

$$\begin{aligned} \tilde{\mathrm{r}}k) &= \mathrm{r}(Mk+P+\delta) - \mathrm{r}(Mk+P+N+\delta) \\ e(k) &= \mathrm{f}^T(k)\tilde{\mathrm{r}}k) \\ \hat{\mathrm{f}}(k+1) &= \mathrm{f}^T(k) - \mu e(k)\tilde{\mathrm{r}}k) \\ \mathrm{f}(k+1) &= \frac{\hat{\mathrm{f}}(k+1)}{\left\|\hat{\mathrm{f}}(k+1)\right\|} \end{aligned} \quad (6)$$

avec $\mathrm{r}(i) = [r(i), r(i-1), \cdots, r(i-L_f]^T$, et $(\ *\ )$ est le conjugué complexe. Pour éviter la solution triviale $(\mathbf{f = 0}\ )$ nous devons prendre $\|\mathrm{f}\| = \mathbf{1}$. L'algorithme représenté par (6) donne le vecteur propre minimal de la matrice $A = E\left[\tilde{\mathrm{r}}, \tilde{\mathrm{r}}^{\mathrm{H}}\right]$. Soit C la matrice canal de convolution autrement dit h = Cf et soit C_{wall}obtenue par suppression de δ lignes des $\delta + P - 1$ de C. Si l'entrée $s(k)$ est blanche, alors $\mathrm{A} = \mathrm{C}_{wall}^T, \mathrm{C}_{wall}$. L'énergie à l'extérieur de la fenêtre du canal effectif plus le gain du bruit est donnée comme suit :

$$J_\delta = 2\sigma_s^2 \left(\sum_{j=0}^{\delta-1} |h_j|^2 + \sum_{j=\delta+P}^{L_h} |h_j|^2\right) + 2\mathrm{f}^{\mathrm{T}}\mathrm{R}_n\mathrm{f}^* \quad (7)$$

Dans le cas où la réduction du canal utilisée est autodidacte et non adaptative, alors la matrice $A = E\left[\tilde{\mathrm{r}}, \tilde{\mathrm{r}}^{\mathrm{H}}\right]$ peut être estimée à partir des données. Le vecteur propre correspondant à la valeur propre minimale peut être calculé, ce qui fournira une technique d'initialisation pour éviter les modes de convergence lents.

Réduction optimale du canal

La réduction de canal optimale utilise un algorithme basé sur le calcul des valeurs propres et des vecteurs propres pour générer les coefficients du filtre réduit optimal. La technique consiste à déterminer le filtre TEQ qui maximise le rapport de réduction du signal sur le bruit dans une fenêtre. Pour ce faire, il faut minimiser l'énergie de la réponse impulsionnelle du canal effectif, à l'extérieur de la fenêtre contenant les $(P+1\ )$ échantillons. Nous reprenons C_{win}et C_{wall} tels que définies dans [8], alors $\mathrm{h_{win}} = \mathrm{C_{win}f}$ représente le canal effectif situé dans la fenêtre de taille $(\ P+1)$. Cependant $\mathrm{h_{wall}} = \mathrm{C_{wall}f}$ donne le canal effectif en dehors de cette fenêtre. Le problème de conception du TEQ à base du MSSNR peut être décrit comme suit[8, 1, 2, 4, 9]:

$$\min_{\mathrm{f}} \left(\mathrm{f}^{\mathrm{T}}\mathrm{Af}\right) \text{ sous la contrainte } \mathrm{f}^{\mathrm{T}}\mathrm{Bf} = 1 \quad (8)$$

où A et B sont des matrices réelles [MAR 02], symétriques $L_f \times L_f$ avec :

$$\mathrm{A} = \mathrm{C}_{wall}^T, \mathrm{C}_{wall}, \ \mathrm{B} = \mathrm{C}_{win}^T, \mathrm{C}_{win} \quad (9)$$

Elles représentent, respectivement, les énergies correspondant à C_{wall}et C_{win} où :

$$h_{wall}^T h_{wall} = f^T C_{wall}^T Cf = f^T Af \quad (10)$$

$$h_{win}^T h_{win} = f^T C_{win}^T C_{win} f = f^T Bf \quad (11)$$

La résolution de l'équation (8) mène au TEQ qui donne la solution du problème de vecteurs propres généralisé [10], nous avons par conséquent :

$$Bf = \lambda Af \quad (12)$$

où λ est la valeur propre généralisée correspondant au vecteur propre généralisé f, qui est la solution de l'équation (12).

$$C = \left(\sqrt{B^T}\right)^{-1} A \left(\sqrt{B}\right)^{-1} \quad (13)$$

L'inverse de la matrice A est retrouvé par factorisation de Cholesky. Les TEQ sont alors donnés par :

$$f = \left(\sqrt{B^T}\right)^{-1} q \quad (14)$$

où q est le vecteur propre correspondant à la valeur propre λ. Il est montré aussi [8] que l'algorithme converge globalement si $q = q_{min}$ est le vecteur propre minimal correspondant à la valeur propre minimale λ_{min} . C'est ainsi que le filtre TEQ optimal f_{opt}est retrouvé [3]. L'expression du SNR réduit optimal (Shortening SNR ou SSNR) est donnée par :

$$SSNR_{opt} = 10 \log \left(\frac{f_{opt}^T B f_{opt}}{f_{opt}^T A f_{opt}} \right) = 10 \log \left(\frac{1}{\lambda_{min}} \right)$$

$$SSNR_{opt} = -10 \log (\lambda_{min}) \quad (15)$$

En somme, l'algorithme optimal utilise la matrice C, dont les éléments sont calculés à partir de H_{wall} et H_{win}. Le SSNR optimal est retrouvé par calcul direct des valeurs propres minimales de la matrice C. Les coefficients du TEQ optimal sont finalement calculés par transformation linéaire du vecteur propre unitaire associé à la valeur propre minimale.

4 Modification de l'algorithme

4.1 Le filtre optimal

Cette procédure débute à partir de tous les filtres réduits f_n ayant été trouvés à partir de l'équation (14), utilisant l'algorithme du MSSNR [8]. Nous proposons de choisir le filtre SCE (Shortened Channel Equalizer) optimal, non pas en comparant les énergies de tous les filtres trouvés tels que abordés par Martin et al. dans [7], mais plutôt en calculant le kurtosis de chaque filtre. Nous avons ainsi :

$$y_n = h * f_n \quad (16)$$

$$g_n = \kappa_4(y_n) \quad (17)$$

Réduire le canal revient à trouver un filtre tel que sa séquence de sortie ait la même variance et le même kurtosis maximum en valeur absolue qu'à l'entrée du filtre. Le filtre optimal sera celui qui maximisera la quantité donnée par l'équation (19). Le délai de synchronisation sera la valeur de l'indice qui correspondra à ce filtre, tel que:

$$k = \underset{n}{arg} \{max(g_n)\} \quad (18)$$

4.2 Calcul du pas de convergence par kurtosis

Le kurtosis normalisé d'une variable aléatoire s ayant comme valeur moyenne $\bar{s}$ est défini par le rapport du moment d'ordre quatre η_4 au carré du moment d'ordre deux η_2^2 tous deux centrés. Les HOS (Higher Order Statistics) définissent le kurtosis comme suit [LAC 97]:

$$\kappa_4(s) = \frac{\eta_4}{\eta_2^2} \quad (19)$$

où, si est E l'opérateur espérance mathématique:

$$\eta_2 = E\left\{(s - \bar{s})^2\right\} \quad (20)$$

$$\eta_4 = E\left\{(s - \bar{s})^4\right\} \quad (21)$$

L'excès (kurtosis standard) est défini par l'équation (19) moins trois. Il s'annule lorsqu'il s'agit d'une distribution normale [3, 5]. D'ou tout l'intérêt à introduire ce coefficient. En effet, sachant que le bruit additif est dans la plupart des cas de type Gaussien, il est bien connu que les statistiques d'ordre supérieur ne sont pas affectées par le bruit. Nous proposons dans ce papier une méthode itérative pour le calcul de μ. En effet, le pas de convergence divisé par le kurtosis normalisé donné par l'équation (19) de la séquence reçue à l'entrée de l'égaliseur permet de tenir compte à chaque itération de la séquence à l'entrée de l'égaliseur r(i). Ainsi, le pas de convergence du nouvel algorithme est calculé à partir d'un μ_0 divisé à chaque itération par le kurtosis de sorte à avoir:

$$\mu_{i+1} = \frac{\mu_0}{\kappa_4 (r(i))} \quad (22)$$

Par ce procédé, la mise à jour du pas de convergence dépend des données reçues (c'est à dire des conditions de transmission du canal). Deplus, nous utilisons la fonction de densité de probabilité Gamma connue dans la littérature pour la détermination du pas de convergence. Les résultats obtenus vont maintenant être discutés dans la partie consacrée aux simulations.

5 Simulations

Les données que nous utilisons lors de la simulation sont les huit CSA loop (Carrier Serving Area) [7], utilisées dans le standard ADSL. Nous utilisons le CSA1

lors de nos simulations. Le CP est de taille, la taille de l'égaliseur est égale à 16 [9]. La figure 2 représente les réponses impulsionnelles du canal réelle et celle réduite par MSSNR à partir de l'algorithme MERRY optimal. La figure3 représente les réponses impulsion-

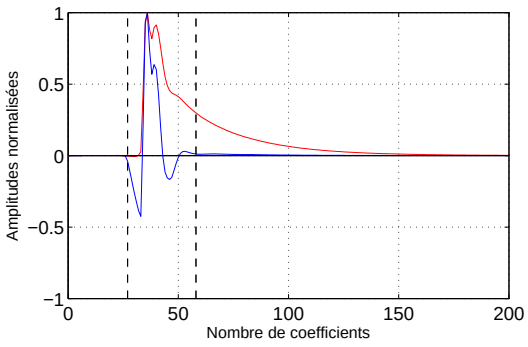

Figure 2: Canal réel et canal réduit par MSSNR

nelles du canal réelle et celle réduite par la méthode du maximum du kurtosis. Afin de pouvoir comparer les résultats donnés par les deux méthodes, nous nous proposons de dérouler l'algorithme de MERRY et celui que nous proposons. Le pas de convergence étant

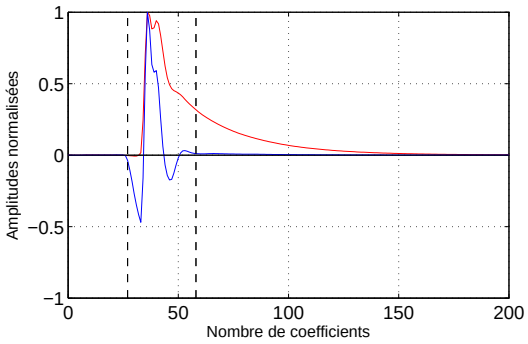

Figure 3: Canal réel et canal réduit par maximum du kurtosis et la fonction gamma

déterminé par notre technique d'itération dépendant de la séquence de données ou de façon classique. Dans tous les cas nous choisissons un SNR égal à 40dB.

Les figures (2 et 3) donnent les réponses impulsionnelles réelle et réduite dans les deux cas (à savoir la méthode du MSSNR et celle du kurtosis conjuguée à la fonction Gamma. Les deux figures sont très semblables mis à pars quelques légères différences. La figure 4 donne la fonction coût de MERRY ainsi que le débit. Nous remarquons que la convergence est effective à partir de la 500ème itération avec un débit fluctuant entre 3 et 4Mb/s. La figure 5 représente la fonction coût et le débit faisant appel aux statistiques d'ordre supérieur HOS et la fonction Gamma. Nous remarquons que la convergence est effective à partir de la 180ème itération avec un débit fluctuant entre 3 et 4Mb/s.

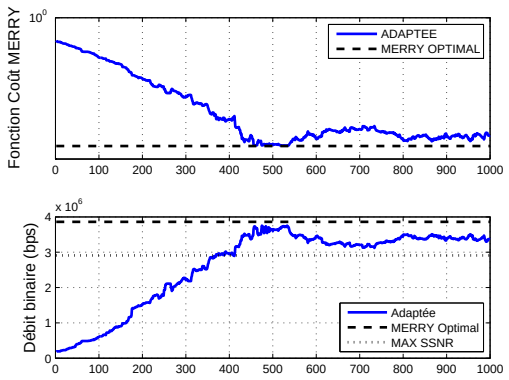

Figure 4: Courbe de convergence par MERRY optimal

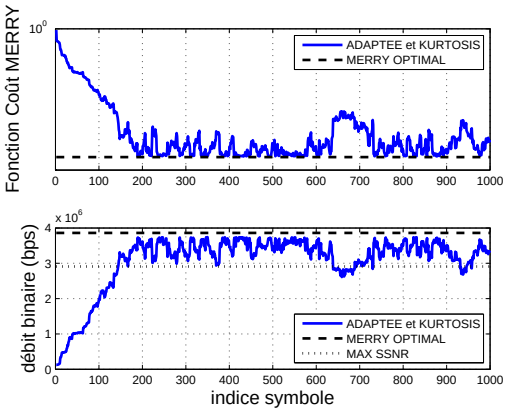

Figure 5: Courbe de convergence par kurtosis et la fonction Gamma

Il est à remarquer que les délais optimaux sont différents de ceux retrouvés dans la littérature [6].

6 Conclusion

Nous avons amélioré les approches adaptatives de réduction de canal aveugle. En effet, une nouvelle méthode de calcul du filtre optimal par maximisation du kurtosis à été proposée. Le délai de synchronisation a pu être calculé. Les résultats trouvés ont été comparés avec ceux donnés dans la littérature. A travers les HOS (High Order Statistics) conjugué à la fonction Gamma le temps de convergence de l'algorithme a été nettement réduit. Il est à signaler que la stabilité de la fonction coût et du débit est meilleure avec la méthode de MERRY. La stabilité des résultats fera l'objet de travaux futurs. Tous nos travaux de simulation ont été réalisés sous Matlab.

Remerciements

Nous remercions le Pr J. M. Rouvaen du laboratoire IEMN de l'université de valenciennes en France pour

son aide. Nous remercions aussi, l'université de Texas AT, Austin aux USA pour avoir mis à notre disposition les données standards CSA.

References

[1] N. Al-Dhahir. FIR Channel Shortening Equalizers for MIMO ISI Channels. *IEEE Trans. on comm*, 49(2):213–218, 2001.

[2] G. Arslan, B. Lu, L. D. Clark, and B. L. Evans. Iterative Refinement Methods for Time Domain Equalizer Design. *EURASIP Processing*, 2006(1):83–95, 2005.

[3] I. Chahed, H. Bellahsene, J. M. Rouvaen, and M. Djeddi. Selection of the order of ARMA model using Kurtosis minimisation. Application to blind deconvolution of seismic data. *AMSE proceding*, 47(2):77–89, 2004.

[4] D. D. Falconer, S. L. Ariyavisitaul, A. Benyamin-Seeyar, and B. Eidson. Frequency domain equalization for single-carrier broadband wireless systems. *IEEE Comm. Mag.*, 40(4):58–66, 2002.

[5] J.L. Lacoume, P.O. Amblard, and P. Comon. *Statistiques d'Ordre Supérieur pour le Traitement du Signal*. Masson, 1997.

[6] R. K. Martin, J. Balakrishnan, W. A. Sethares, and C. R. Johnson. A Blind Adaptive TEQ for Multicarrier Systems. *IEEE Signal Processing Letters*, 9(11):341–343, 2002.

[7] R. K. Martin and C. R. Johnson. Adaptive Equalization: Transitioning from single-carrier to multicarrier systems. *in Proc. IEEE Signal mag.*, 22(6):108–122, 2005.

[8] P. J. W. Melsa, R. C. Younce, and C.E. Rohrs. Impulse Response Shortening for discrete Multitone Transcievers. *IEEE Trans. on comm.*, 44(12):1662–1672, 1996.

[9] H. Minn, N. Al-Dhahir, and Y. Li. Optimal Training Signals for MIMO OFDM Channel Estimation in the Presence of Frequency Offset and Phase Noise. *IEEE Trans. on comm.*, 54(10):1754–1759, 2006.

[10] T. Pollet, M. Peeters, M. Moonen, and L. Vandendorpe. Equalization for DMT-Based Broadband Modems. *IEEE comm. mag.*, 38(5):106–113, 2000.

[11] A.H. Sayed. *Fundamentals of adaptive filtering*. John Wiley, 2003.

[12] B. Widrow, J. M. McCool, M. G. Larimore, and C. R. Johnson. Stationary and Nonstationary Learning Characteristics of the LMS adaptive filter. *Proc. IEEE*, 64(8):1151–1161, 1976.

Biographies

Dr.Bellahsene Hocine a reçu son diplôme d'ingénieur en communication en 1993 et le diplôme de Magistère 1999 à l'université de Tizi-ouzou (Algérie). Il prépara sont diplôme de doctorat au laboratoire IEMN laboratory (Valenciennes, France) de janvier 2005 à juillet 2007. Il reçu son doctorat en juin 2009. Il est actuellement maître de conférence à l'université de Béjaia (Algérie). Son domaine d'intérêt porte sur l'égalisation aveugle dans les systèmes de coommunications, les statistiques d'ordre supérieur et les techniques MIMO pour les communications numériques. mail: bellahsene_ho@yahoo.fr.

Fatani Imade Fahd Eddine est actuellement en post doc à l'univeristé de Valenciennes en France. Il à obtenu son diplôme de docteur en télécommunication à la même université en septembre 2010. Actuellement il travail à l'école nationale des sciences appliquées de khouribga au Maroc. Son domaine d'intérêt porte sur les techniques de codage conjoint source canal, les techniques MIMO pour les transmissions et les transmission vidéo H 264 dans le contexte MIMO. Mail: fatani.imade@gmail.com